UC Berkeley

UC Berkeley Electronic Theses and Dissertations

Title

Supernova Ia Spectra and Spectrophotometric Time Series: Recognizing Twins and the Consequences for Cosmological Distance Measurements

Permalink

https://escholarship.org/uc/item/8wd353zx

Author

Fakhouri, Hannah

Publication Date

2013

Peer reviewed|Thesis/dissertation

eScholarship.org Powered by the California Digital Library
University of California

Supernova Ia Spectra and Spectrophotometric Time Series: Recognizing Twins and the Consequences for Cosmological Distance Measurements

by

Hannah Kathleen Fakhouri

A dissertation submitted in partial satisfaction of the

requirements for the degree of

Doctor of Philosophy

in

Physics

in the

Graduate Division

of the

University of California, Berkeley

Committee in charge:

Professor Saul Perlmutter, Chair

Professor Steve Boggs

Professor Chung-Pei Ma

Fall 2013

Supernova Ia Spectra and Spectrophotometric Time Series: Recognizing Twins and the Consequences for Cosmological Distance Measurements

Copyright 2013

by

Hannah Kathleen Fakhouri

Abstract

Supernova Ia Spectra and Spectrophotometric Time Series: Recognizing Twins and the Consequences for Cosmological Distance Measurements

by

Hannah Kathleen Fakhouri

Doctor of Philosophy in Physics

University of California, Berkeley

Professor Saul Perlmutter, Chair

In Part I we introduce the method and results of the Twin Supernova analysis. This novel approach to Type Ia supernova standardization is currently only possible with spectrophotometric timeseries observations from the Nearby Supernova Factory. As Chapters 1 through 4 will explore, we select an ideal subset of supernovae, find pairs whose features match well in flux at all wavelengths and times, and test their dispersion in brightness. The analysis is completed in a blinded fashion, ensuring that we are not tuning our results. What we find is that twin supernovae do indeed have a small brightness dispersion.

Part II shows two additional analyses related to the standardization of Type Ia supernovae. In Chapter 5 we present a check on the results of Bailey et al. [2009]. Literature supernovae with spectra near maximum light were tested to see how well their magnitudes could be standardized using the flux ratio method of Bailey et al. [2009]. Chapter 6 shows a study with data from the Nearby Supernova Factory. Using only the spectrophotometric observations near maximum light, we calculate monochromatic Hubble Diagram residuals for each supernova. Those residuals are then corrected using a flux ratio, similar to Bailey et al. [2009], to test the standardization possibilities using only near-maximum observations.

For my dad: what can a daughter say to a father who has filled her life with love, encouragement, and passion for learning. Thank you for all you instilled in me from my youth. It is with deep gratitude that I dedicate this work to you.

Contents

Acknowledgments

This journey has been long and there are many to whom I am grateful for their love and support.

Thank you Mom and Dad for always encouraging me to pursue my passion and for teaching me the life skills necessary for a successful launch into adulthood. Thank you to my siblings: Abby, Ruth, and Nate, for teaching me how to play well with others. Thank you to Sister Maria Mater Dei, my deeply loved soul sister, for her continual support, though far away.

To all my undergraduate professors and mentors (especially Dave Besson), thank you for teaching me, believing in me, and encouraging me. To my cohort: all those problem sets would have been much less fun without you; I am thankful for all the fond memories I have of battling through quantum homeworks together.

Many thanks to my group, David, Josh, Kyle, Nao, Jakob, Alex, Rollin, and Greg, for the many helpful suggestions (and even the unhelpful ones); I am blessed to have worked on a project that so many people found so interesting. A special thanks to Rollin Thomas, without whom the Gaussian Process work would not have been possible.

Many thanks to my advisor Saul: I admire your passion and count myself fortunate to have been your student. Without you this analysis would not have come to be. I will carry forward with me many fond memories of your passion for discovery.

To my community, thank you! Through all these years, your prayers and support have endlessly improved my quality of life. A special shout out to my bible study ladies, especially Karen Grutter, with whom I have shared my successes and struggles in our weekly meetings, and Melissa Filbin who has brought much joy and laughter and deep friendship to my life.

To my dear husband Onsi, thanks are not enough. Your excitement about my research has meant more than I know how to say. That you have never doubted my abilities is something I take for granted. Your confidence in me has made this thesis possible. To our son, Joseph! You are my delight. Thank you for your smiles and hugs and joy. And to our baby girl on the way, I can't wait to meet you and some day tell you all about supernovae.

And thank you Jesus; to spend time studying your creation has been a gift.

Part I

Twin Supernovae with the Nearby Supernova Factory

Chapter 1

Introduction

Due to their uniformity in absolute brightness, Type Ia Supernovae have been used as standard candles, allowing cosmological distance measurements. In the late 90s, studies of high-redshift Type Ia Supernovae lead to the discovery of the accelerated expansion of the universe, a remarkable and paradigm-shifting discovery (Riess et al. [1998],Perlmutter et al. [1999]).

A Type Ia Supernova is the result of the death of a Carbon-Oxygen white dwarf. The explosion is triggered by mass accretion from a companion star, though the type of companion star is still under study, namely a main sequence companion or a white dwarf companion. In either scenario, the white dwarf accretes matter from its companion until the pressure is great enough to ignite carbon burning, which unbinds the star. The burning proceeds through intermediate mass elements, such as silicon, all the way to iron peak elements. This carbon ignition happens around the Chandrasekar mass, the maximum mass that can be supported by electron degeneracy pressure. Close to uniform mass means similar amounts of energy being released in the burning process and similar amounts of photons produced, resulting in what we call standard candles.

In truth, Type Ia Supernovae are standardizable, not standard, candles: there exists about 40% variation in the uncorrected brightness of these objects [Kim et al., 1997]. The physical source of this variation is not fully understood, but corrections have been devised since the early days of the field to make these brightnesses more standard. The two canonically used are stretch and color. Stretch accounts for the brighter-broader correlation: Type Ia SNe with broader light curves (in the time domain) tend to have a brighter absolute magnitude. The color correction is designed to account both for extrinsic reddening due to dust and intrinsic color differences arising from differences in the physics of the supernova explosion. With these corrections, the variation in brightness drops to 15%, allowing precision cosmology measurements.

Since the discovery of the accelerated expansion, many large Type Ia Supernova programs have been completed, resulting in sufficiently large data sets that statistical errors have become subdominant to systematic errors [Sullivan et al., 2011]. The dominant systematic error is currently calibration [Conley et al., 2011], though soon that too will fall subdomiant to intrinsic supernova explosion differences.

Standardization techniques have been and continue to be tried to decrease the brightness dispersion. Various spectral metrics have been tried, mostly using spectra near maximum light. The Bailey Ratio [Bailey et al., 2009] was able to achieve 0.128 mag dispersion using only a spectral correction. Recent explorations into using IR bands show a standardization as good as 0.085 mag level for nearby SNe Ia [Barone-Nugent et al., 2012]. The application of this method to higher redshifts is challenging for a variety of reasons. One is the intrinsically low flux in the IR. Additionally, the IR is overwhelmed by atmospheric lines, making observations from the ground very difficult. Observations from space are hindered by the lack of detectors for supernovae beyond about redshift 0.03, making a high-redshift study untenable. All these studies attempt to circumvent the problem of dust, namely that some of the observed color arises from dust and some is intrinsic color from the specifics of the explosion, and disentangling the two is a major challenge in standardizing Type Ia supernovae.

Using new more detailed measurements of Type Ia supernova timeseries, we are able to go even further in exploring standardization techniques, using spectra across all phases. A

timeseries of spectrophotometric observations offers a look at the physics of the explosion through the expanding photosphere. Each phase observation is a snapshot of the elements visible at that stage of the expansion. If two timeseries were to match in flux at all wavelengths and times, they would represent the same physical explosion process. We call two such timeseries Twin Supernovae.

A distinct advantage of this twin supernova methodology is the ability to separately account for color arising from dust extinction. Dust extinction being constant in time, we are able to fit a color law for the relative amount of dust extinction in the two timeseries. Two objects that are true twins would have the same intrinsic color and the same spectral features at all times; any color difference between them is then from dust extinction. An advantage of this color correction is that we are able to put reddened supernovae to use in this analysis.

For pairs of supernovae that are twins, we expect a very low brightness difference, as they represent the same explosion physics. If this is indeed the case, we could do cosmology with true standard candles, with no stretch or intrinsic color corrections necessary.

The data set we use from the Nearby Supernova Factory (SNfactory) [Aldering et al., 2006] is the first of its kind. As an untargeted search in the Hubble flow, it not only mimics the subtypes of type Ia supernovae that are found in high redshift searches, but also is at high enough redshift to be in the regime where peculiar velocity errors are subdomiant. To do a twin supernova analysis, frequent observations are necessary to ensure that the analysis captures relevant spectral feature changes. With data from SNfactory, we have spectrophotometric observations every 2 to 3 days. Chapter 2 describes the data set, the current state of production, and cleaned subset we have prepared for the twins analysis. Note that we finalize the sample selection criteria before examining the brightness scatter, which gives us the freedom to finalize our data quality and subset cuts without concern that we are tuning the result.

Additionally Section 2.2 introduces the techniques we developed to directly compare the supernovae observations to each other. Although we have very good cadence with the SNfactory data, rarely do we have observations at identical phases. Correctly comparing both the spectral feature shapes and the overall flux level is essential to the robustness of the analysis.

The twins analysis is performed in a blinded fashion. The supernova sample is split into a training half and a validation half. The analysis is developed and finalized on the training half of the data in Chapter 3 before including the validation half and checking the result on the unblinded full sample in Chapter 4.

Pairs are identified and ranked in Sections 3.1 and 3.2 and in Section 3.3 we answer the question: are better-ranked pairs more tightly dispersed in brightness? Additionally we present a cosmologically useful way to calculate the weighted RMS for our ranked sets of pairs. In Section 3.4 we introduce a weighting scheme that optimally takes into account data at different phases. Monte Carlo randomization tests are performed in Section 3.5 and outlier rejection is explored in Section 3.6. The chapter ends with Section 3.7, a variety of checks that were explored in advance of examining the full sample results.

Section 4.1 shows the checks that were performed on the full sample before unblinding the WRMS result that is shown and discussed in Section 4.2.

Chapter 2

The Nearby Supernova Factory Data Set

2.1 Nearby Supernova Factory

The data used in this study were obtained by the Nearby Supernova Factory between 2006 and 2009 using the SuperNova Integral Field Spectrograph [SNIFS, Lantz et al., 2004]. SNIFS consists of a high-throughput wide-band pure-lenslet integral field spectrograph [IFS, "à la TIGER;" Bacon et al., 1995, 2000, 2001], a multi-filter photometric channel to image the field in the vicinity of the IFS for atmospheric transmission monitoring simultaneous with spectroscopy, and an acquisition/guiding channel. The IFS possesses a fully-filled $6.''4 \times 6.''4$ spectroscopic field of view subdivided into a grid of 15×15 spatial elements, a dual-channel spectrograph covering 3200–5200 Å and 5100–10000 Å simultaneously, and an internal calibration unit (continuum and arc lamps). SNIFS is mounted on the south bent Cassegrain port of the University of Hawaii 2.2 m telescope on Mauna Kea, and is operated remotely. Spectra of all targets were reduced using the SNfactory's dedicated data reduction pipeline, similar to that presented in § 4 of Bacon et al. [2001]. A brief discussion of the software pipeline is presented in Aldering et al. [2006] and is updated in Scalzo et al. [2010].

For this analysis we use an early release of the data. There are individual spectra with clear flaws in the data reduction that are obvious to the eye and for which there is not yet a complete series of automatic rejections in place. Moreover, even if the reduction is okay to first order, there could be second order effects that do hurt the analysis; Section 2.3 details how these issues were handled to obtain the high quality subset we require for this analysis.

2.2 Interpolation of Supernova Timeseries

For the twins analysis, we need to be able to compare data between candidate twin supernovae at the same phases. Although the spectrophotometric timeseries in the SNfactory sample are sampled every few days, rarely are the observations at the same phase relative to maximum light. We use a method called Gaussian Processes (GPs) to interpolate a SN time series to desired phases. To take advantage of all the data we have, we interpolate in both directions. In comparing SN_A to SN_B we first interpolate SN_A to the phases of SN_B and then vise versa. We give the pair a ranking (discussed in Section 3.2) by combining the results of both interpolation directions.

The basic idea of a Gaussian Process is that it allows non-parametric reconstruction of a function from data. It requires the selection of a mean function, which is an initial guess of the average supernova flux at all phases and wavelengths. (The end result is not highly dependent on the choice of the mean function, so long as a reasonable function is used.) The workhorse of the Gaussian Process is the kernel, which specifies the correlation lengths in wavelength and time. The parameters of the kernel, called hyper-parameters, are optimized separately for each SN timeseries and with them we can interpolate the SN flux to the phases of interest.

Appendix A provides a detailed introduction to Gaussian Processes and a detailed discussion of their application to the SNfactory sample.

2.3 Supernova Sample Selection

2.3.1 Coverage Cuts

For each of the 132 SNe in our initial sample we do the following to determine its utility for this analysis. We begin with a set of coverage cuts and then do a series of quality cuts. We require coverage for the SN begin before +2 days after maximum light to ensure we are sampling some of the region of highest spectral diversity. We only consider coverage out to +25 days, as supernova spectra become increasingly similar at later times [Branch et al., 2008] and because of computational efficiency (i.e decomposing a 3000x3000 matrix with spectra out to day +25 is preferable to a 6000x6000 matrix with spectra out to day +45, when most of supernova spectral diversity is captured in the first two weeks or so past maximum light.)

The calibration for the red and blue arms of the spectrograph are performed separately, and as such there are times when only one or the other successfully completed in this early version of the reduction. We choose to leave these observations out. In principle we could include these spectra, as the GP is capable of predicting the missing channel, but for simplicity in the analysis we choose to use only spectra with both channels.

Occasionally a supernova has more than one observation on a given night. In these cases, we use only one of the observations (preferentially the latest one unless there is a quality reason to prefer an earlier one). This is done because if there were to be any sort of calibration issues between multiple spectra on a given night, the GP would pick this up as a relevant time length scale, but this time length scale would be much too small at other phases and would not be capturing the desired variation. In future analyses of this kind, one might look for alternative ways to constrain the correlation lengths of the kernel in the time direction so as to take advantage of this additional data.

Additionally there must be no gap greater than 10 days in coverage. This is enforced to ensure the GP model is well-constrained by supernova data and not relying too heavily on the mean function.

In total, the supernova must have at least five spectra before +25 days, again to ensure that the GP model is well-constrained by supernova data. By limiting the sample size with these cuts based on coverage, we are at worst losing some potential good pairs for the sake of sample purity. As we have such a large sample to begin with, we prefer sample purity for this initial analysis. Further analyses may wish to be more lenient in sample cuts.

For the initial sample of 132 supernovae, there are 1364 spectra before +25 days in this reduction version. Of these, 71 ($\sim 5\%$) have only one channel and are ignored. The coverage cuts discussed above remove 35 supernovae from the sample: 16 are rejected due to starting after +2 days, 17 are rejected for a coverage gap larger than 10 days, and an additional two are rejected for having fewer than five spectra. This leaves 97 supernovae that will be examined for quality.

2.3.2 Quality Cuts

The first quality cut we do is an initial visual scan of the spectra to identify and remove spectra with obvious calibration issues or low signal to noise spectra if there is another

observation of the same supernova on the same night that has higher signal to noise. In total 37 spectra are removed in this fashion and they are shown in Figures 2.1 to 2.3. By and large this was a very clear-cut process. The goal was to remove spectra that were obviously bad or obviously lower signal to noise than another observation on the same night. Two supernovae are lost after this visual scan, one because it no longer has a spectrum before +2 days and another because it no longer has five spectra before +25 days.

The next quality cut that is done is to do a visual scan at the level of the data cube, the 3-D data cube with x,y spatial and λ spectral indices. We examine cubes that are collapsed along the wavelength direction for the blue and red chanels to look for evidence of bad host subtraction (presence of residual host light in the collapsed cube), blue step (a step in the background flux level on the blue cubes resulting from calibration effects), or other questionable behaviors characteristic of this early reduction version. If a cube looks suspect, the spectrum resulting from that cube is dropped from the analysis. A scan of all cubes corresponding to spectra out to +25 days for each supernova results in 69 spectra being removed. 12 supernovae are additionally lost from the sample, as they no longer satisfy the coverage cuts. Although we have no direct evidence that spectra from these cubes would be problematic in the final analysis, our method is to throw out in advance anything that would be suspect upon inspection further down the line so that we are not in a position to compromise the blinded nature of the analysis.

The final quality check is done by examining the GP predictions for visual quality. We require that the wavelength-averaged GP predictions (i.e. bolometric figures) be smooth as a function of phase, as in the left panel in Figure 2.4. The right panel of the figure shows an example of cases in which although the data look fine individually, the GP prediction is not well behaved: the predicted bolometric flux does not follow the smooth bolometric curve expected for SNe Ia. As we will use the GP prediction to interpolate spectrophotometric data, we need to be able to trust the flux level as well as the individual feature shapes. Thus again we reject such SNe from our sample to ensure purity.

In order to test if an individual spectrum might be strongly affecting the GP, we do a "leave one out test": for each supernova, we remove each spectrum in turn and redo the GP model and predictions. This is the best direct test of the GP's ability to interpolate, as we are able to compare the GP prediction to the actual data that we left out. Figures 2.5-2.7 show three examples of this test: the data are in black and in color is the GP prediction at that phase when the corresponding data are left out. The first, Figure 2.5, shows a supernova with fairly high signal to noise; this object performs well on the leave one out test, indicating that no individual spectra are problematic. Next, Figure 2.6 illustrates the same, but for a supernova with moderate signal to noise. Aside from the difference in signal to noise, these two examples are typical of the 74 supernovae that passed this check.

The final example, Figure 2.7, shows a problematic supernova, randomly chosen and typical of the issues for the nine that were thrown out. The Gaussian Process is unable to accurately predict the overall flux level of the spectra that are left out. In this case, this is due to overall flux disparity between two spectra: the earliest one at +2 days (not shown in the figure) and the next at +4.8 days (first spectrum in figure). Not wanting to be dependent on templates, we cannot assess which of these spectra is correct (if, indeed, either is). We thus choose to reject this SN from the sample, again to maximize purity of the final subsample.

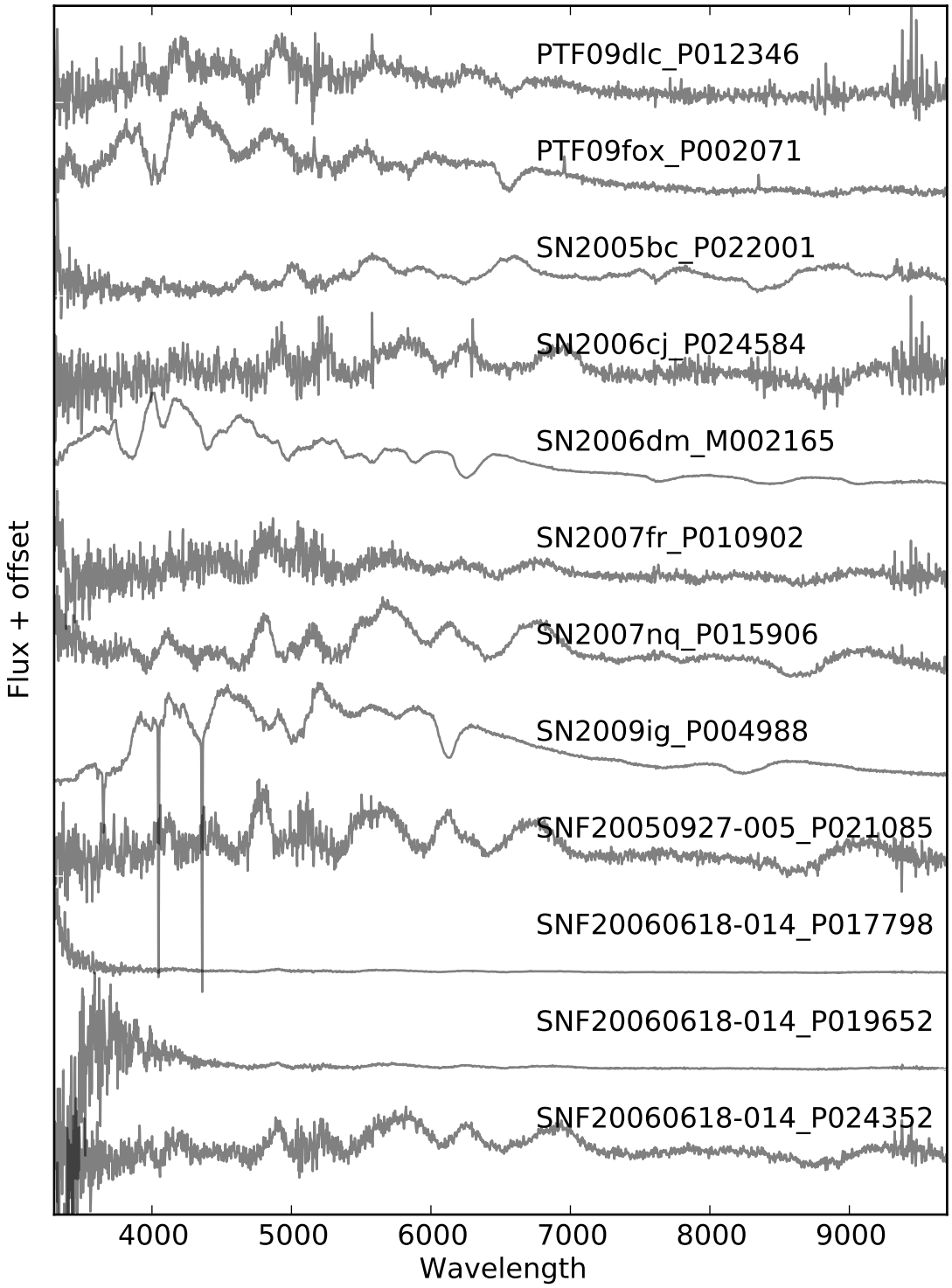

Figure 2.1 Spectra that are removed in the initial visual scan for quality.

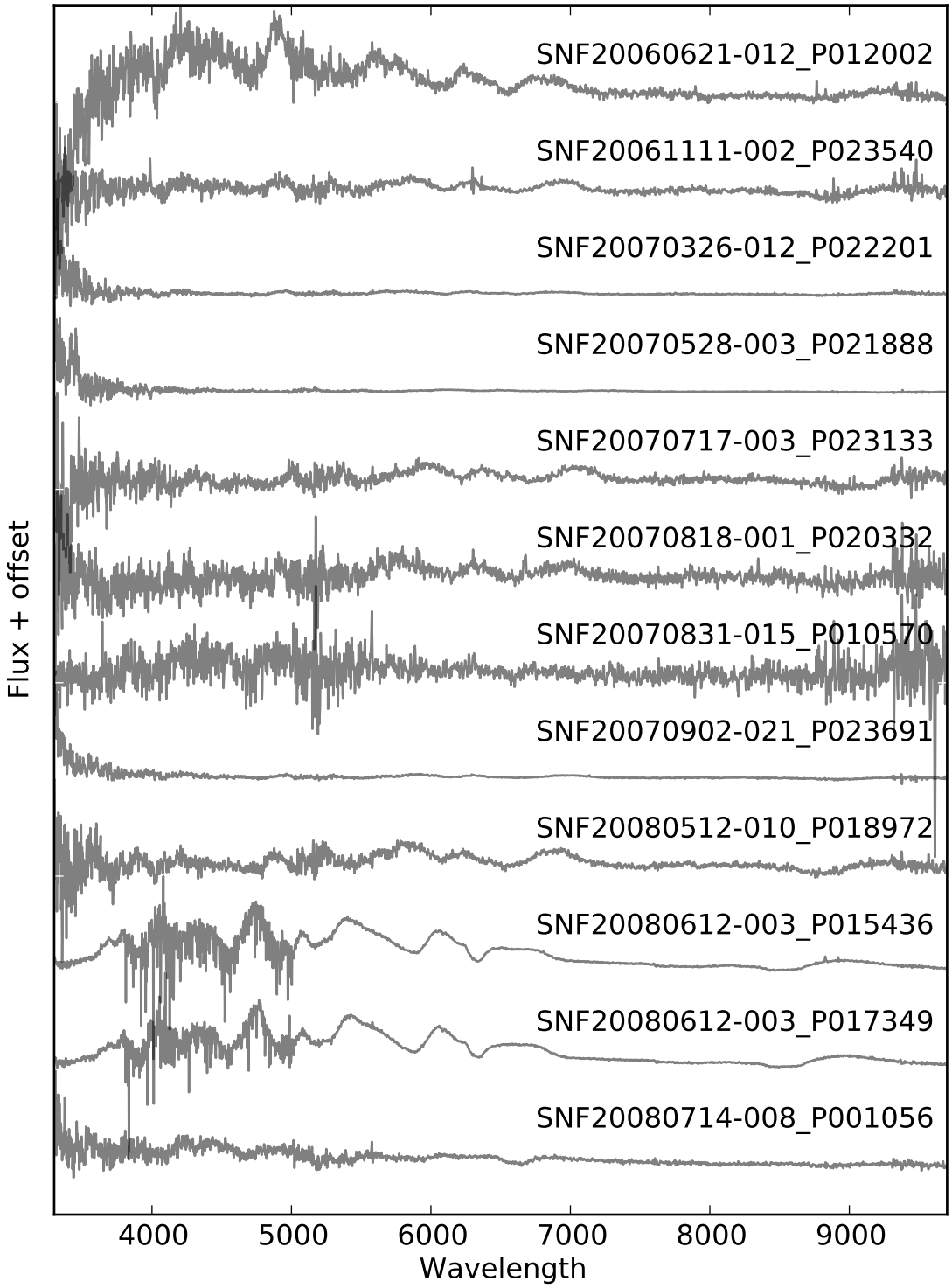

Figure 2.2 Spectra that are removed in the initial visual scan for quality.

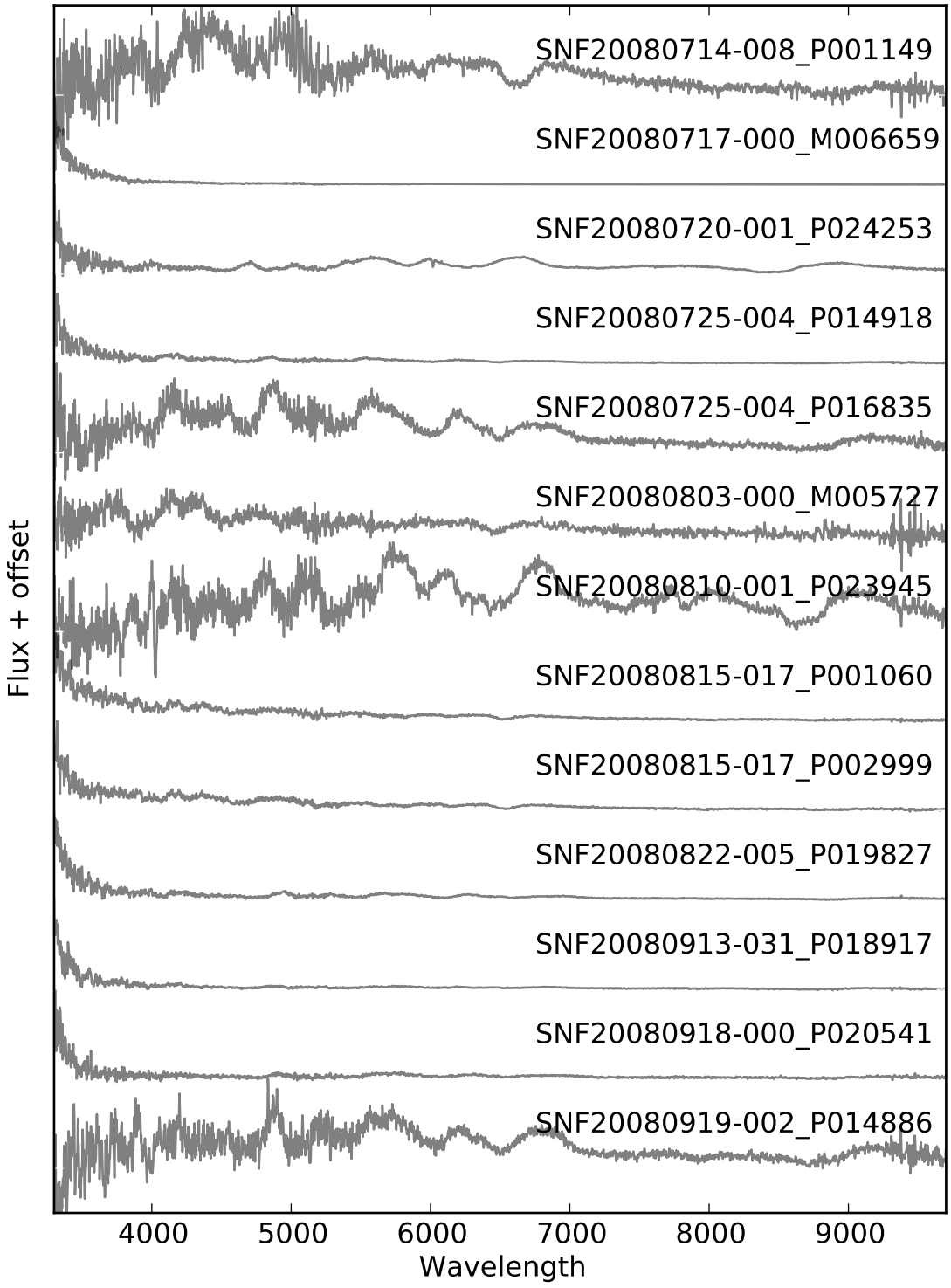

Figure 2.3 Spectra that are removed in the initial visual scan for quality.

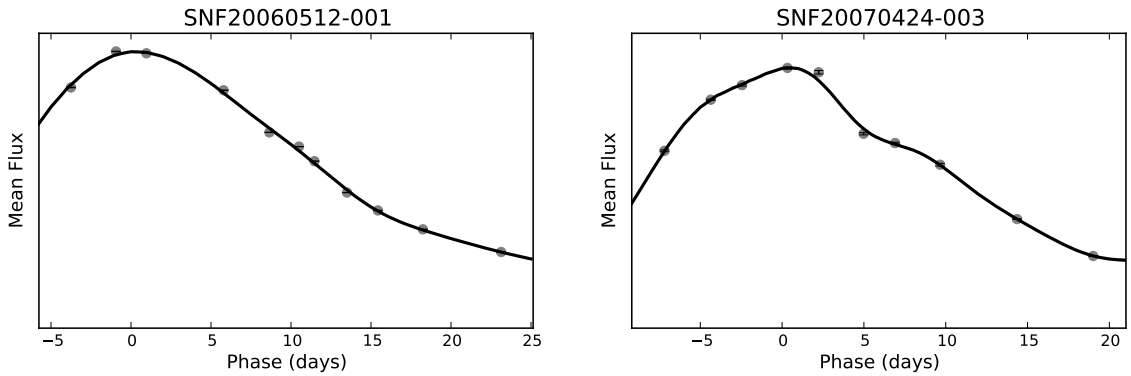

Figure 2.4 Wavelength-averaged Gaussian Process predictions for two supernovae. Left panel shows the desired smooth bolometric behavior; right panel shows an example lacking such smoothness, resulting in the rejection of this supernova.

For nine supernovae we found that removing one spectrum alone significantly improved the overall GP behavior; we drop these spectra in order to keep these SNe in the analysis. There were an additional nine supernovae whose GP models could not be improved by the removal of any single spectrum and so we remove these SNe from the sample.

In the long run we would also want to find automated techniques that would filter out bad and less than ideal data, but for the purposes of this analysis our goal is purity over completeness and as we complete the data quality cuts before examining the brightness scatter results, we are confident in our method to find a clean subset. What we would not want is to have a supernova appear as an outlier in our final analysis that has some questionable data, for if we did we would be tempted to throw it out. By completing a draconian by-eye scan of the data, we ensure that no such supernovae will be in our final sample.

Additionally, an obvious further extension of this analysis is to test if the results we find hold for increasingly less stringent data coverage and quality cuts. Since we complete our quality and coverage cuts before proceeding with the analysis, we are confident that we are not biasing our results, simply ensuring that we have the most pure sample of good data. This is the power and safety of a blinded analysis.

2.3.3 Final Sample

After all coverage and quality cuts we have 74 supernovae (out of the original 132) remaining. Part of the data release that we use has the samples split into training, validation, and auxiliary sub samples. The auxiliary subsample is for SNe that do not have a sufficiently good SALT2 light curve fit but that are otherwise trustworthy. The training and validation subsamples represent an equal split of all the SNe that have good light curve fits. (Much work has been put into ensuring that the training and validation subsamples are representative of each other.) We split the data in this way so that exploratory analyses can be done with only the SNe in the training sample. Then when the analysis is finalized, it is applied to the

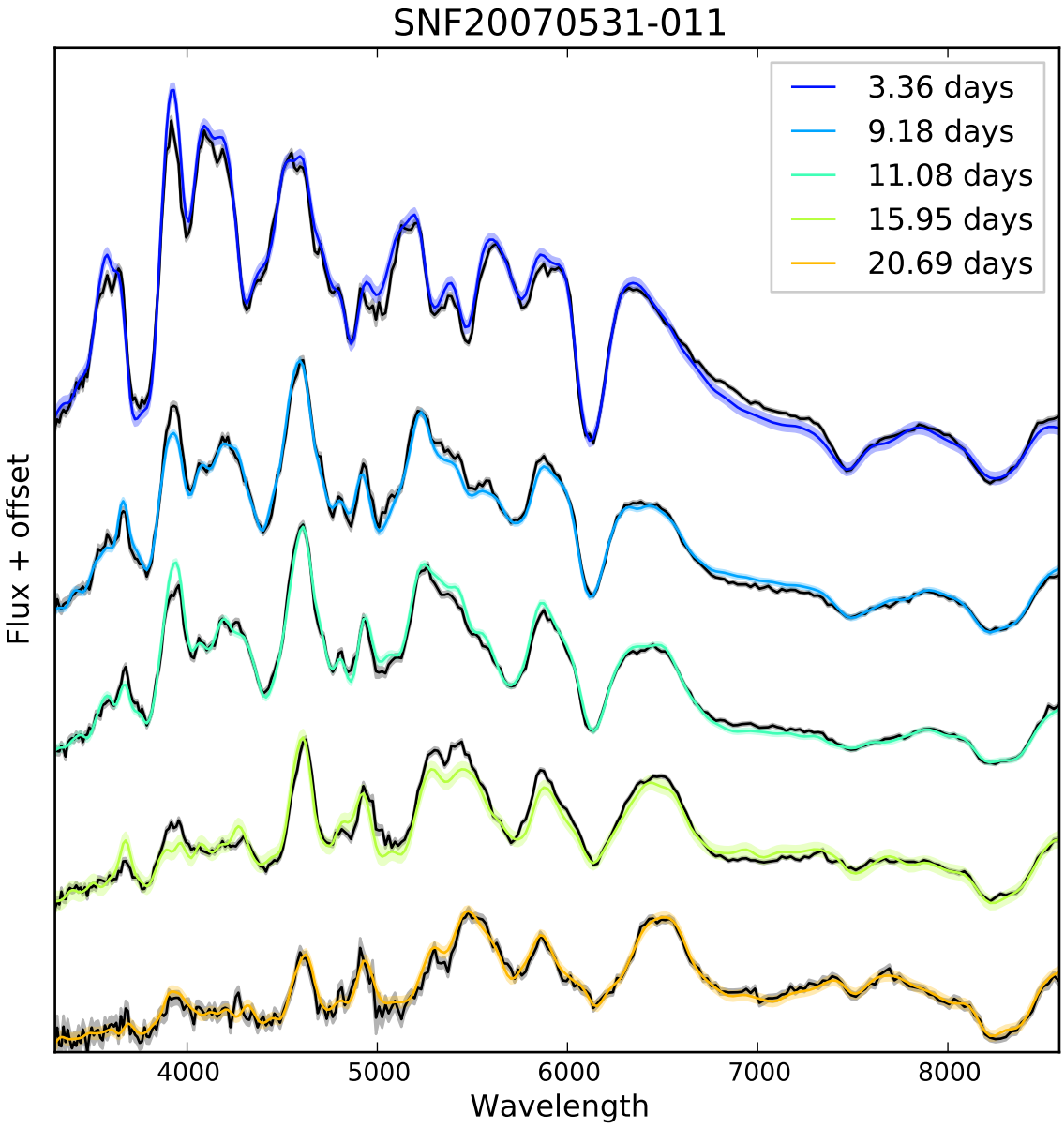

Figure 2.5 Leave one out test results for SNF20070531-011, a relatively high signal to noise supernova on which the Gaussian Process performs well: the Gaussian Process does reasonably well at predicting the features shapes, as well as the overall flux level. The data are in black and in color is the GP prediction at that phase when the corresponding data are left out. Note that the first and last data phases are excluded, as we do not expect the GP to be able to extrapolate the endpoints well.

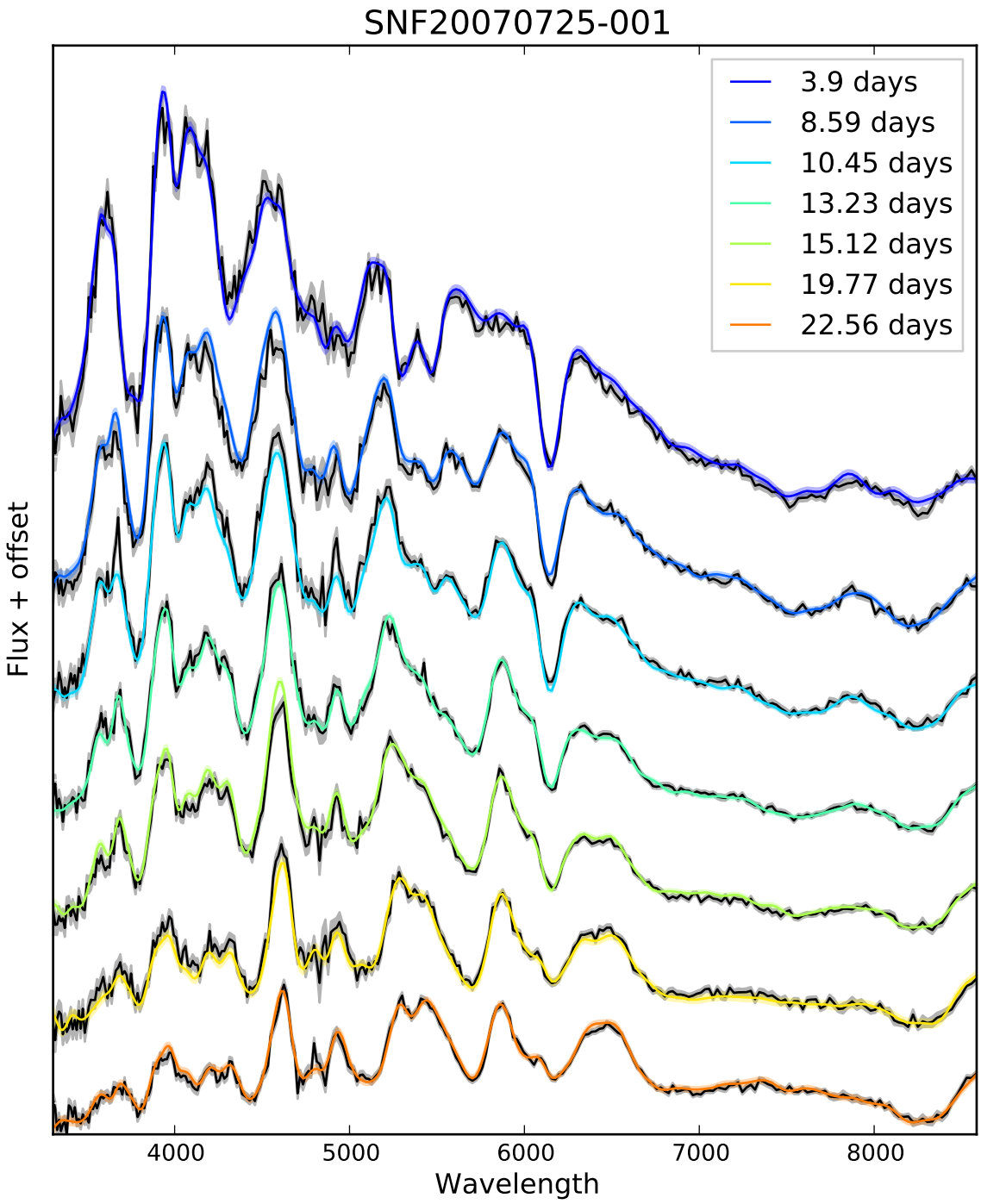

Figure 2.6 Leave one out test results for SNF20070725-001, a lower signal to noise supernova on which the Gaussian Process performs well. The data are in black and in color is the GP prediction at that phase when the corresponding data are left out. Note that the first and last data phases are excluded, as we do not expect the GP to be able to extrapolate the endpoints well.

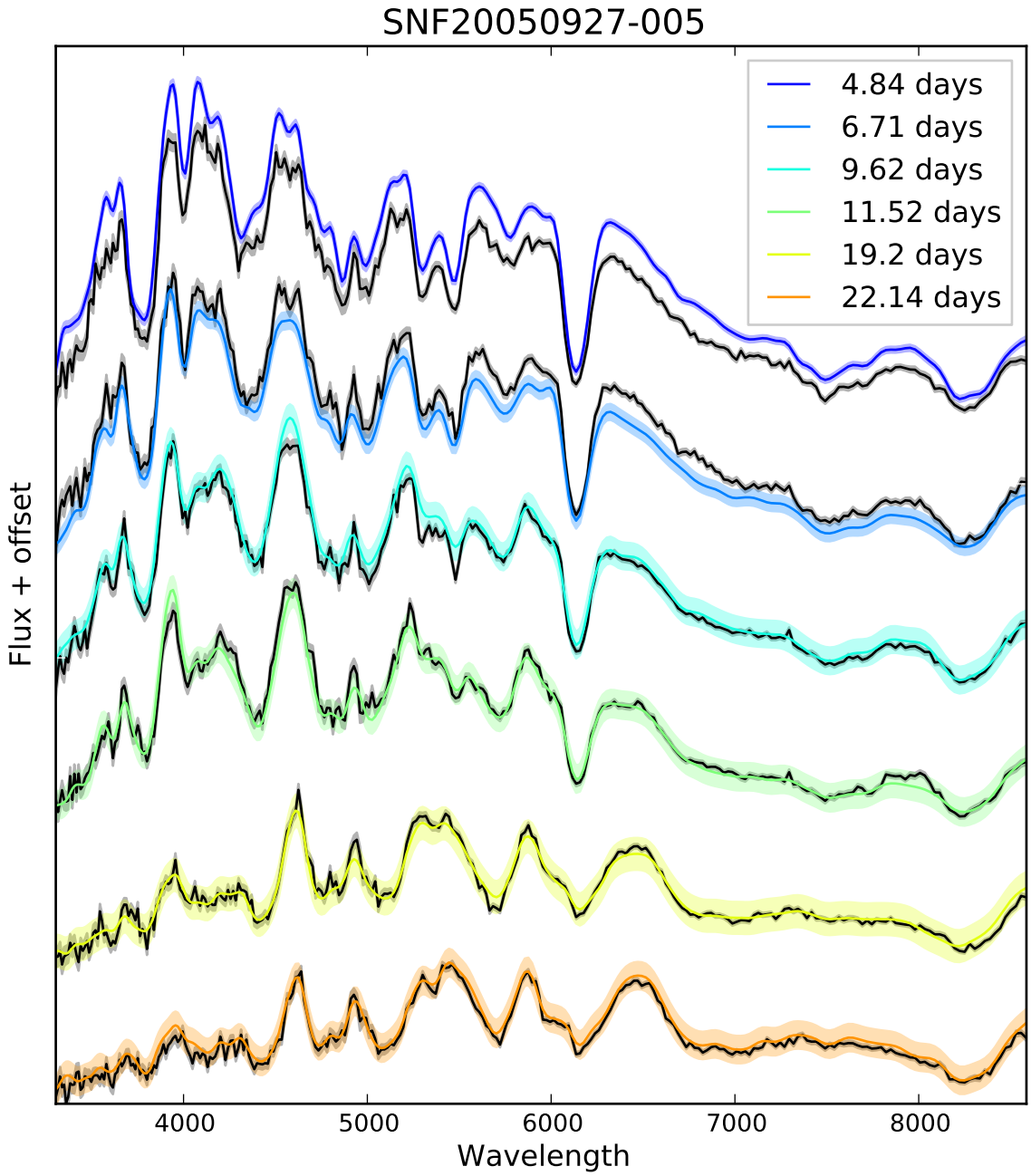

Figure 2.7 Leave one out test results for SNF20050927-005, a supernova that cannot be modeled well by the Gaussian Process: the Gaussian Process is unable to reconstruct the overall flux levels. The data are in black and in color is the GP prediction at that phase when the corresponding data are left out. Note that the first and last data phases are excluded, as we do not expect the GP to be able to extrapolate the endpoints well.

validation SNe to act as an independent test and ensure the result was not simply tuned to the training sample. In this analysis, we are not dependent on good light curve fits, so we can use the auxiliary SNe as well as the training and validation SNe. Of the 74 SNe that pass the cuts, 37 of are in the training sample, while 30 are in the validation sample and 7 are in the auxiliary sample.

Later in the analysis we determined that the lowest redshift supernovae could be problematic due to the uncertainty in their absolute luminosity from their peculiar velocity. Although we do de-weight supernovae based on their peculiar velocity, seeing as our goal is to achieve a pure (not complete) sample, we institute a final cut requiring SNe to be above 0.03 in redshift. This leaves 60 supernovae (29 in the training set) with which we proceed with the analysis.

After the low-redshift cut, four of the remaining supernovae are in the auxiliary sample. In case of concern that including the auxiliary supernovae only in the validation sample while none are in the training sample, as will be discussed in Chapter 4, none of them have sufficient pairs to be involved in the WRMS calculation. Two are super-Chandrasekhar-mass candidates (having luminosities well above the standard range for Type Ia Supernovae) and are beyond our normal redshift cut-off; one has peculiar spectral features and is not a good match with any other supernovae; the remaining one does not have highly peculiar features, but is nonetheless not able to find sufficient good pairs. In retrospect, the auxiliary supernovae need not to have been included, but a priori we had no reason to neglect them from the sample.

Chapter 3

Training Set Analysis and Results

3.1 Training Set Pairs

For the first stage of the analysis, we use only the supernovae in the training set. This allows us to refine our method on part of the sample while reserving a portion (in this case half) of the data for later validation, thus protecting against tuning our results. There are 812 (29x28) potential supernova pairs in the training set. The usual division by two does not apply here because for each supernova we compare its data with the GP-prediction of every other supernova (predicted at the phases where the first supernova has data). Note that this means that pairs of supernovae are compared twice, once with each supernovae interpolated to the other's observation epochs.

Thus, in comparing each supernova to each other supernova, we are in some ways double counting, as a GP-prediction of SN_B at the phases of SN_A is compared with the data of SN_A, and vice versa. However, comparing GP-prediction with GP-prediction (i.e. SN_A and SN_B both predicted at some arbitrary phases), would likely serve to wash out the desired signal, as the GP-prediction does a smoothing as well as an interpolation.

Since a GP prediction sufficiently far away from input data will simply yield the mean function with a large uncertainty, we do not allow extrapolation by more than two days. I.e., if SN_A has data at phases {-8, -4, 0, 4, 8, 12, 16} days and SN_B has data at phases {-2, 1, 4, 7, 10} days, we would use only the data for SN_A that is between -4 and +12 days. Enforcing the coverage cuts from the previous section, i.e. requiring that there be at minimum five spectra, means that some of the potential pairs are not viable due to an insufficient overlap in phase coverage.

The goal in comparing supernovae to each other is to find pairs that are spectroscopically similar at all phases. Any such pairs would be considered "twins." What we want to know is if these twins have a similar absolute magnitude, as we would expect, since spectra are a window into the explosion physics. Since our data are spectrophotometric, and since there may be extrinsic dust reddening in play, for each pair we fit for a scale factor (κ) to measure any magnitude difference and a Cardelli-like color difference ($\Delta E(B-V)$) to measure any standard dust reddening using the following χ^2 equation:

$$\chi^2 = \sum_{p_i} \sum_{\lambda_j} \frac{[f_A(p_i,\lambda_j) - \alpha(\kappa, \Delta E(B-V))\ f_B(p_i,\lambda_j)]^2}{\sigma_A(p_i,\lambda_j)^2 + \alpha(\kappa,\Delta E(B-V))^2\ \sigma_B(p_i,\lambda_j)^2}, \tag{3.1}$$

where f_A (σ_A^2) are the data flux (variance) of SN_A, f_B (σ_B^2) are the GP-predicted flux (variance) of SN_B, p_i are the phases of SN_A, λ_j are the wavelength elements (from 3300Å to 8600Å in 1000 km s^{-1} bins), and

$$\alpha(\kappa, \Delta E(B-V)) = \kappa\ 10^{-0.4(a_\lambda + b_\lambda/R_V)R_V \Delta E(B-V)}, \tag{3.2}$$

where a_λ and b_λ are functions of lambda and are from Cardelli et al. [1989]. We fix the value of R_V to 3.1 so the only unknowns are κ and $\Delta E(B-V)$. (Note that though not presented in Equation 3.1, we actually weight spectra differently at different phases; this will be discussed further in a later section.)

This χ^2 is also a natural way to rank the SN pairs, though we must use χ^2/dof, as the number of spectra per comparison differs. When we use the χ^2 values from the fitting discussed above, none of our pairs are perfect matches (in the sense of $\chi^2/dof = 1$) When

we rank them, we see that the lowest χ^2/dof pairs are overwhelmingly those involving data from a SN with lower signal to noise.

Our goal for a twinness metric, however, is that the best ranked pairs would be independent of the signal to noise; i.e. that the best pairs would have a representative spread of signal to noise values. One way of enforcing this is to alter the χ^2 statistic by adding an error floor in quadrature with the variance spectrum and GP produced errors. For our error floor we choose to use a percentage of the flux, as a flat error floor would give too much leeway to spectra at later times (where the flux is lower), and we already expect the spectra to match well at later times.

We tested adding error floors from 2% to 20% in steps of 2%. When the additional error floor becomes too large, the distribution will begin to favor high signal to noise supernovae (as opposed to low signal to noise supernovae when the error floor is too small.) We found that 12-14% produced a ranking of pairs for which the best 50 pairs had a signal to noise distribution most similar (using a K-S test) to that of the training supernovae. For this analysis we choose to add a 12% error floor in quadrature with the variance spectrum.

3.2 Twinness Metric

For our twinness metric ξ, then, we use the following:

$$\xi = \sum_{p_i} \sum_{\lambda_j} \frac{[f_A(p_i,\lambda_j) - \alpha(\kappa, \Delta E(B-V))\ f_B(p_i,\lambda_j)]^2}{\sigma_A^2(p_i,\lambda_j) + (0.12\ f_A(p_i,\lambda_j))^2 + \alpha(\kappa,\Delta E(B-V))^2\ \sigma_B^2(p_i,\lambda_j)} / (N_p * N_\lambda - 2), \tag{3.3}$$

where the variable names remain the same as before, and we are dividing by the number of degrees of freedom, which is equal to the number of phases (usually $\sim$8 to 10) multiplied by the number of wavelength elements (288), minus two (as two parameters are fit in the minimization). We divide by the number of degrees of freedom because different pairs have different numbers of spectra included in the ξ calculation, and as such would not be readily comparable otherwise.

Recall that we fit SN_A to the Gaussian process prediction of SN_B at the phases of SN_A; from this we get a κ that we will call κ_{AB} and a ξ we call ξ_{AB}. We also do the reverse: we get a κ_{BA} and ξ_{BA} when we fit SN_B to the Gaussian process prediction of SN_A at the phases of SN_B. To rank our supernova pairs we must take into account that different pairings will have different number of phases being compared, so we must divide by the degrees of freedom so we are appropriately comparing different pairs. We combine these two ξ values into one metric, dividing out the total number of degrees of freedom:

$$\xi'_{AB} = \frac{\xi_{AB} + \xi_{BA}}{dof_{AB} + dof_{BA}} \tag{3.4}$$

As this is a subtlety easily understood, we now drop the prime and from here on refer to ξ_{AB} as the per degree of freedom twinness metric for SN_A and SN_B.

These ξ values are how we order the pairs from "best pairs" to "worst pairs". Figures 3.1 to 3.3 show three randomly chosen pairs out of the top 50. The level of feature overlap is impressive, much better than current theoretical models of supernova explosions

are able to achieve. For comparison, Figures 3.4 to 3.6 show three pairs in increasing ξ value, to illustrate the progression from twin-like pairs to pairs that are certainly not twins. (In what follows, we are actually using an optimal weighting of the data at different phases that will be discussed at length in a later section.) If these "best pairs" are in fact twins, their brightness spread will be smaller than the "worse pairs."

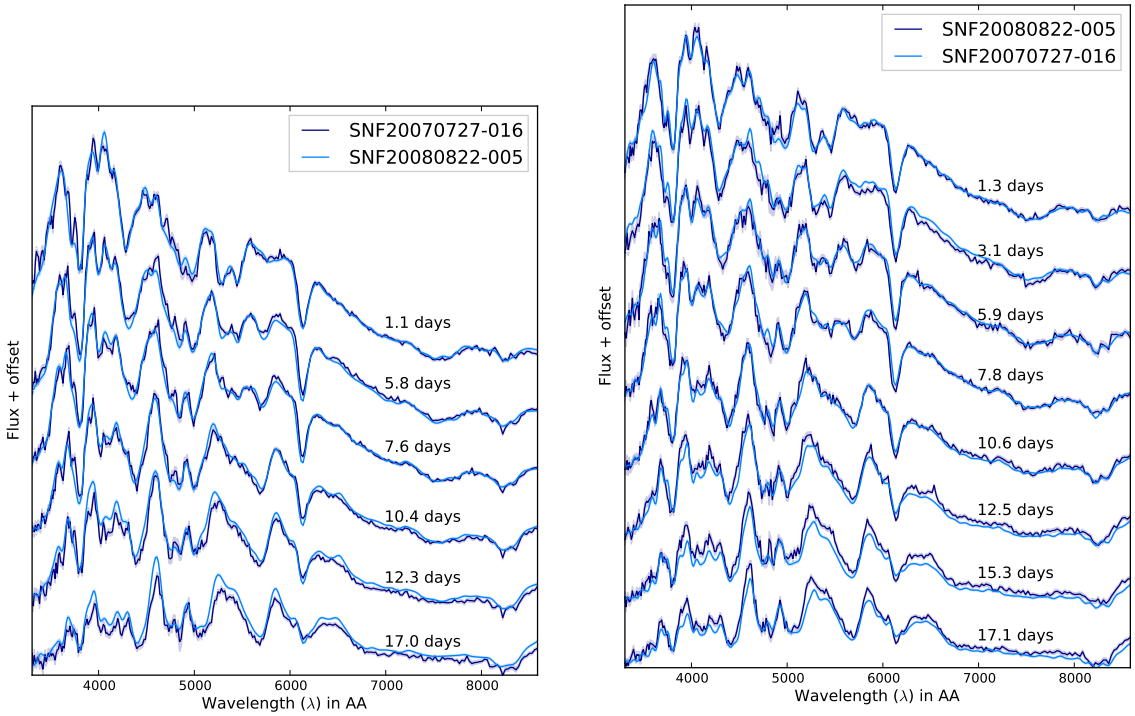

Figure 3.1 Example of two well-matched supernovae from the training set. The left panel shows data for SNF20070727-016 in dark blue. The Gaussian process prediction of SNF20080822-005 at the phases of SNF20070727-016 is shown overlaid in light blue. Note that there are error snakes for both the data and the GP fluxes. Phases are listed with respect to the date of maximum brightness. The right panel shows the reverse: SNF20070727-016 predicted at the phases of SNF20080822-005. The ξ value for this pair is 15.5, in the lowest 5% of pairings, sufficiently low that it is considered a twin.

3.3 Brightness Difference Results

Now that we have our supernova pair ordering, we can assess the extent to which more twin-like pairs (those with low ξ) have more similar brightnesses. Recall that when comparing one supernova to another we fit for a scale factor κ. We have previously normalized the fluxes to a standard distance based on redshift; for this low-redshift supernova data set the exact choice of cosmology makes a negligible difference, but we chose $\Omega_M = 0.28$ and $\Omega_\Lambda = 0.72$. Then, since our data are spectrophotometric, this κ represents the difference in absolute

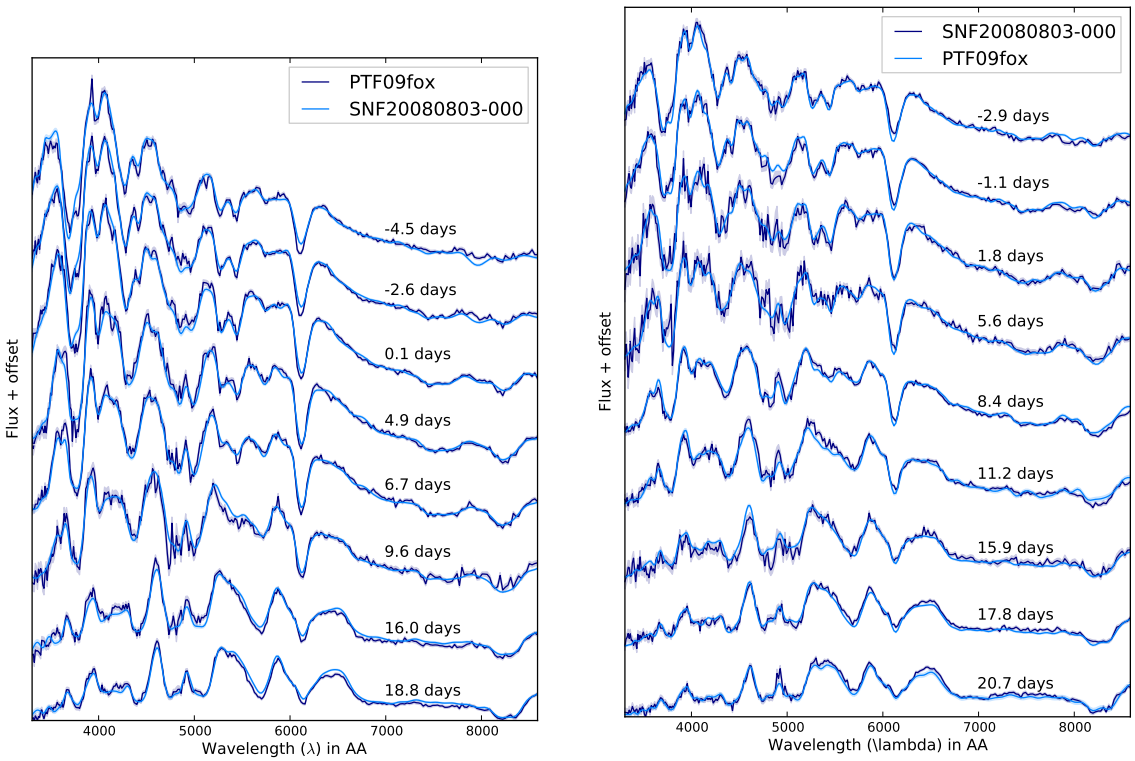

Figure 3.2 Example of two well-matched supernovae from the training set. Colors are as in Figure 3.1 but for PTF09fox and SNF20080803-000 respectively. The ξ value for this pair is 16.1, in the lowest 5% of pairings, low enough to be considered a twin.

brightness of the two supernovae. If κ is 1, the supernovae have a zero brightness difference; κ less than or greater than one corresponds to a magnitude difference of

$$\Delta M = -2.5 log_{10} \kappa. \tag{3.5}$$

The error on this brightness difference is determined from the errors on the fit parameters (κ and $\Delta E(B-V)$), the peculiar velocities (with a 300 km/s error), and a small calibration error from our standard star measurements:

$$\sigma_{\Delta M} = \sqrt{\sigma_M^2 + \sigma_{host}^2 + \sigma_{pv1}^2 + \sigma_{pv2}^2 + \sigma_{calib}^2} \tag{3.6}$$

where

$$\begin{aligned} \sigma_M &= |-2.5 log_{10}(\kappa) - -2.5 log_{10}(\kappa + \sigma_\kappa)| \\ \sigma_{host} &= 4.1 \sigma_{\Delta E(B-V)} \\ \sigma_{pv} &= 5/log(10)300/3e5/z = 0.00217/z \\ \sigma_{calib} &= 0.025 \end{aligned} \tag{3.7}$$

Note that the fit errors (σ_κ and $\sigma_{\Delta E(B-V)}$) are subdominant to the peculiar velocity errors, which comprise roughly 80% of the error budget.

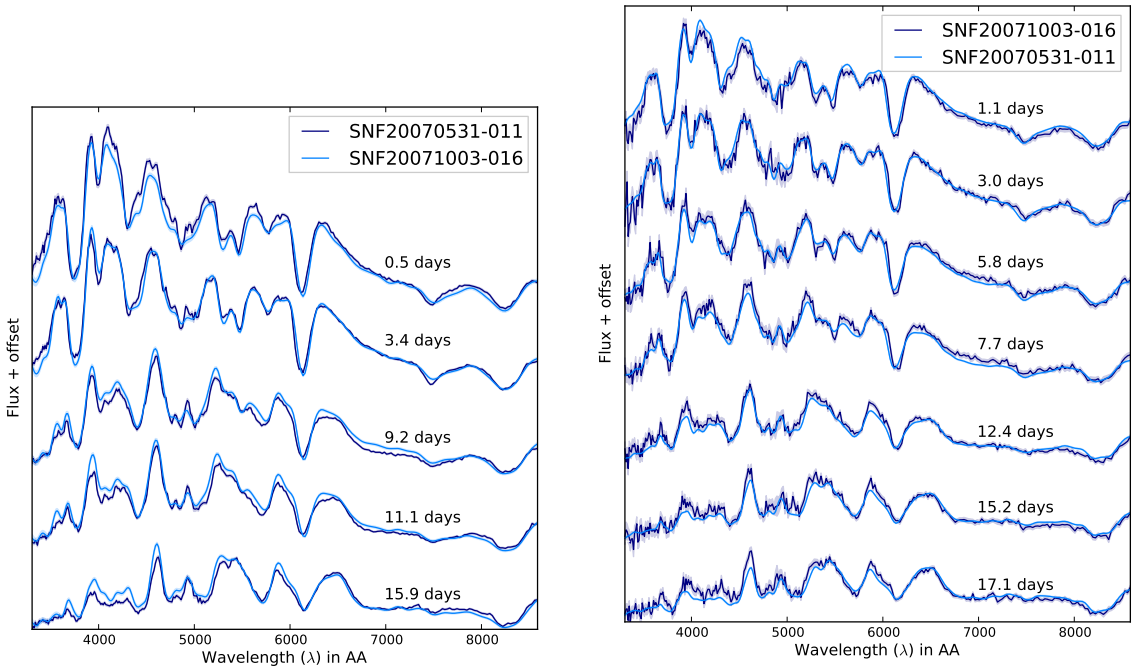

Figure 3.3 Example of two well-matched supernovae from the training set. Colors are as in Figure 3.1 but for SNF20070531-011 and SNF20071003-016 respectively. The ξ value for this pair is 24.9, in the lowest 10% of pairings, low enough to be considered a twin.

Figure 3.7 shows, in the top panel, a scatter plot of the ΔM values as a function of twinness metric value. What we expect to see is that for low ξ there are fewer high ΔM points than for high ξ, which we can see qualitatively from the top panel as well as from the histograms in the lower panel. The lower panel shows the distribution of ΔM values for different cut-offs in ξ. The histograms on the right have a larger spread, indicating there are more high ΔM pairs at higher ξ values. Note that low values of ΔM at high ξ are not surprising. Given that our ΔM is calculated from κ, the fitted scale factor, it is entirely plausible that though two supernovae do not have matching spectral features, their fitted scale factor can be close to one. In other words, the twins hypothesis proposes that spectroscopically identical supernovae have similar brightnesses, not that non-spectroscopically similar supernovae do not have similar brightnesses.

A simple measure of the spread in ΔM as a function of increasing ξ shows that better ranked pairs do indeed have a lower brightness spread. However, to use the method to its full power, we calculate the spread as we would if we were doing this analysis with a high-redshift set of supernovae.

In that case, for each high-redshift supernova we would calculate its brightness relative to all the low-redshift supernovae it matches well (brightness difference being the ΔM obtained from fitting for κ in Equation 3.1). By taking a weighted average of these ΔMs, we have an average brightness difference (called μ) for each high-redshift supernova. (Note that because the redshifts have been normalized out μ would be zero for a perfect standard candle with

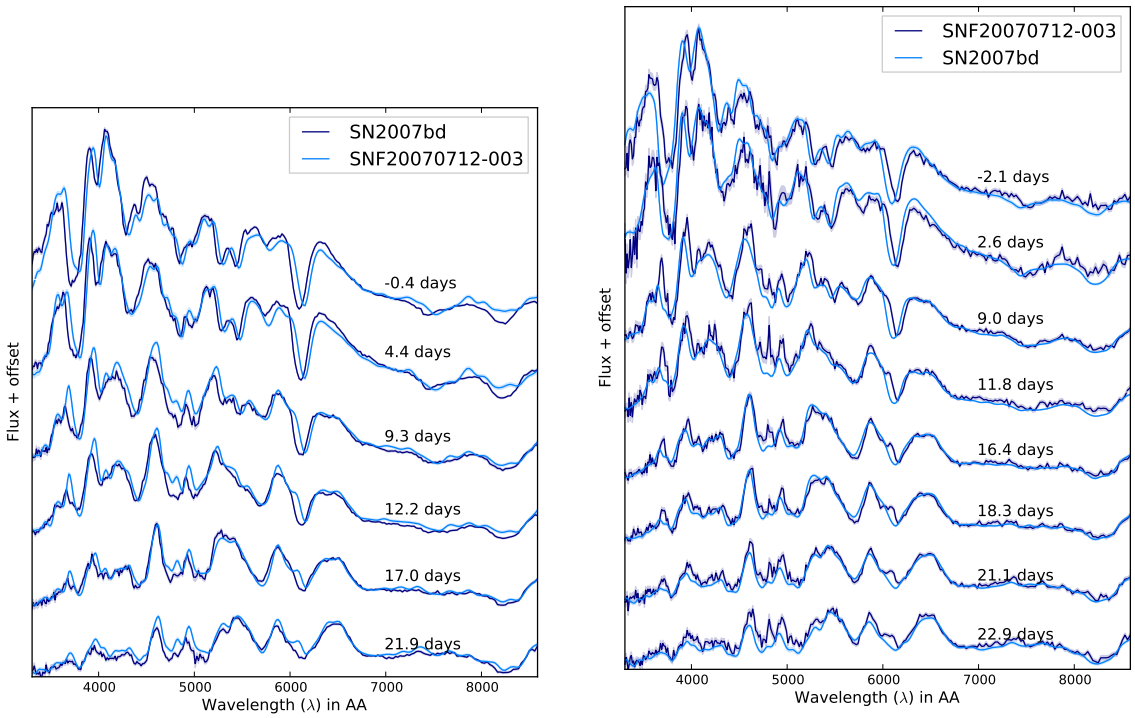

Figure 3.4 Example of two somewhat poorly-matched supernovae from the training set. Colors are as in Figure 3.1 but for SN2007bd SNF20070712-003 respectively. The ξ value for this pair is 43, which corresponds to the 45th percentile of pairings, too high to be considered a twin.

no measurement errors.) The spread of those μs over the whole high-redshift sample is the measure of how well the standardization method works.

To mimic this within our low-redshift sample, we treat each supernova in turn as though it were the high-redshift supernova. We want to know if indeed the best ranked pairs have a lower brightness difference spread (lower spread in μ) than the worst ranked pairs, and if so, how low is that spread. To test this, we begin by only using the very best pairs we have. We find all the supernovae that have at least four pairs (so that their μs are reasonably well defined; we tested that the results are similar with a requirement of three or five pairs) and calculate the spread, using the weighted root-mean-square (WRMS) as our measure of spread. (It is the weighted RMS of a set of weighted means.)

We calculate this WRMS as a function of ξ: we let in worse and worse pairs to the calculation of the μs. If the twins hypothesis is true, we expect the WRMS(ξ) to increase with ξ, as more and more non-twin pairs are included.

Figure 3.8 shows the WRMS as a function of ξ for this training set analysis. As predicted, the WRMS at low-ξ is better than at high-ξ. Note that figure shows results up to ξ of 46, which only represents about half the total pairings (183 out of 346 pairs). At the transition ξ where the WRMS increases from $\lesssim 0.10$ mag to $\lesssim 0.15$ mag, there are 77 pairs included. The asymptotic WRMS (with all pairs) is 0.149 ± 0.012 mag, comparable to the value measured

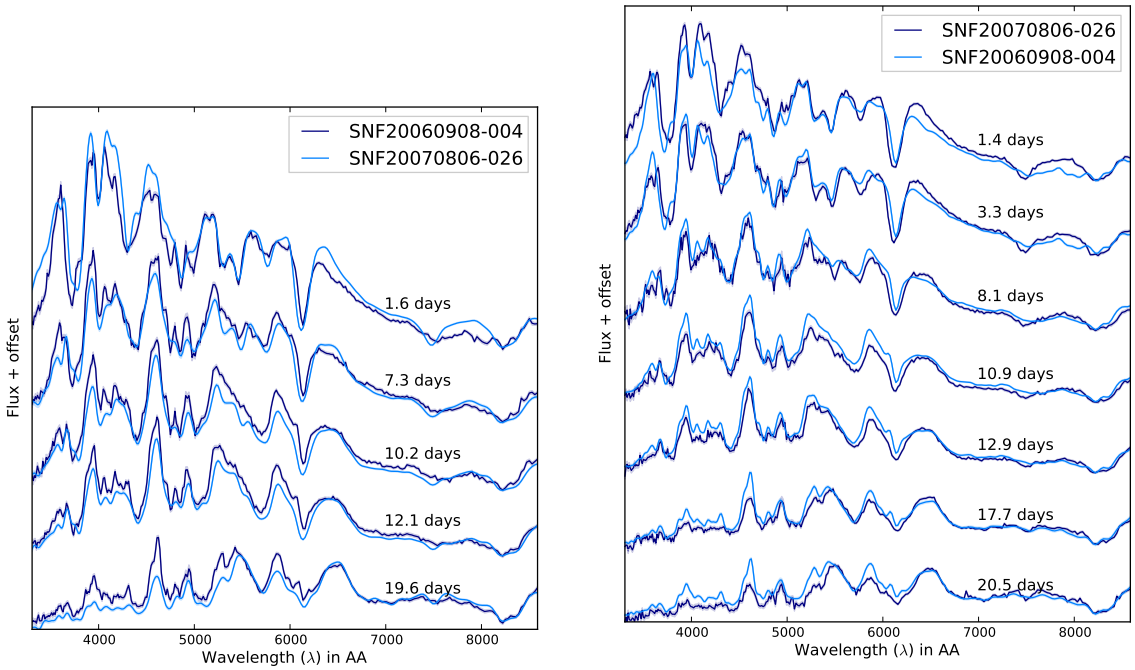

Figure 3.5 Example of two poorly-matched supernovae from the training set. Colors are as in Figure 3.1 but for SNF20060908-004 and SNF20070806-026 respectively. The ξ value for this pair is 56, which corresponds to the 65th percentile of pairings, too high to be considered a twin.

using the standard SALT fits and Hubble residuals. As you can see from the figure, the WRMS has reached close to this asymptotic value within the plotted range.

It is interesting to know how many different supernovae are contributing to the result shown in the figure. At the transition value around ξ of 30, 19 of the 29 training set supernovae have at least four pairs and are included in the WRMS calculation. Of those 10 lacking sufficient pairs, six have some pairings up to the cut off, so only four are in no way contributing to the result. It is encouraging that the result is not obtained using a small fraction of the sample, but rather with the large majority of the objects participating in some form. The fraction of supernovae with sufficient pairs should increase as the sample size increases so this will be revisited with the full sample.

3.4 Optimal Weighting

Although one might try the analysis described above giving equal weight to early and late time spectra of Type Ia SNe are known to be considerably more homogeneous than spectra at early (near-maximum and pre-maximum) phases. Thus giving additional weight to early spectra over late spectra ensures we are using the data in an optimal manner.

Though at first we attempted an ad hoc weighting scheme, we realized the optimal weighting could be determined from the data themselves, by doing a WRMS analysis in bins

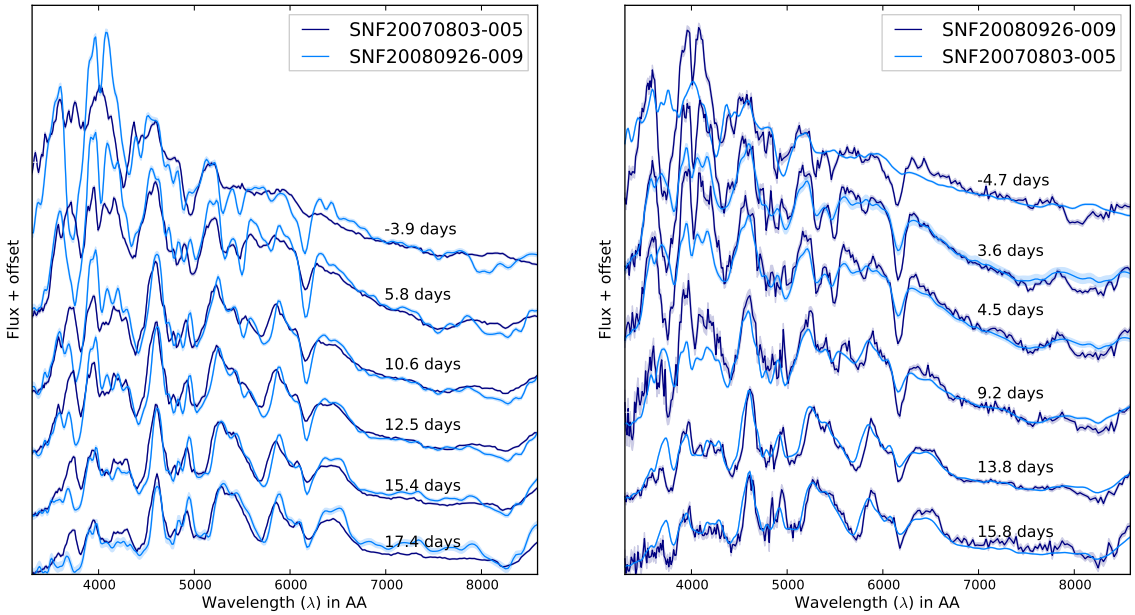

Figure 3.6 Example of two very poorly-matched supernovae from the training set. Colors are as in Figure 3.1 but for SNF20070803-005 and SNF20080926-009 respectively. The ξ value for this pair is 135, which corresponds to the 99th percentile of pairings, too high to be considered a twin.

of phase. Phase bins were set to be non-overlapping, sampling every 2.5 days. For example, the +5 days bin would include all supernovae with spectra from +3.75 days to +6.25 days.

The analysis described in the above sections is done in each bin independently: fits for κ and ΔE(B-V) are done for each pair of objects having data in the specified phase range, the pairs are ranked based on their combined ξ value, as in Equation 3.3, and the WRMS of average brightness differences is calculated as a function of increasing ξ. Note that only one pair of spectra are compared for each supernova pair. As such the fitted κ values will be different for a pair that appears in multiple phase bins. To calculate the WRMS in each phase bin, we use the pairs that are sufficiently good to be considered twins; there are roughly 50 such pairs in each bin.

The top panel of Figure 3.9 shows the WRMS results for each phase bin. The color coding is blue at early phase bins progressing to red at late phase bins. To determine the optimal weighting, shown by the purple line in the bottom panel, we do a weighted linear fit to the inverse variance (where the WRMS is taken as the error so the inverse variance is $1/\mathrm{WRMS}^2$. The WRMS value that was used for each phase bin is the median value in a "suitable" ξ range. That range varies for each bin; the lower limit is the ξ value when at least 5 supernovae are participating in the WRMS calculation; the upper limit is the ξ value when 80% of the SNe that will eventually participate are in the WRMS calculation. The end result is not highly-dependent on the weighting scheme; a slightly different WRMS selection, resulting in a different linear fit, does not affect the end results.

The fit result is used as a weighting scheme in the χ^2 minimization, using the linear fit

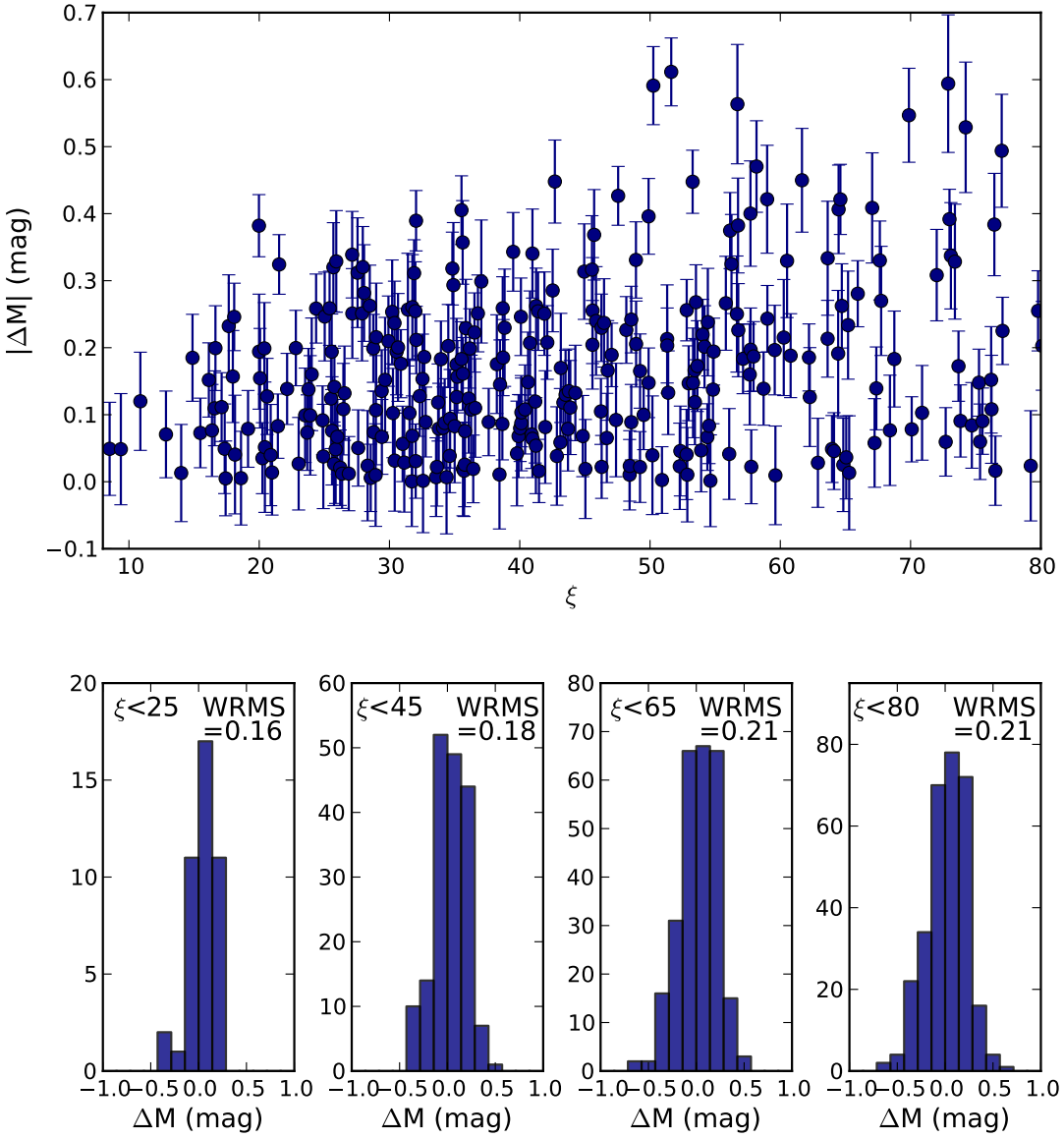

Figure 3.7 Top panel: Scatter plot of ΔM as a function of twinness metric ξ for the training set analysis. Bottom panel: Histograms of ΔM for inclusively larger ξ values, illustrating that the spread in ΔM increases as worse pairs are included.

parameters and the phase of the data spectra. This gives early time spectra more power to determine the κ values, from which we get the brightness difference. We considered flattening off the weighting function before maximum light, out of concern that any very early time spectra would get a very high weight. And although we do have some spectra in the sample that are before -5 days, only 9% of pairings have spectra that early, and when considering only pairs with sufficiently low ξ value to be considered twins, the percentage falls to 4%. So rather than add an additional degree of freedom by flattening the weighting function, we proceed with the simple linear fit.

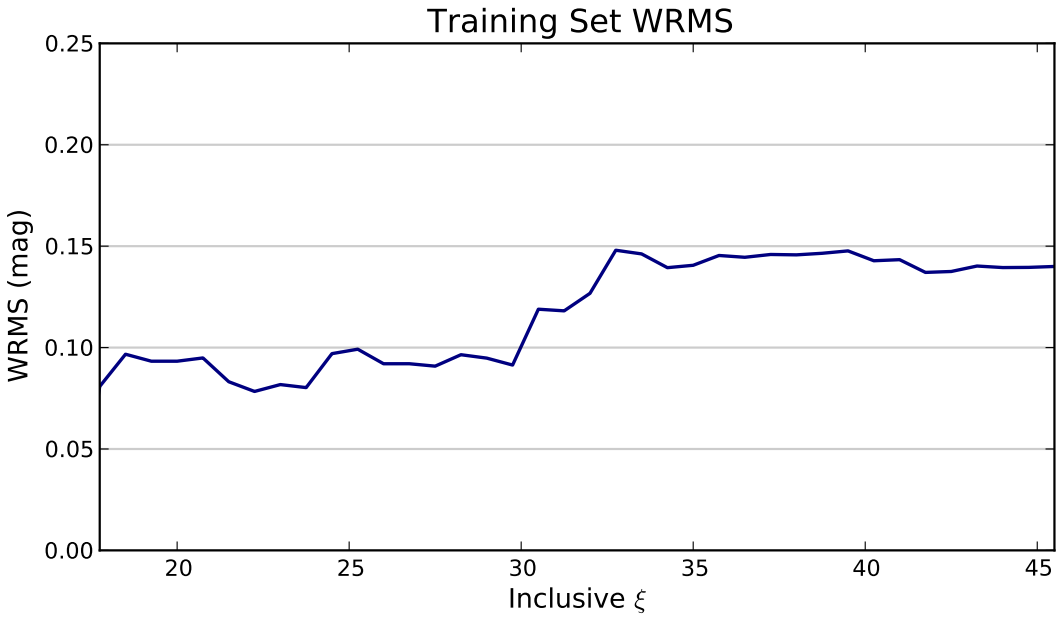

Figure 3.8 Weighted root mean square as a function of inclusive ξ. See text for discussion.

The low-WRMS performance of the early phase bins gives an indication that the entire spectrophotometric series might not be needed to do this kind of analysis. If this were to be the case, it would have positive implications for the future use of this method, as full coverage spectrophotometric timeseries of high-redshift Type Ia supernovae is not on the immediate horizon.

In light of this, we additionally pursue an "at max" analysis, where we pair down our cleaned sample of supernovae and take the subset that have spectra between -2.5 and +2.5 days. An identical analysis is done on this set, with results presented in the next section. However, note that our "at max" sample is not necessarily representative of a high-redshift "at max" sample (nor is our optimally weighted sample), because our cleaning and selection process chose SNe that are well-behaved with respect to our Gaussian Process regression, and we use the Gaussian Process predictions to compare the SNe spectra to each other. A more accurate test of the suitability of such a constrained analysis would be to select all SNe from the data set with a spectrum near maximum and complete this analysis either without a Gaussian Process (i.e. fitting the spectra directly to each other) or with some other method to predict what the SNe would look like at each other's phases.

3.5 Randomization Tests

In order to test the significance of our low-WRMS finding, we do Monte Carlo randomization tests. A naive randomization test would be to randomly re-order the ξ rankings and proceed with the analysis. However, this does not capture the correlations present in the non-randomized pair rankings. The correlations come about because SN_A may be used in the average ΔM of SN_B and vice versa and also because the same SN_A plays a role in

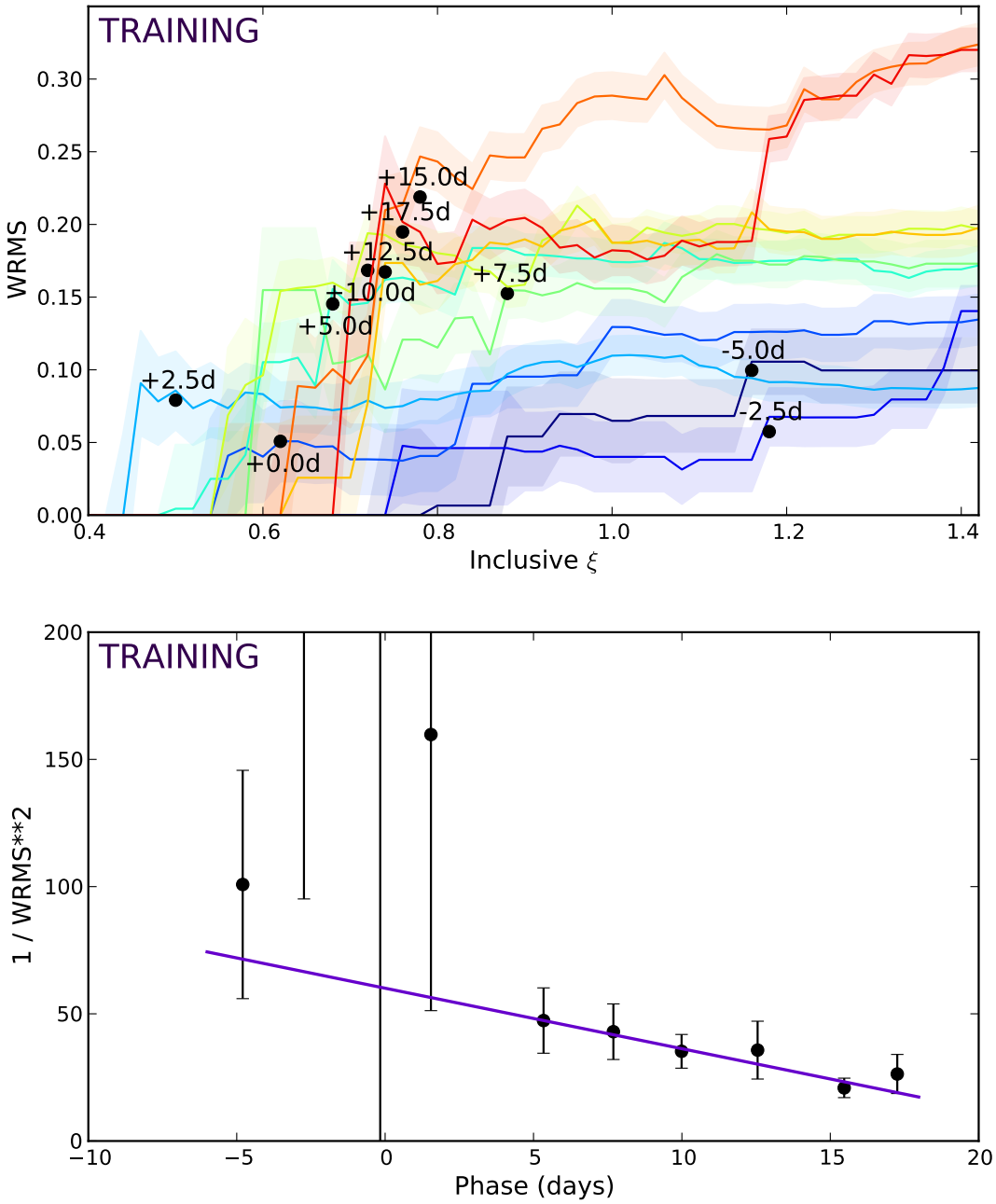

Figure 3.9 Top panel: WRMS as a function of inclusive ξ for different phase bins. The shaded regions are the error on the WRMS values. Each line is labeled by the bin-center value. The black circles show the WRMS values that were used in the lower panel to calculate the optimal weighting function. Lower panel: The purple line is a weighted linear fit to the inverse variance, where the points are drawn from the upper panel. Note that the points around -2.5 days and 0 days are significantly off scale, but their errors are large and consistent with the fitted line.

several other supernova distance modulus estimates besides SN_B. So instead of randomly re-ordering the ξ rankings, we shuffle the supernova identities, making a look-up table. When the analysis wants the pairing of SN_A with SN_B, instead we call the pairing of, say, SN_H with SN_M. Generating hundreds of these shuffled look-up tables and running the analysis allows us to calculate the spread of the randomized results.

However, not all possible supernova pairings have sufficient coverage overlap to allow a fit as done in Equation 3.1. This means that some pairings called for in the look-up table will be empty. We mark these as failed pairing attempts and only use look-up table instances where the total failure rate is less than 10%.

To calculate the significance of our result, we take the mean and standard deviations of the randomization results at each ξ value. Figures 3.10 and 3.11 show the results of the optimally weighted analysis and the near maximum spectra analysis, respectively. The top panel of the figures shows the 1-, 2-, and 3-σ bands of the spread of the randomizations; the thick colored line is the result from the data. The bottom panel shows the pulls (the magnitude dispersion in units of sigma) as a function of ξ.

The significance of the training set results is encouraging. For the optimally weighted analysis, we see a peak significance around 2.8 σ and for the at near maximum analysis we see a peak significance around 3.0 σ. Unblinding the validation set will increase the sample size by a factor of two, so we expect the significance to be roughly $\sqrt{2}$ larger.

We also note there is a floor to how well we can do, set by the errors on ΔM, as calculated in Equations 3.6 and 3.7. For both the optimal weighting and near maximum analyses, that floor is roughly 0.065 mag. When considering only the errors from the peculiar velocity, that floor is closer to 0.045 mag.

3.6 Jackknife Outlier Rejection

Before we "unblind" (look at the results with the full sample), we want to be prepared for various issues we may see, so that we do not have to do much additional analysis on the unblinded sample, allowing it to stand as a verification of our initial result.

One such concern is that there could be individual supernovae that drive the WRMS high and would be obvious outliers. In this early version of the reduction pipeline, an occasional bad calibration could cause such an obvious outlier. To protect against this in the full sample, we developed a jackknife outlier detection using the training sample.

The jackknife is done by proceeding with the analysis but dropping each supernova from the sample in turn. The thin grey curves in the top panel of Figure 3.12 show the WRMS results when throwing out each SN. The darker blue line shows the WRMS when all SNe are included. Between ξ of 20 and 25, there is a curve that drops substantially lower than the others; this indicates that removing that supernova from the analysis would result in a substantial drop in the WRMS in that ξ range.

Many methods for identifying these outlying objects were considered. First we decided to limit the range of ξ over which outliers are detected to be that of "twins"; i.e. we are not interested in catching outliers if they show no strong presence in the low ξ values where we consider our pairs to be twins. The lower limit of this boundary was chosen to be the ξ value where at least five supernovae have sufficient pairs to calculate an average ΔM. The

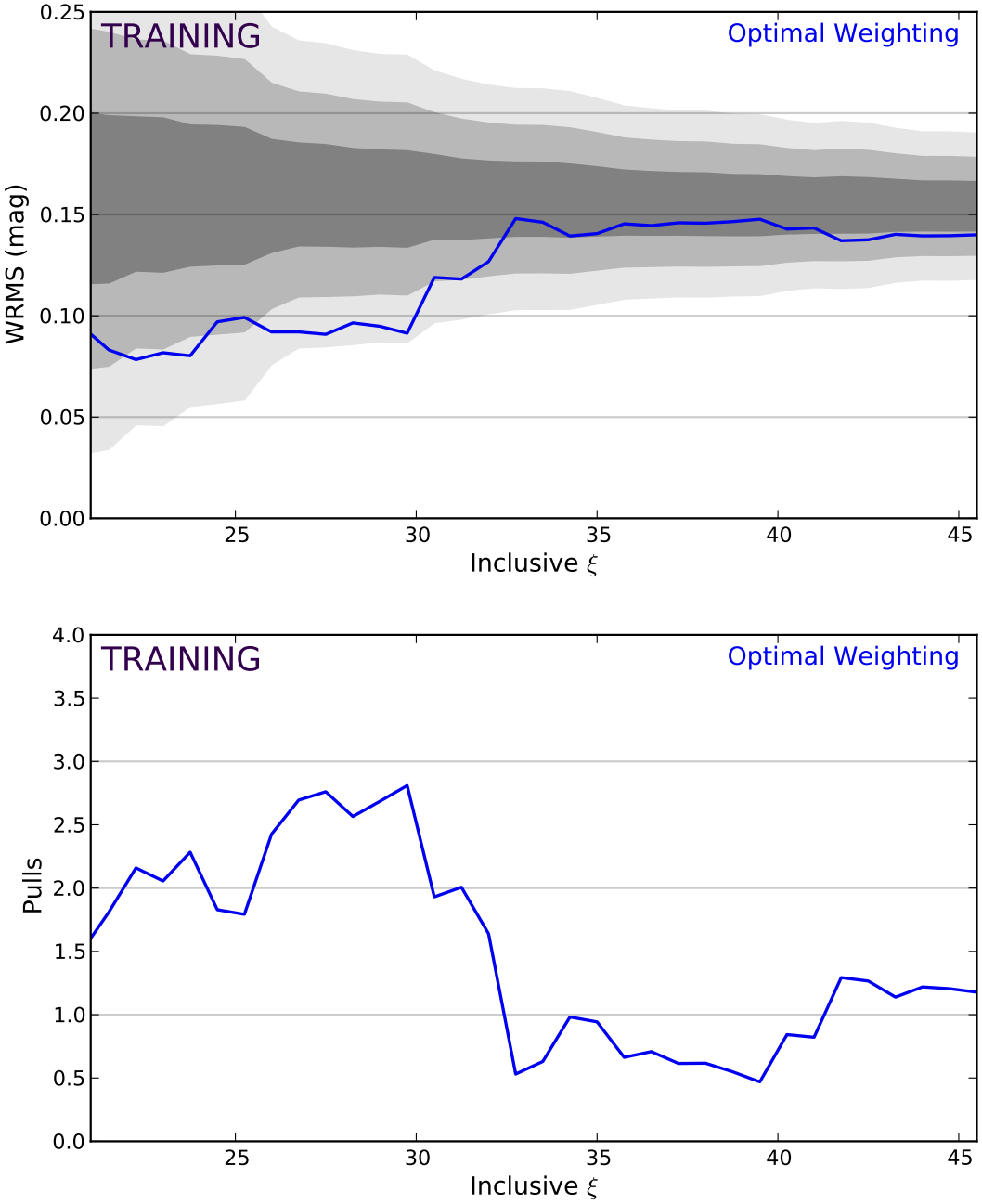

Figure 3.10 Results for the optimal weighting analysis on the training set data with no outlier rejection performed. Top panel shows the WRMS of the data in blue along with the 1-, 2-, and 3-σ error bands from the Monte Carlo randomization tests. Bottom panel shows the pulls as a function of ξ, with a maximum significance of 2.8 σ around inclusive ξ of 30, with a nice low WRMS result around 0.09 mag.

upper limit was chosen to be the ξ value where the maximum significance from the bottom panel of Figure 3.10 drops by 25%.

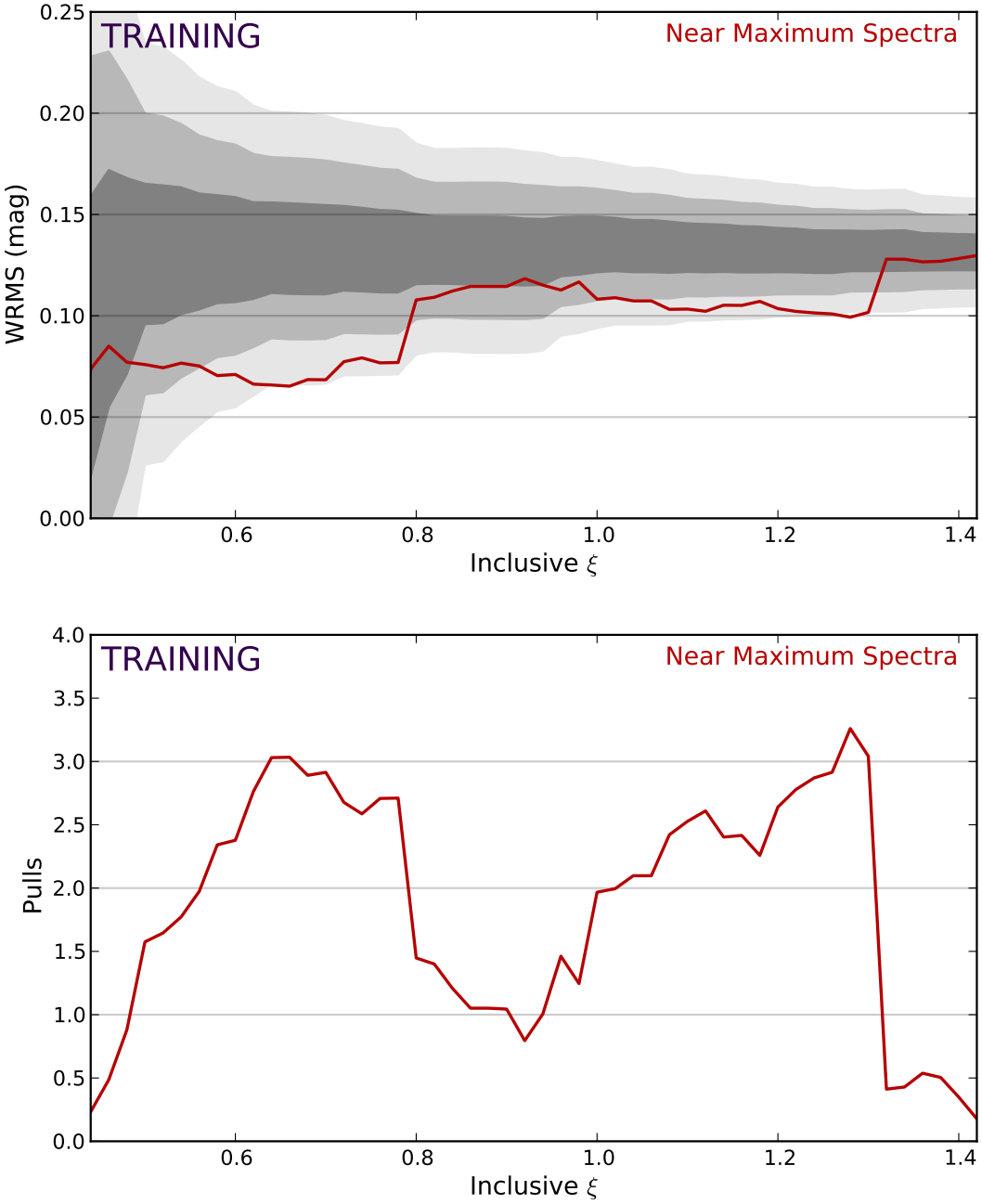

Figure 3.11 Results for the near maximum analysis on the training set data with no outlier rejection performed. Top panel shows the WRMS of the data in red along with the 1-, 2-, and 3-σ error bands from the Monte Carlo randomization tests. Bottom panel shows the pulls as a function of ξ, with a maximum significance of 3.0 σ around inclusive ξ of 0.65, with a very nice low WRMS result around 0.07 mag

Inside these boundaries, we identify curves that are below the distribution. We characterize this distribution at each bin in ξ: the lowest 10% of curves are ignored and the median

and spread of the remainder are recorded. The spread is the maximum value minus the minimum value inflated by a Gaussian correction factor (∼1.5) for dropping the lowest 10%. If a given supernova's curve has 15% of bins lower than median minus the spread/2 * 1.25 (a cautionary inflation factor), that supernova is determined to be an outlier. The cautionary inflation factor was chosen to be just large enough that the algorithm was well-behaved on the training set. With no inflation factor too many objects were detected as outliers in subsequent iterations.

The detection is done iteratively; the supernova (or supernovae) with maximum number of outlying bins above the 15% threshold is removed and the processes completed again, until no more outlying supernovae are detected. The bottom panel of Figure 3.12 shows the result of the first outlier iteration detection on the optimal weighting analysis; the outlying object is plotted in cyan. (After unblinding, this choice to iterate needed to be revisited, which will be discussed in the following chapter.)

For the optimal weighting analysis, only one outlier was found. For the analysis using only spectra near maximum light, no outliers were found. To assess the significance of the result, we must run the same jackknife procedure on the randomizations. Figures 3.13 and 3.14 show these results. The significance has dropped; for the optimal weighting analysis, it peaks around 2.2σ. If the low WRMS is confirmed with the full unblinded sample, the increase in the sample size will act to increase the significance.

To test our jackknife procedure we did a redshift perturbation for six of the supernovae to see at what stage they are detected by the jackknife procedure. For a redshift perturbation of δz, the resulting brightness difference is given by:

$$\delta M = \frac{0.00217}{z_{hel}} - \frac{0.00217}{(z_{hel} + \delta z)} \tag{3.8}$$

The outliers were detected at δz values between 0.002 and 0.009; the maximum δM was 0.0049, an error well below the dominant error source (peculiar velocity), indicating that our jackknife rejection is robust to the presence of supernovae with overall brightness calibration issues.

3.7 Additional Checks

3.7.1 Δdmfit_{corr} as Brightness Difference

There are a variety of additional checks we performed on the analysis before unblinding. One check was testing an alternative to our brightness difference proxy, κ. In its place we used residuals of the Hubble fit based on the SALT2 analysis of the light curves These residuals, which we call dmfit_{corr} are the result of using SALT2 to fit the synthesized light curves of our SNe and fitting the SALT2-determined magnitudes to the Hubble line. The "corr" subscript means that prior to the Hubble fit the magnitudes were corrected for stretch and color. The analysis proceeds identically to the above, except using Δdmfit_{corr} in place of $log_{10}\kappa$ for the brightness difference. Also, in place of the errors outlined in Equations 3.6 and 3.7, we use the errors propagated through SALT2. The results for the optimal weighting and near maximum analysis are shown in the top and bottom panels of Figure 3.15, respectively.

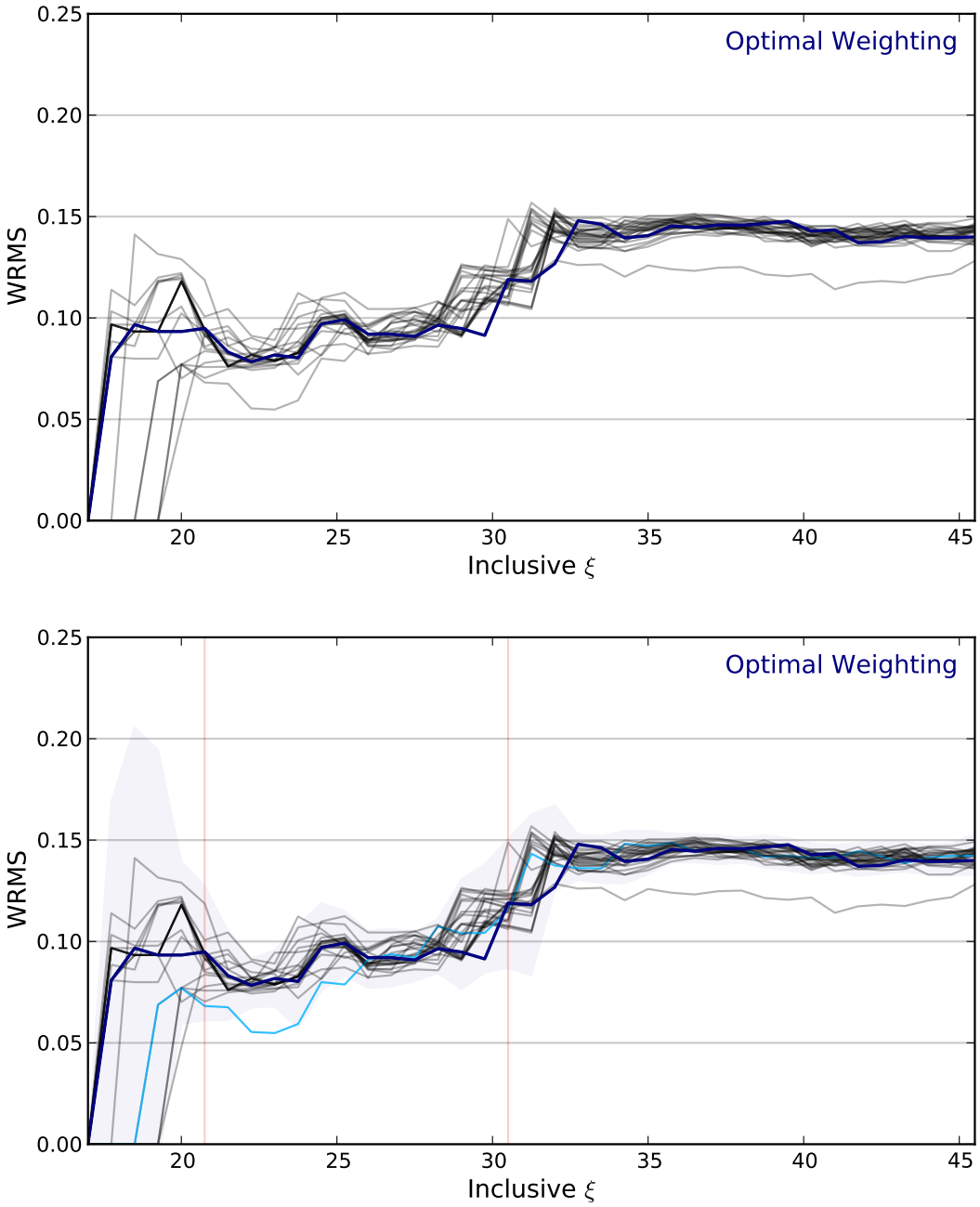

Figure 3.12 Top panel shows the jackknife distribution of WRMS curves in the optimally weighted analysis. The thick blue line is the WRMS when no SNe are excluded. The bottom panel shows the first iteration outlier detection; the thin cyan line is the supernova that was identified as an outlier; the red vertical lines mark the jackknife boundaries as discussed in the text; the grey band shows the inflated spread discussed in the text.

Jackknife outlier rejection is included. For the optimally weighted sample one outlier was found; interestingly, it is different from the outlier supernova detected using the κ as our

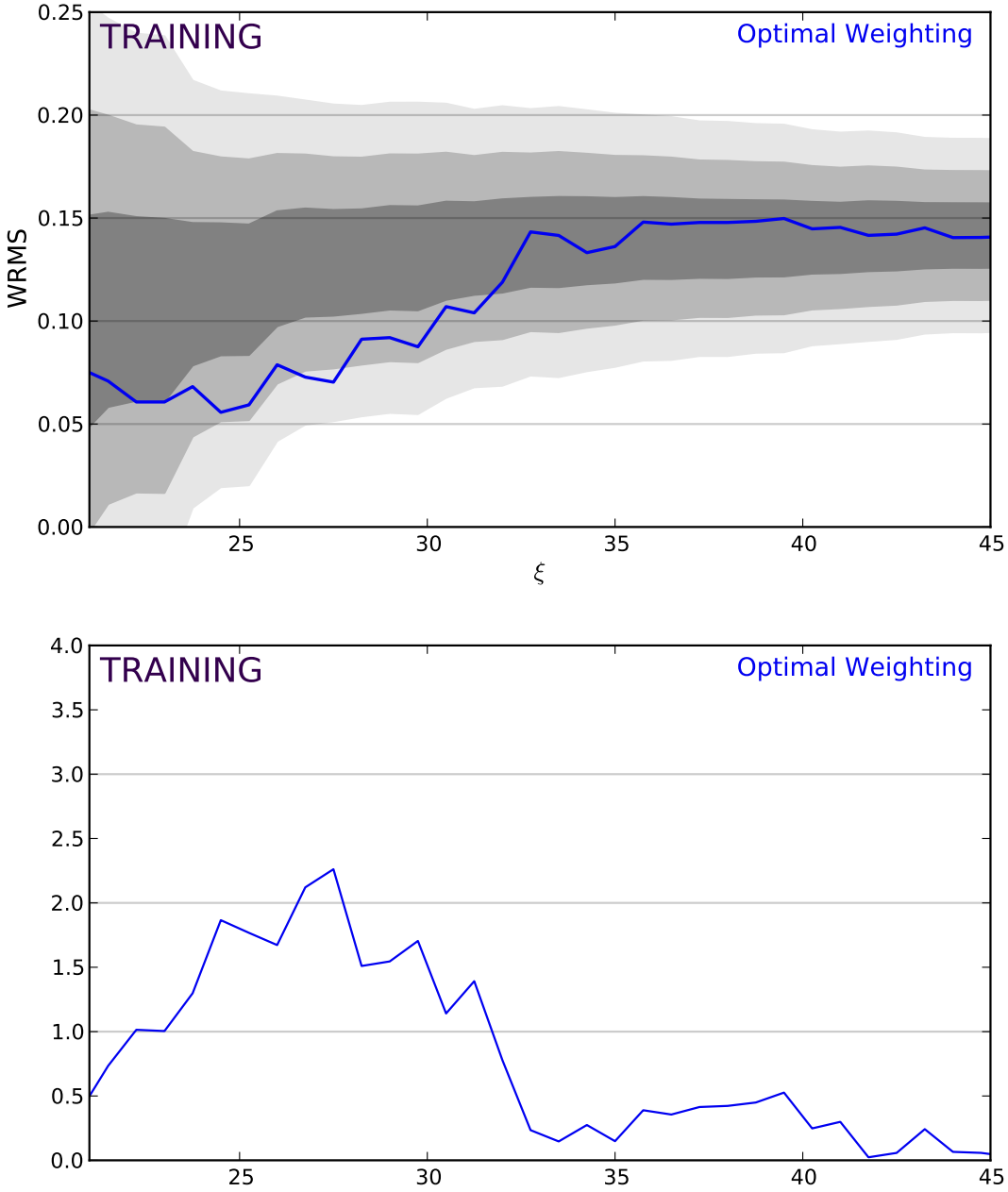

Figure 3.13 Results for the optimal weighting analysis on the training set data with jackknife outlier rejection on both the data (blue line) and randomizations (grey bands). Top panel shows the WRMS of the data in blue along with the 1-, 2-, and 3-σ error bands from the Monte Carlo randomization tests. Bottom panel shows the pulls as a function of ξ, with a maximum significance of 2.2 σ around inclusive ξ of 28, at a very nice low WRMS result of 0.07 mag.

brightness difference. For the near maximum analysis, two outliers were found, the first of

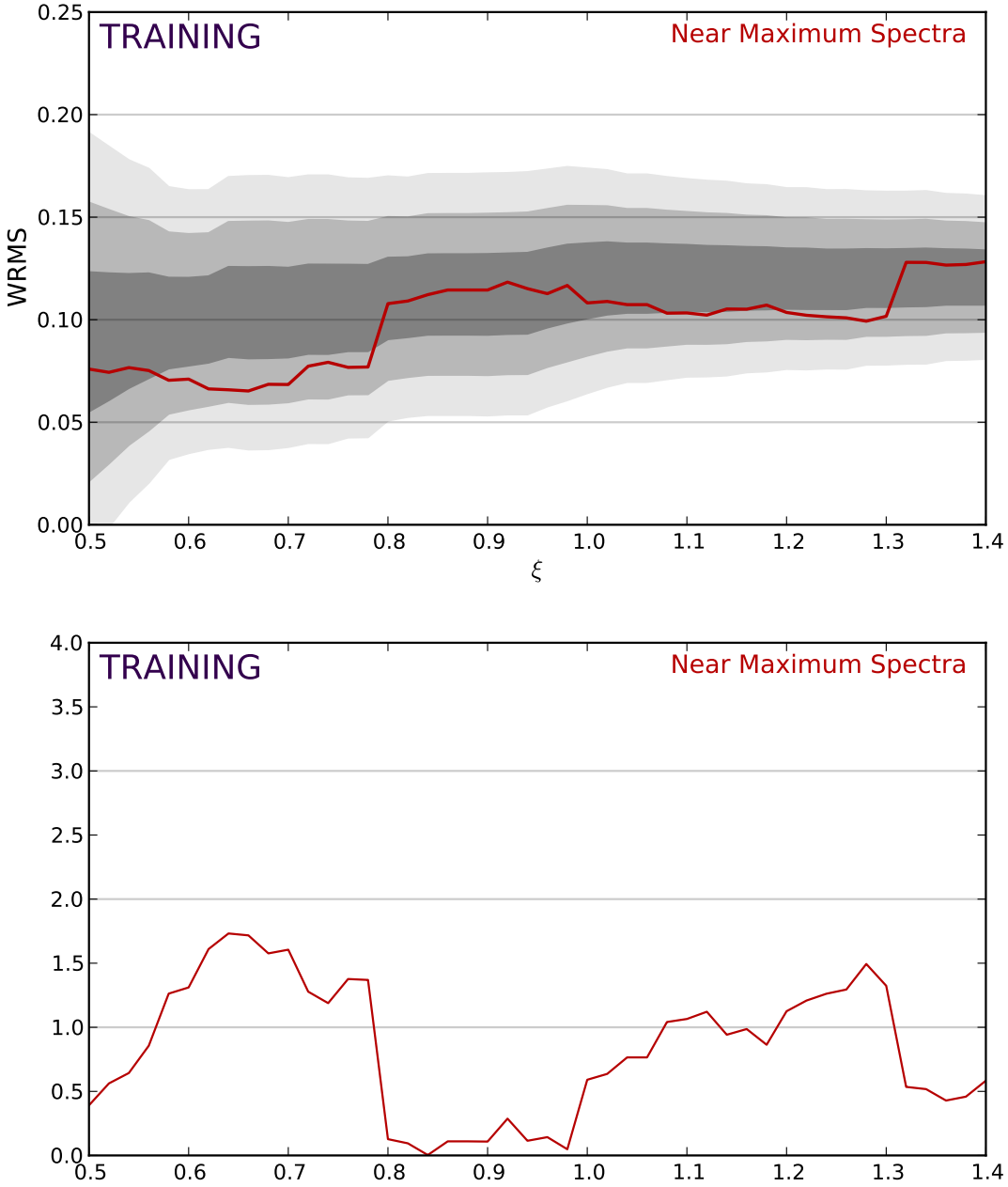

Figure 3.14 Results for the near maximum analysis on the training set data with jackknife outlier rejection on both the data (red line) and randomizations (grey bands). Top panel shows the WRMS of the data in red along with the 1-, 2-, and 3-σ error bands from the Monte Carlo randomization tests. Bottom panel shows the pulls as a function of ξ, with a maximum significance of 1.7 σ around inclusive ξ of 0.65; as no outliers were found in the data, the WRMS value remains at the nicely low value of 0.07 mag.

which was the outlier found with the optimally weighted sample, indicating, perhaps, that

there could be a problem with the SALT2 fit for this supernova.

One caveat is that we did not re-run the randomizations, the results of which are used to determine the upper limit of the jackknife outlier detection range. As we are performing here simply a check on the results using κ and not quoting a significance, we feel this is sufficient and are encouraged to examine results with the entire sample.

The goal of the test is not only to confirm the results using κ as the brightness difference proxy, but also to see if the twinness ranking is providing extra information not already contained in the state-of-the-art SALT2 analyses. The results show that this is indeed the case; the WRMS is lower for twins than for non-twins.

3.7.2 Pair Requirement

We examined changing the number of pairs required to calculate an average ΔM, results shown in Figure 3.16. In both the optimal weighting and the near maximum analyses, we see that lowering the number of required pairs to three results in a jump to larger WRMS at lower ξ value, which is consistent with expectations, as fewer required pairs will mean a less well-determined ΔM and a more easily polluted WRMS. The opposite happens when increasing the pair requirement to five: a the WRMS jump is delayed to higher ξ value. In this case, although worse twins are being included at these higher ξ values, their impact is lessened by the requirement of more pairs to calculate an average ΔM.

For the near maximum analysis, no outliers are found with the three or five pair requirement, as none were found with the four pair requirement. The same outlier is found in the optimal weighting analysis for the three, four, or five pair requirement. Thus, though the range of ξ values over which we have a low dispersion are dependent on the pair requirement, the fact that the dispersion remains low when changing the pair requirement is encouraging and we choose to continue requiring four pairs in our analysis on the entire sample.

3.7.3 Error Floor

Figure 3.17 shows the results of the analysis when the percentage error floor in Equation 3.3 is changed. Recall the 12% was chosen so that the distribution of signal to noise ratios of good twins best matched that of the overall supernova sample. No added error floor results in an over-representation of low signal to noise supernovae, as they have an intrinsic advantage in a simple χ^2.

In this test, we change the error floor in increments of 2% and run the analysis. Note that the values of κ and ΔE(B-V) remain unchanged, only the twinness metric ξ is altered. The results are plotted as a function of slice number not ξ because the value of the latter changes based on the added error floor. We did not do a full set of randomizations for each error floor nor is there any outlier rejection done. This is designed to be a simple test of the effect of the error floor.

In the bottom panel of the figure, we see that the results of the near maximum analysis are unchanged so long as the error floor is at least 8%. The upper panel shows the optimally weighted analysis; the low value of the WRMS is present to some twinness metric value for error floors above 6%. The progression of the 6% to 10% WRMS curves shows that there

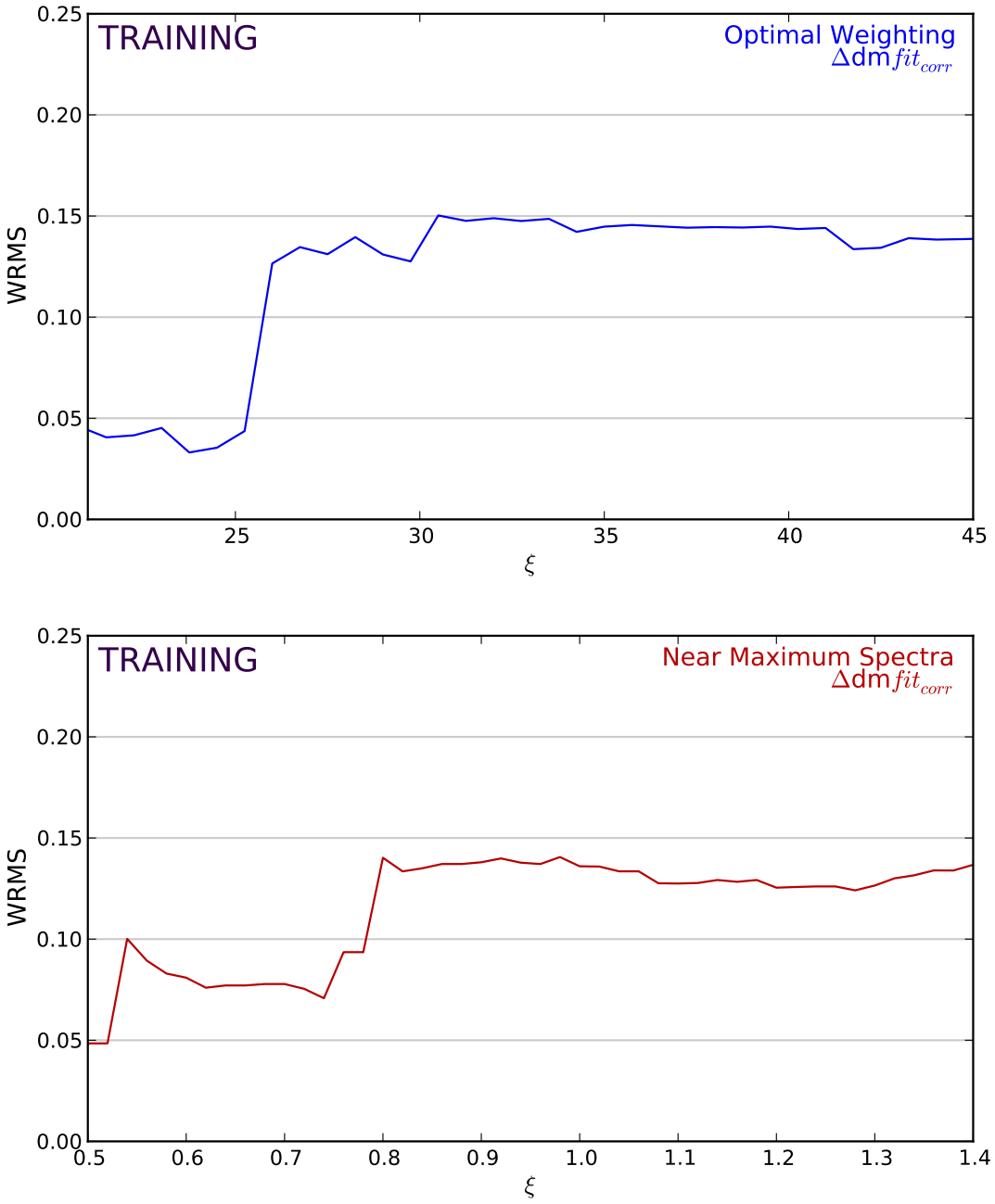

Figure 3.15 Results using SALT2 derived magnitudes as our brightness difference proxy. Top panel shows the optimal weighting analysis, bottom panel the near maximum analysis. In both cases the WRMS is low for the best pairs, indicating that the twins ranking is providing extra information not already captured in the SALT2 analysis.

is one supernova that, when included, causes the WRMS to jump; a sufficiently large error floor correctly moves this supernova to a worse twinness ranking.

By 20% the effect of increased error floor has plateaued. Indeed, there is relatively little

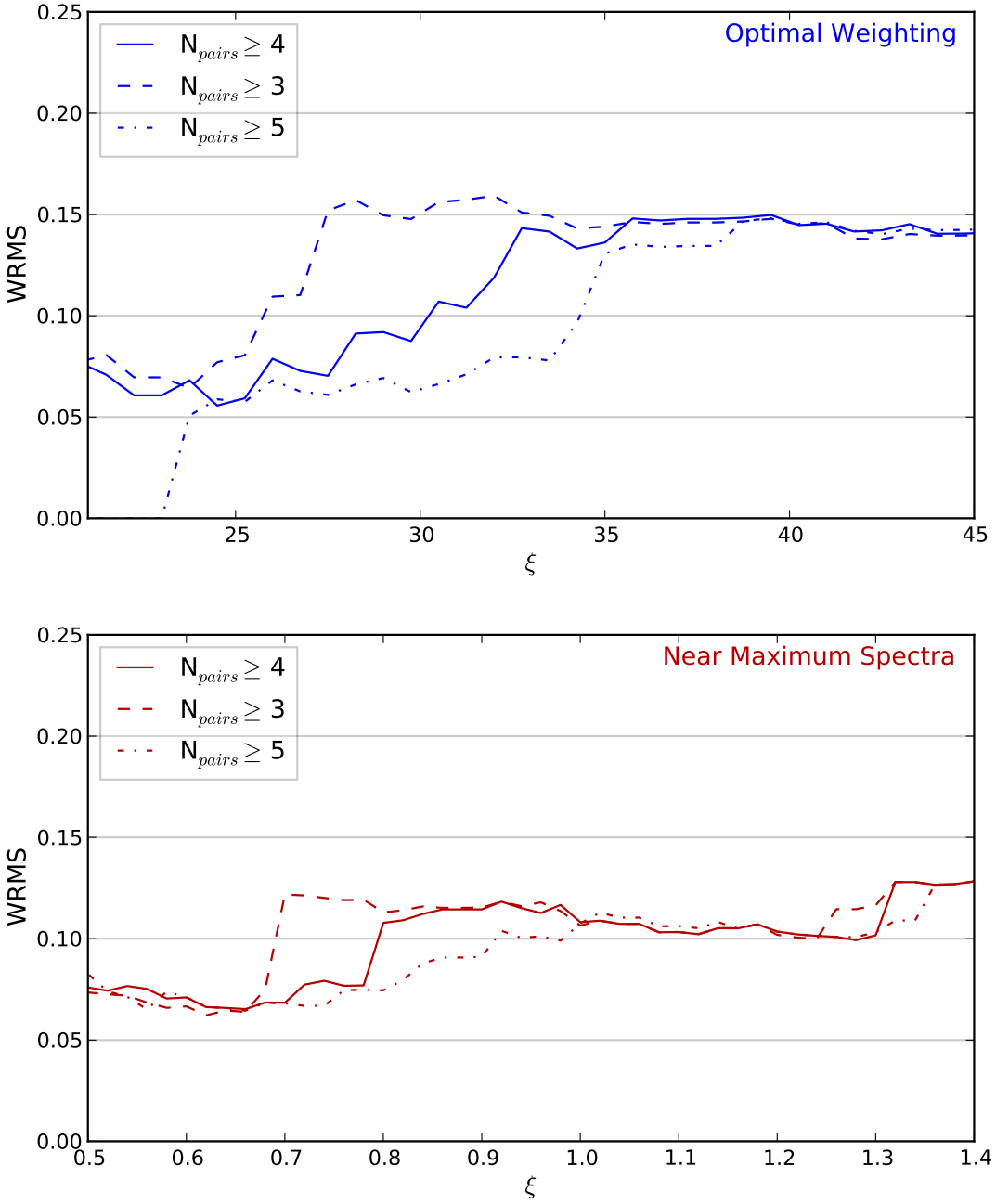

Figure 3.16 Results of the optimal weighting (top panel) and near maximum (bottom panel) analyses when altering the number of pairs required to calculate an average ΔM. In both cases the WRMS is low despite changing the pair number, though the ξ value at which the WRMS increases is variable.

change in the WRMS for error floors above 12%, which indicates that it is a sufficiently good choice for the full analysis on the entire sample.

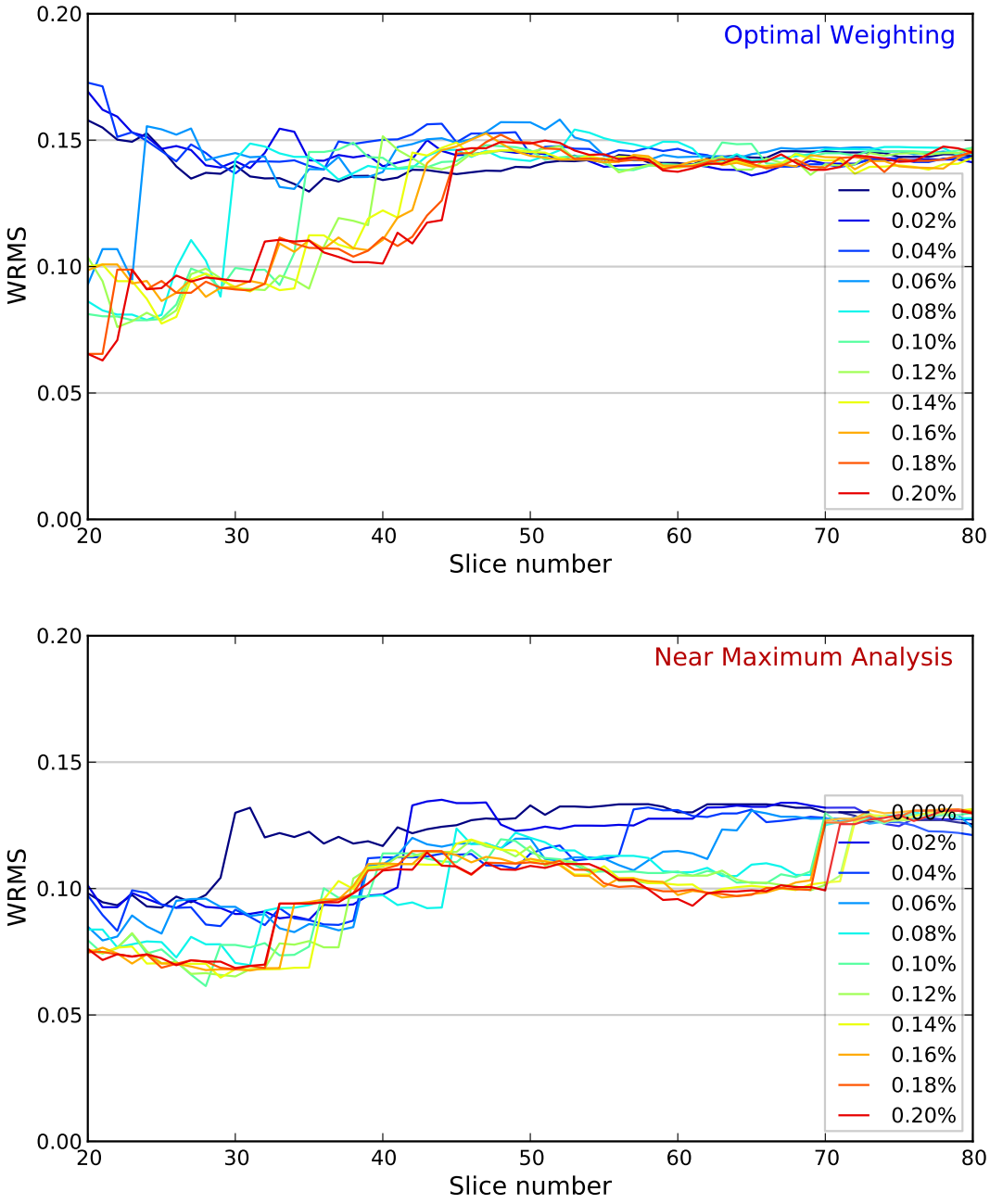

Figure 3.17 Results of optimally weighted (top panel) and near maximum (bottom panel) analyses when changing the percentage error floor added into Equation 3.3. The low WRMS result is present to at least some ξ with error floors above 6%. There is little changed by increasing the error floor beyond the 12% used in the analysis.

3.7.4 R_V Value

There is some controversy in the supernova cosmology field over the proper value to use for reddening correction. Our choice of R_V=3.1 reflects the Galactic value for dust, though some

prefer a smaller value, for a more shallow color correction. There is evidence (presented in Chotard et al. [2011]) that when accounting for supernova features, the appropriate reddening law is substantially closer to the Galactic value for dust.

Our underlying assumption is that any color difference in true twins must be caused by external factors, such as dust extinction, which is why we choose to use a Cardelli color law [Cardelli et al., 1989] with R_V=3.1. Nevertheless, we test the effects of changing R_V, with results shown in Figure 3.18. The fiducial analysis with R_V=3.1 is shown by the thick black line; the colored lines show the result for differing R_V values.

For each curve, jackknife outlier rejection has been done as outlined in previous sections, except that the upper and lower boundaries were fixed to the non-shaded region shown in the figure. For both the optimal weighting and near maximum analyses the value of R_V has a non-negligible impact on the final result. Interestingly, the "best" R_V (i.e. those corresponding to the low WRMS) are different when considering the whole timeseries (optimal weighting) versus only the spectra at maximum light. It should be noted that fitting for the value of R_V in Equation 3.1 is not an option, as the value of R_V governs the a_λ component of the Cardelli law (which is fairly monochromatic) and as such is degenerate with the fit for κ.

Given that the R_V=3.1 curve is generally in the middle of the distribution and that it is the value with the best physical argument, we choose to continue using this value for R_V for the full analysis on the entire sample.

3.7.5 Low Redshift Supernovae

Some early by-eye identification of outliers pointed to pairs involving low-redshift (z<0.03) supernovae having large values of ΔM. Although we include the peculiar velocity error in our uncertainty on ΔM, this may not be sufficient to de-weight these objects. Additionally, if there were only a few of them, the jackknife outlier rejection might be able to throw them out. However, with eight of the 37 training set supernovae having a redshift below 0.03, it would not be possible to identify them with a single jackknife procedure.

Thus since our analysis is focused on purity over inclusion, we threw out these objects and proceeded with the analysis. Here, for thoroughness, we test their impact on the final results, using the same procedure as outlined above.

Without allowing jackknife outlier rejection on either the data or the randomizations, the optimal weighting analysis gives a WRMS of 0.11 mag at a significance of 2σ. For the near maximum analysis, the result is somewhat better: WRMS of 0.09 mag at a significance of 2.5σ.

With the jackknife outlier rejection in place, one outlier is found for the optimal weighting analysis, dropping its best WRMS to 0.09 mag. No outliers are found for the near maximum analysis. However, the significance will drop strongly in both cases when outlier rejection is allowed on the randomizations.

Given the higher value of the WRMS and lower significance when including the low-redshift supernovae, we continue to remove them from the sample in the full set analysis.

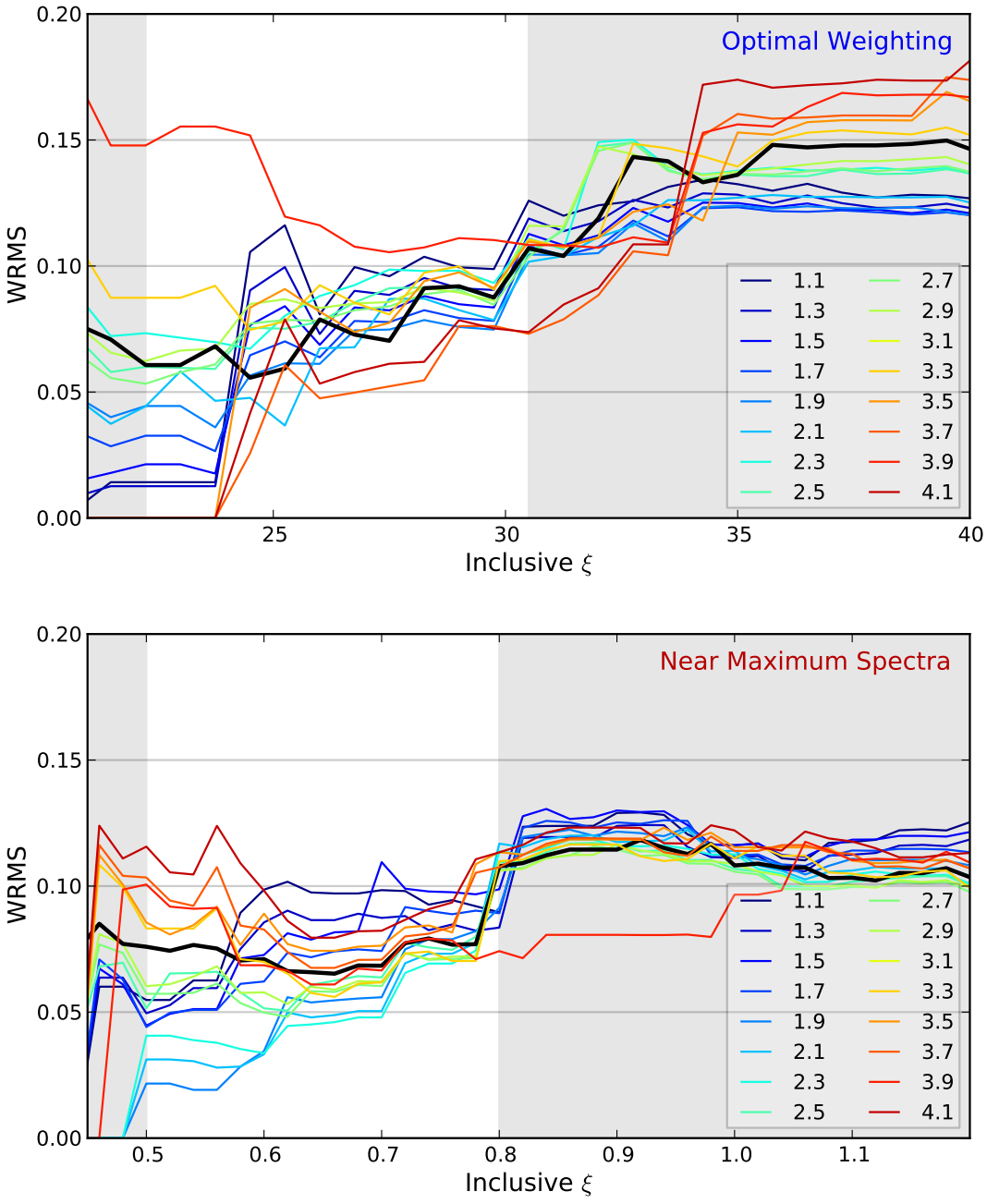

Figure 3.18 Top panel shows results on the optimally weighted analysis when the value of R_V is changed in the fit for κ and ΔE(B-V) in Equation 3.1. Bottom panel shows the same for the near maximum analysis. In both cases, jackknife outlier rejection has been done for each value of R_V, with the upper and lower boundaries fixed and illustrated by the non-shaded region. The primary analysis (using R_V=3.1 is shown by the thick black line.

Chapter 4

Unblinded Twins Results

4.1 Unblinding Checks

Having finalized the analysis on the training set half of the sample, we begin the unblinding in stages, to check for any possible issues before examining the final result. The first sanity check is to visually inspect the pairs ranked by ξ and see if, by eye, the overall trend is that pairs with lower ξ value have similar spectra and pairs with higher ξ values have disparate spectra. As expected, this first sanity check is confirmed.

4.1.1 Optimal Weighting with the Full Sample

Additionally, since we have more data in play we must test how the optimal weighting differs. Figure 4.1 shows the updated sliced analysis, completed identically to that done above but now using all of the data, not just the training set. The overall results look very similar. Note that the spread in the dispersion (WRMS) is blinded; this way we have not given away the end result but we can get a sense of how well the fit performs.

We can compare the slope of this fit with the slope of the linear fit for the training set only: here we have a somewhat steeper value of -4, compared to the training value of -3, indicating that with the full sample even more weight is placed in early phases. Given the over all similarity of the results here and in the training set analysis, we choose to use this new linear fit as our optimal weighting.

4.1.2 Outlier Rejection

We also tested our outlier rejection with the full sample, again with the spread in the dispersion (WRMS) blinded. First we checked boundary stability, particularly whether or not to fix the jackknife boundary values to those found with the training set or to let them float and be chosen at each iteration as they were in the training analysis. After examination, we chose the latter, as the tests on the maximum light analysis showed no differences in the end result with different boundary selections. Note that we cannot test this directly with the optimally weighted analysis because using a new optimal weighting scheme changes the ξ values.

We did not alter the cut selections but let the jackknife outlier rejection proceed as with the training set. Recall that the jackknife boundaries are determined using the maximum significance from the Monte Carlo randomization tests. In this stage of the unblinding, we do not examine either the WRMS curve with no outlier rejection or the significance with respect to the randomizations. We examine those in the following section.

Figures 4.2 and 4.3 show the iterations of the jackknife outlier rejection. The top panel of Figure 4.2 shows the identified outlier in cyan; the bottom panel shows the second outlier. The top and bottom panels of Figure 4.3 show the third and fourth outliers, respectively.

Although the scale of the WRMS is blinded, we can assess to what degree the outliers that are found are consistent with what we desire our algorithm to find. Upon visual inspection, the first outlier seems quite reasonable, although the subsequent ones are perhaps less clear. In order to be sufficiently conservative, we will present results tightening our constraints such that only the first outlier is rejected.

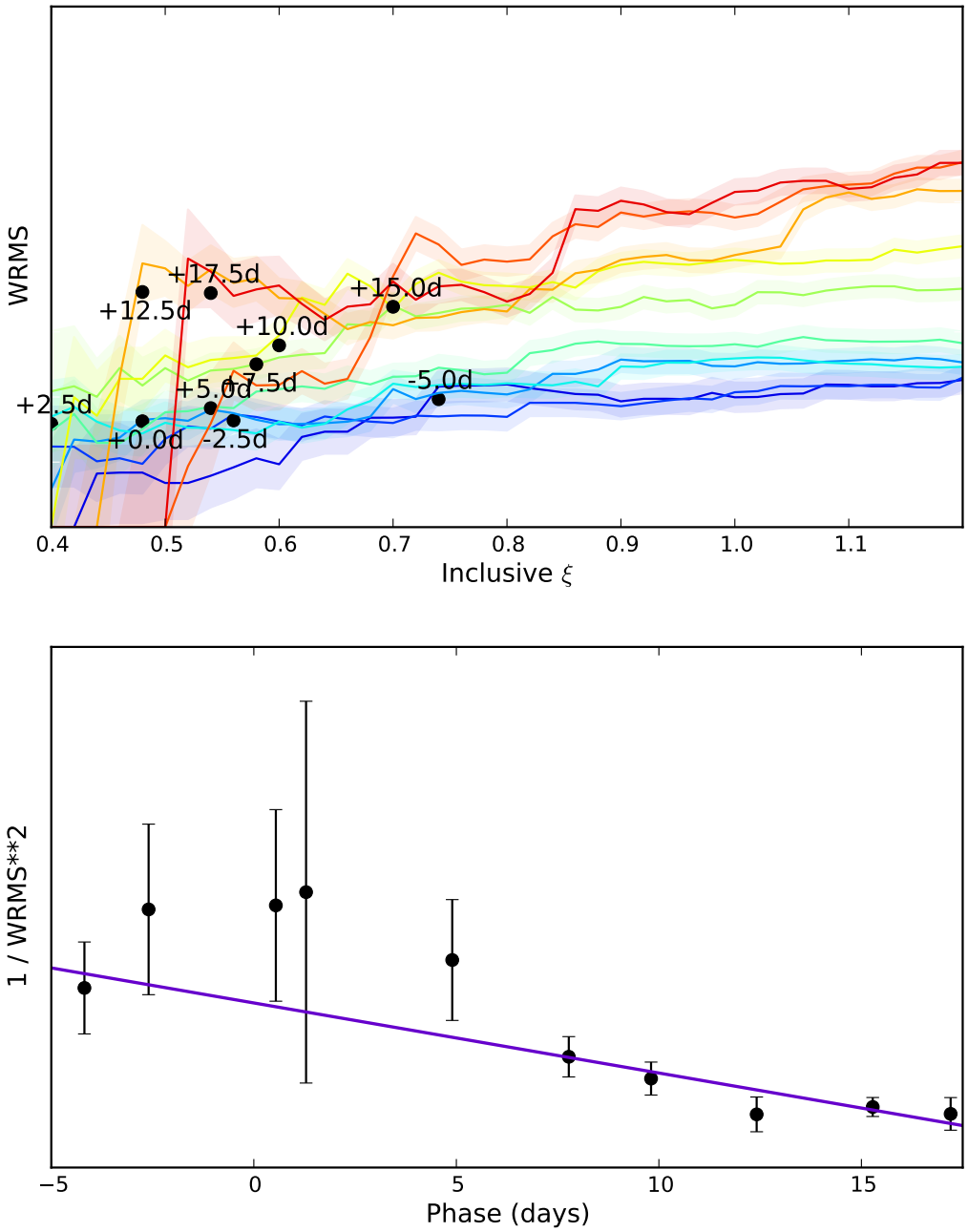

Figure 4.1 As Figure 3.9 but with the full sample. Top panel: WRMS as a function of inclusive ξ for different phase bins, The shaded regions are the error on the WRMS values. Each line is labeled by the bin-center value. The black circles show the WRMS values that were used in the lower panel to calculate the optimal weighting function. Lower panel: The purple line is a weighted linear fit to the inverse variance, where the points are drawn from the upper panel.

The near maximum analysis behaves similarly. Five outliers are found, but the first is

more convincing to the eye than the subsequent ones. Thus to guard against too zealous an outlier rejection we allow only one supernova to be rejected.

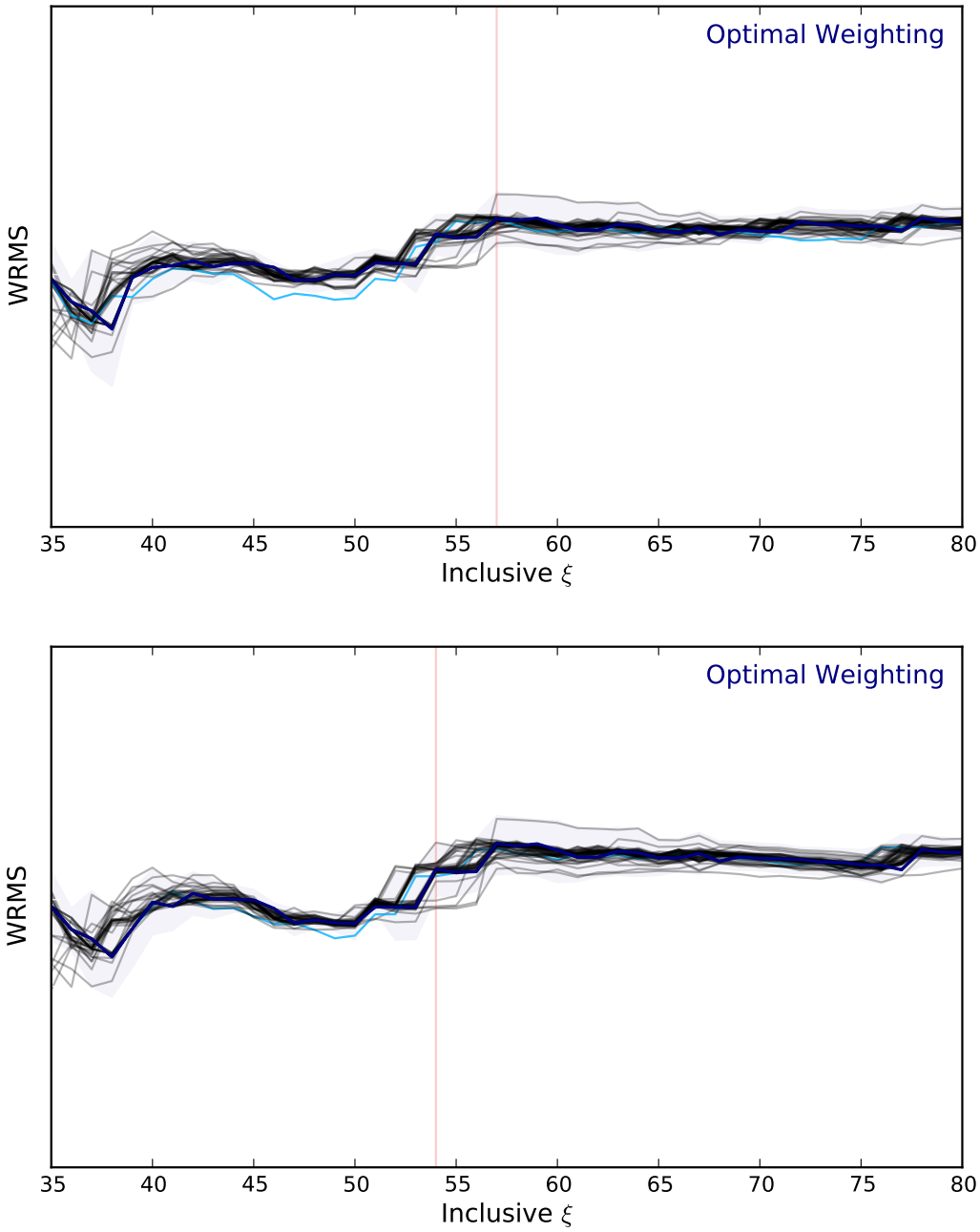

Figure 4.2 Blinded jackknife outlier rejection figures. Top (bottom) panel shows the first (second) iteration. The thin black lines show the WRMS when each supernova is removed in turn from the sample. The thick blue line shows the WRMS when all supernovae are used. The thin cyan line illustrates the outlier. The thin vertical red line shows the boundary cut off, determined from the randomizations.

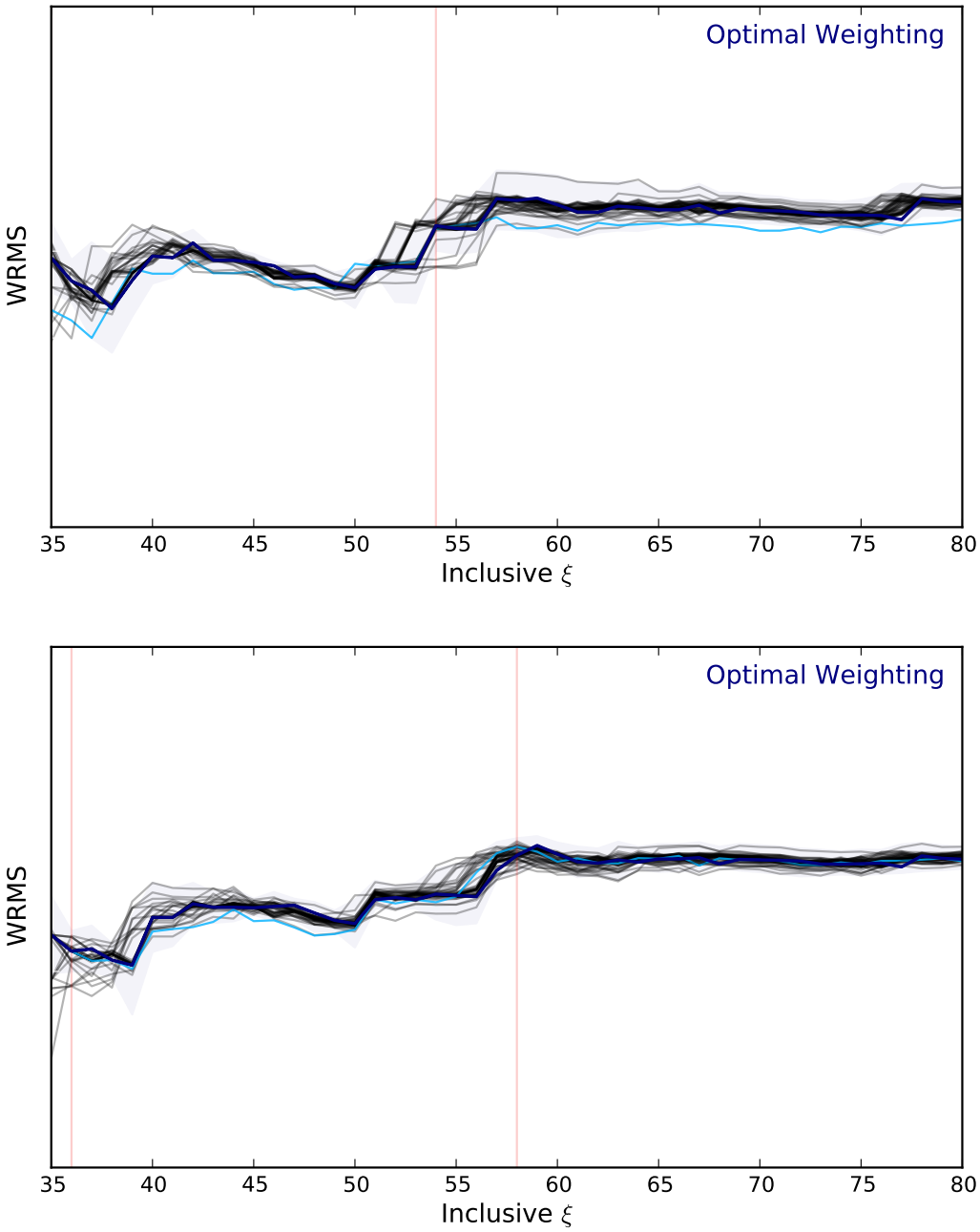

Figure 4.3 Blinded jackknife outlier rejection figures. Top (bottom) panel shows the third (fourth) iteration. The thin black lines show the WRMS when each supernova is removed in turn from the sample. The thick blue line shows the WRMS when all supernovae are used. The thin cyan line illustrates the outlier. The thin vertical red line shows the boundary cut off, determined from the randomizations.

4.2 Full Sample Results

With our checks completed we are prepared to unblind the WRMS values using the full sample. We unblind in two steps: first the result with no outlier rejection performed either

on the data or on the randomizations; second the result with a single outlier rejection allowed both on the data and the randomizations.

4.2.1 No Outlier Rejection

Figures 4.4 and 4.5 show that although the value of the spread in the dispersion (WRMS) is somewhat higher with the full sample, around 0.1 mag, for the optimal weighting versus around 0.09 mag with just the training set, the significance of the result is substantially higher, around 3.5 σ, increased from 2.8 σ. The results are similar for the near maximum analysis: the WRMS is somewhat higher (0.09 mag for the full sample vs 0.07 mag for the training sample) but at higher significance (4.5 σ vs 3.0 σ).

Recall that in the WRMS calculation we require at least four pairs to calculate an average brightness difference. Since that number is finite, our WRMS calculation suffers from a penalty that goes as $\sqrt{1+1/N}$ where N is the number of pairs used. Using the average number of pairings at each ξ value, we are able to correct the quoted WRMS by the appropriate value, which we call WRMS_{corr}; it is what the dispersion would be for an equivalent large sample. Table 4.1 lists both the WRMS and WRMS_{corr} for the full sample analysis. (Note that the quoted errors are obtained from simple error propagation.)

Table 4.1 Full sample WRMS results

		No Outlier Rejection	**Single Outlier Rejection**
Optimal Weighting	WRMS	0.099 ± 0.011 mag	0.086 ± 0.011 mag
	WRMS_{corr}	0.093 ± 0.010 mag	0.081 ± 0.010 mag
	WRMS_{pop}	0.085 ± 0.009 mag	0.071 ± 0.009 mag
At Max Spectra	WRMS	0.090 ± 0.010 mag	0.083 ± 0.011 mag
	WRMS_{corr}	0.086 ± 0.010 mag	0.078 ± 0.010 mag
	WRMS_{pop}	0.075 ± 0.008 mag	0.067 ± 0.009 mag

4.2.2 Single Outlier Rejection

Figure 4.6 shows that allowing one outlier to be rejected drops the spread in the dispersion (WRMS) to 0.086 mag for the optimal weighting analysis but maintains a good significance around 3.3 σ. Similarly, Figure 4.7 shows that a low WRMS of 0.083 mag at 3.6 σ is found for the near maximum analysis.

It is interesting that the near maximum analysis performs as well as the optimally weighted analysis (or even somewhat better in the case of no outlier rejection), as we may expect the latter to benefit from the additional data. However, it is plausible that the bulk of the brightness-dispersion relevant information is present in the spectra near maximum light. In that case, adding in data at different phases will alter the twinning metric without adding any brightness-dispersion predictive power. The fact that the near maximum analysis performs so well is encouraging for future high-redshift supernova surveys; if only one spectrophotometric observation were to be needed to achieve a dispersion of $\sim$0.085 mag, it would represent a big improvement in standardization.

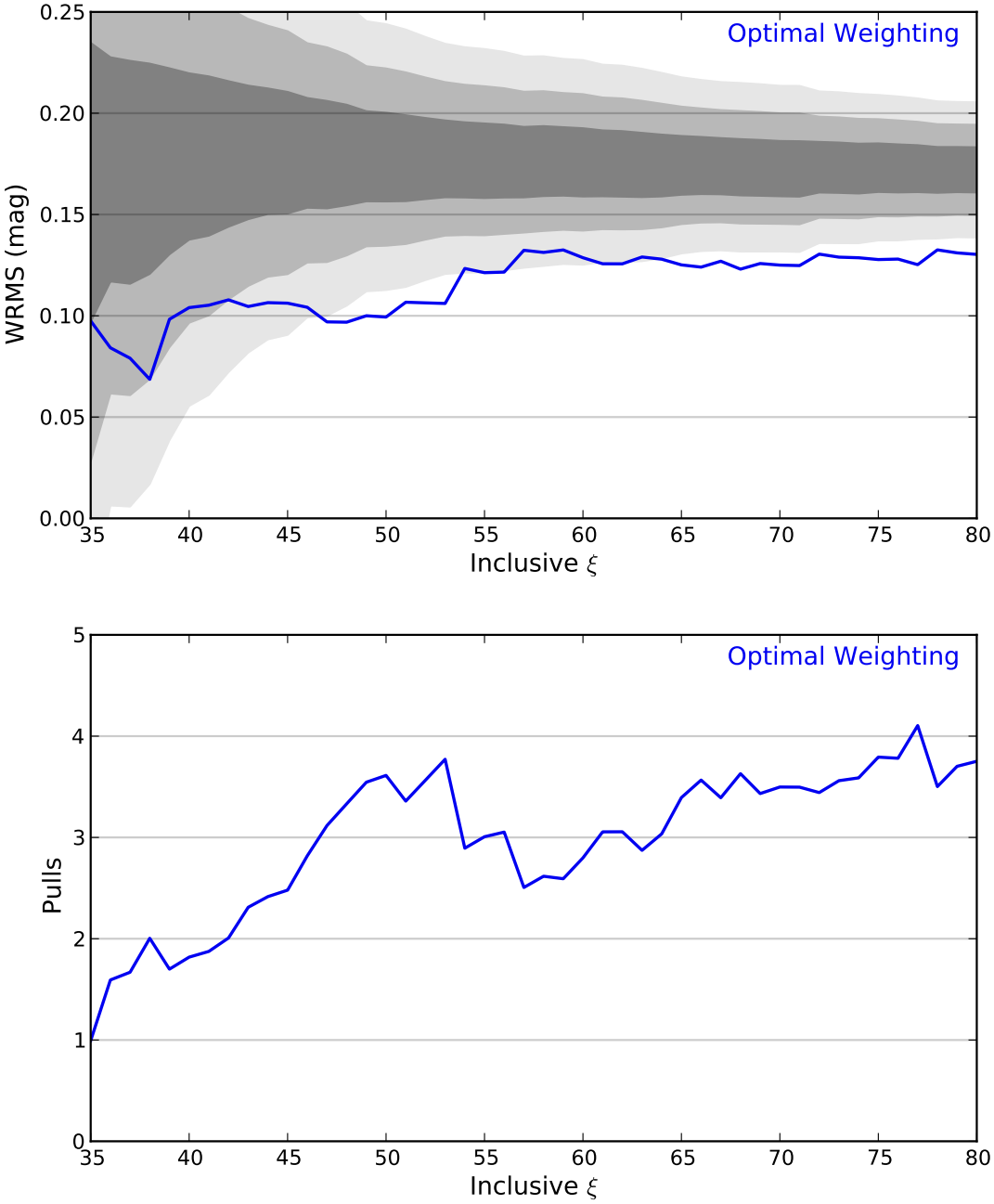

Figure 4.4 Results for the optimal weighting analysis on the full data set with no outlier rejection. Top panel shows the WRMS of the data in blue along with the 1-, 2-, and 3-σ error bands from the Monte Carlo randomization tests. Bottom panel shows the pulls (the magnitude dispersion in units of sigma) as a function of ξ, with a maximum significance of 3.8 σ around inclusive ξ of 50, with a WRMS result of 0.10 mag.

We also examined the results that we would get if we allowed additional outlier rejection in straight analogy to what we did with the training sample. Doing this finds four outliers

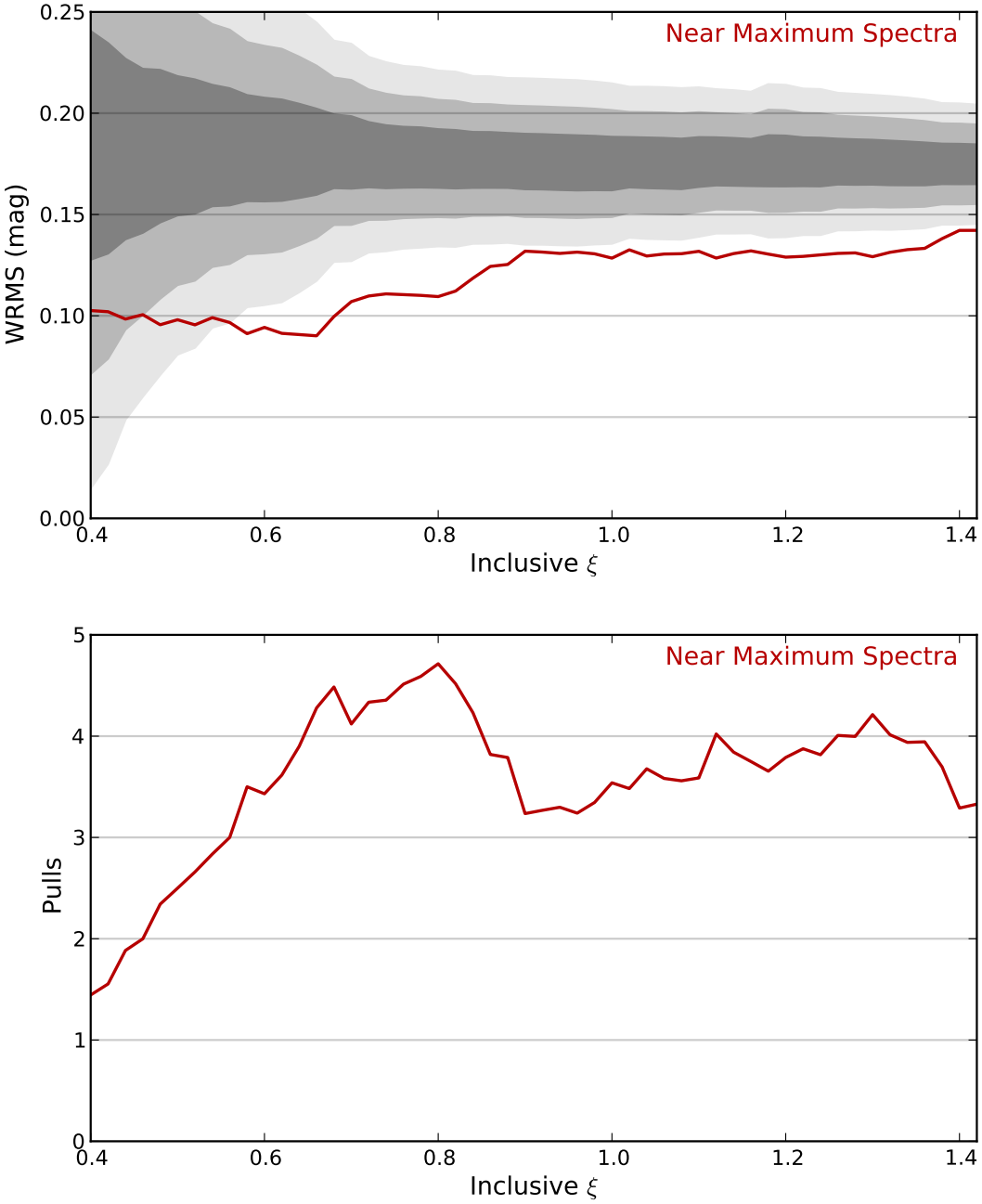

Figure 4.5 Results for the near maximum analysis on the full data set with no outlier rejection. Top panel shows the WRMS of the data in red along with the 1-, 2-, and 3-σ error bands from the Monte Carlo randomization tests. Bottom panel shows the pulls (the magnitude dispersion in units of sigma) as a function of ξ, with a maximum significance of 4.5 σ around inclusive ξ of 0.7, with a WRMS result of 0.09 mag.

and does drop the WRMS for the data to about the 0.07 mag level, but it also drops the significance of the result to around 2 σ. This was surprising, as we expected the significance

to increase with respect to what it was on the training sample given the additional data. The fact that it did not tells us that the iterative outlier rejection is being overly aggressive and perhaps does not behave in the same way on randomizations as it does on the real data.

4.3 Discussion

Table 4.1 shows that we have a better standard candle than previously available. The dispersion has a variety of contributing elements, one of which is the velocity dispersion. At the low redshifts of our sample, the velocity dispersion represents a substantial portion of our error budget. It is instructive to consider the value of the dispersion when this component has been removed. Although the precise value to subtract is dependent on the fine details of which supernovae are involved at how many pairs at each ξ value, our redshift distribution is reasonably smooth and a first order sense of the effect can be achieved by simply subtracting in quadrature the error floor of the dispersion arising from peculiar velocities alone. These numbers are quoted as WRMS_{pop} in Table 4.1.

Although these numbers do not represent the spread in the sample (as the uncertainty in the peculiar velocity is a valid source of error that must be included), they represent the upper limit on the potential of population drift in an analysis such as this. Population drift, the systematic impact of different subpopulations appearing in different proportions at different redshifts, has been worried about at the 0.1 mag level. But the twins analysis shows that with careful matching it is possible to keep it at or below the 0.07 mag level. This is actually still an upper limit because there are still other sources of error.

The twins analysis sets the bar for what the goals should be for future observations and analysis tools.

For cosmological utility, we would hope that a newly discovered high-redshift supernova would have sufficient pairs in the low-redshift sample such that its magnitude could be calculated. We have 36 supernovae with sufficient pairs by the ξ cut off to be included in the weighted RMS calculation. Although we had 60 supernovae in the full sample, a look at the number of all potential pairs for each supernova revealed that five of them lack sufficient late time coverage to be adequately compared to the other 55. Additionally, three of the supernovae are beyond our normal redshift cut-off; they were followed because they were potential super-Chandrasekhar-mass candidates, but their signal to noise is much lower than the target sample, and these should also be neglected from the accounting. This leaves an overall success rate of 36 out of 52, 69%, but depends on the signal to noise of the data set.

Of the 16 supernovae lacking sufficient pairings, five have peculiar spectral features, some belonging to specific subtypes. Given that peculiar supernovae are rarely occurring, only with a larger nearby sample could a given high-redshift supernova of this subtype be included. The remaining 11 are preferentially at higher redshift and lower signal to noise than the bulk of the sample. Indeed, if we only examine the half of the sample with higher signal to noise, we find that only three of the otherwise unaccounted for supernovae have insufficient pairs, a success rate of 88% for the higher signal to noise half of the data.

One next step is to complete this analysis on data from the final reduction pipeline. These low dispersion results may improve with the final reductions in place; that the removal of a

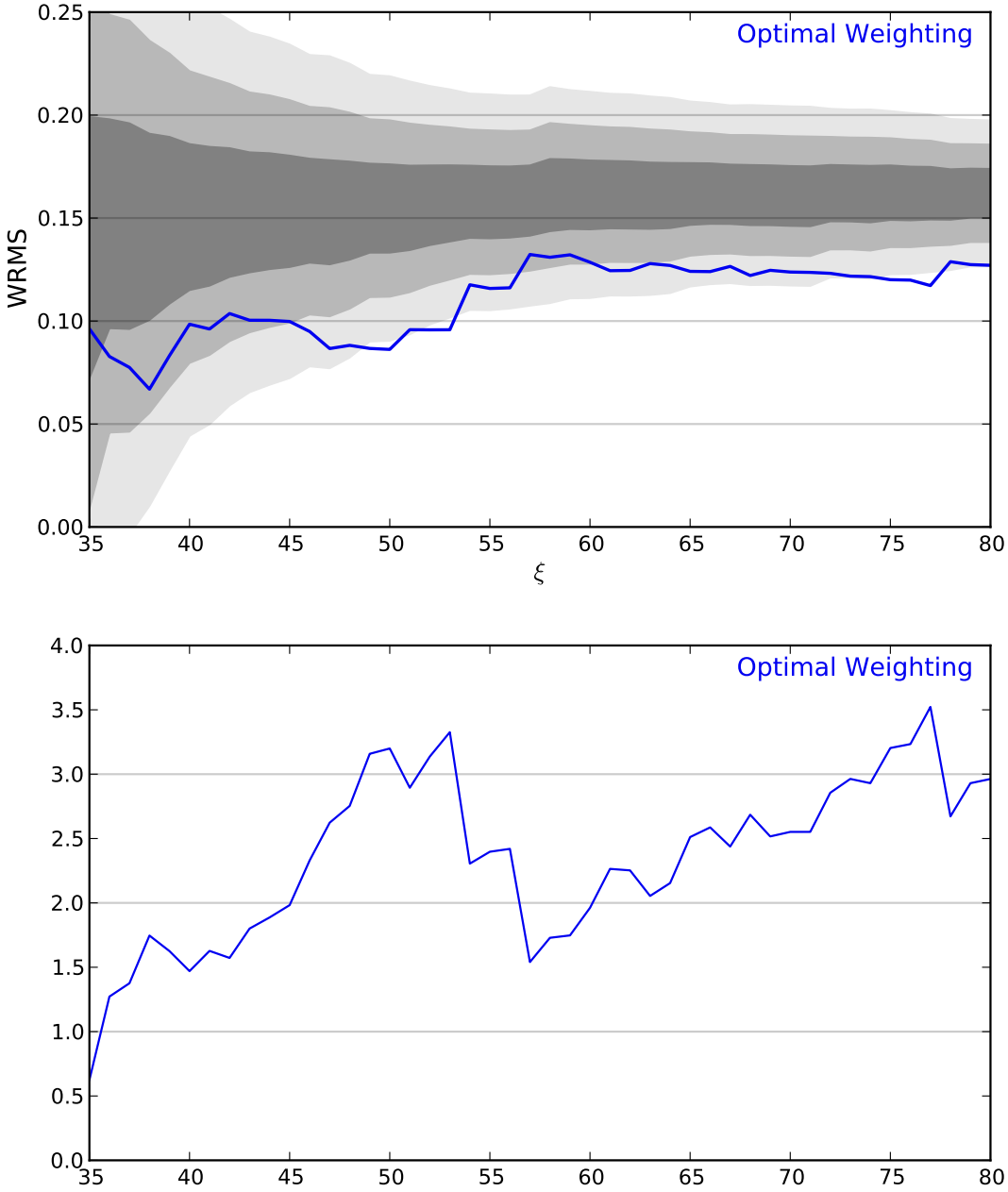

Figure 4.6 Results for the optimal weighting analysis on the full data set with one iteration of jackknife outlier rejection on both the data (blue line) and randomizations (grey bands). Top panel shows the WRMS of the data in blue along with the 1-, 2-, and 3-σ error bands from the Monte Carlo randomization tests. Bottom panel shows the pulls (the magnitude dispersion in units of sigma) as a function of ξ, with a maximum significance of 3.3 σ around inclusive ξ of 50, with a nice low WRMS result of 0.086 mag.

single outlier significantly improves the result suggests that if even a few of the supernova

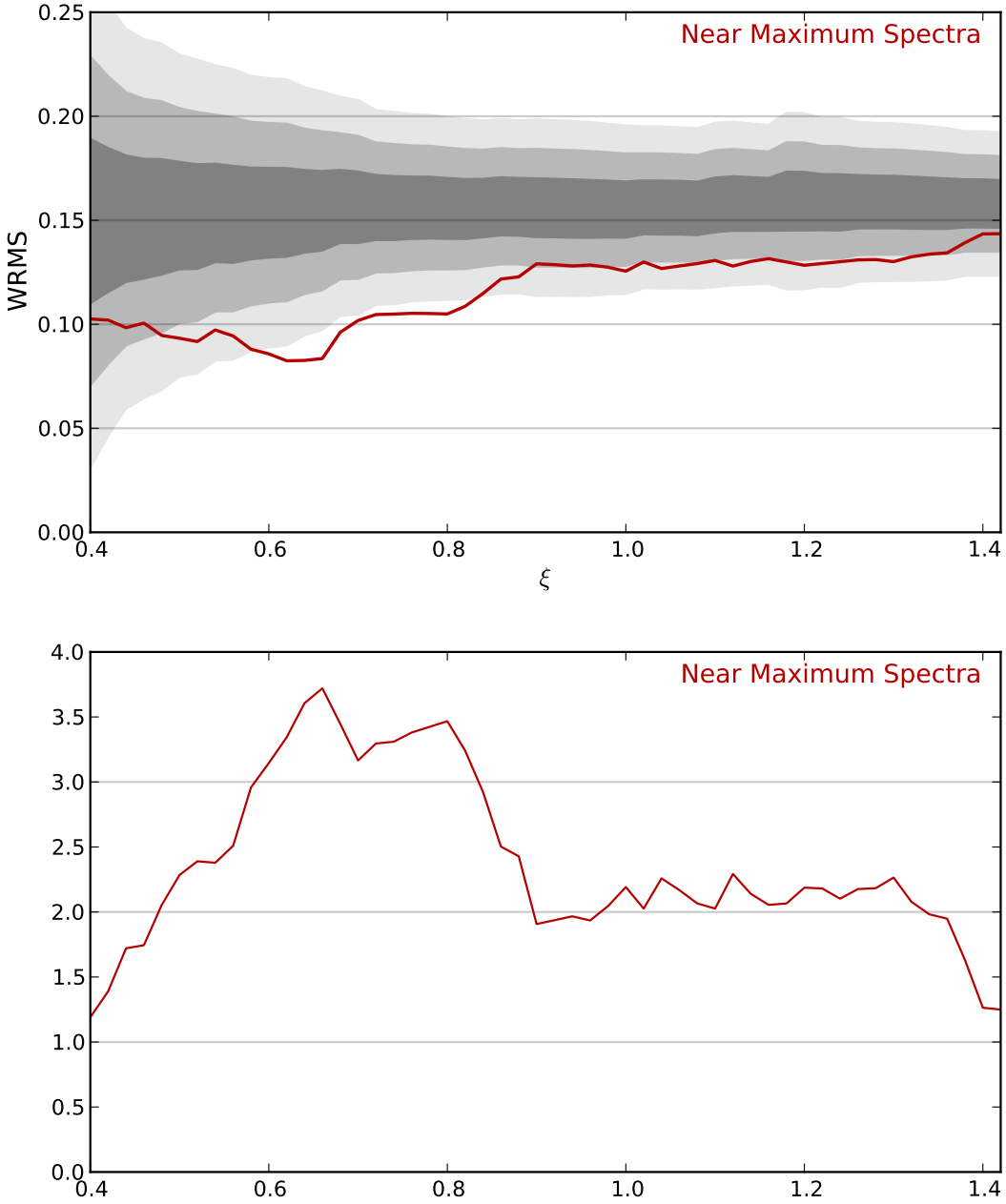

Figure 4.7 Results for the near maximum analysis on the full data set with one iteration of jackknife outlier rejection on both the data (red line) and randomizations (grey bands). Top panel shows the WRMS of the data in red along with the 1-, 2-, and 3-σ error bands from the Monte Carlo randomization tests. Bottom panel shows the pulls (the magnitude dispersion in units of sigma) as a function of ξ, with a maximum significance of 3.6 σ around inclusive ξ of 0.65, with a nice low WRMS result of 0.083 mag.

calibrations are still not perfect, there could be a still better twin result when they are

revisited.

Further restrictions of the twins analysis to smaller phase ranges and less stringent quality cuts are the obvious next step of the analysis, in order to assess just how good the data of high-redshift supernovae would need to be to maintain the ∼0.085 mag dispersion level.

4.4 Extension to High-Redshift

As discussed above, there are many exciting extensions of the twins analysis testing just how much and what quality of data is needed to maintain such a low dispersion. A first simple question is whether we can obtain anything close to the twins result with a standard high-redshift sample.

To test this, we degrade the size (i.e. number and phase distribution) and quality (i.e. signal to noise) of the Nearby Supernova Factory sample to match that found in the Supernova Legacy Survey (SNLS) spectroscopic data presented in Appendix B. The SNLS data were taken at the W .M. Keck 10m telescope as part of the five-year supernova typing program and are generally representative of the quality of high-redshift spectroscopic data.

There are two primary ways in which a degraded Nearby Supernova Factory sample is still superior to the Keck high-redshift data, namely the host subtraction and the spectrophotometricity. Host subtraction with slit spectroscopy is notoriously difficult, though progress has been made in recent years [Baumont et al., 2008]. The Keck data certainly suffer from contamination by host light and though reasonable host templates can be subtracted to aid in typing and phase determination, they are not sufficient for detailed spectral analyses such as the twins analysis. The lack of spectrophotometricity is also a constraint on the utility of high-redshift observations, as without assurance that the observations have captured all of the light (which is not possible with slit spectroscopy) the underpinnings of the twins analysis are lost. Thus this test represents a sort of best case scenario of high redshift data; if it is not possible to recover a low dispersion result even in this ideal case, it is highly informative as to what manner of data will be needed in the future.

To perform this test, each SNLS supernova in the sample is replaced with a Gaussian Process prediction of a randomly chosen Nearby Supernova Factory supernova that has coverage near the phase of the SNLS observation. Gaussian noise is added to the replacement spectrum until the median signal to noise matches that of the SNLS observation.

From this point the analysis proceeds as outlined above. A χ^2 minimization is done to fit for the scale factor κ and color difference $\Delta E(B-V)$. The pairs are ranked based on their twinness metric value ξ and the WRMS is calculated as described in Chapter 3. Figure 4.8 shows the WRMS results. We see that the twins ranking does improve the WRMS vs no ranking at all. However, with this quality of data a dispersion of 0.15 mag is all that can be achieved, similar to what is obtainable with photometric standardization methods. For the full power of the twins analysis to apply to future high redshift surveys, the data quality would need to improve. Further study is warranted on just how much the Nearby Supernova Factory can be degraded (both in quality and quantity) and still achieve a WRMS of ∼0.085 mag.

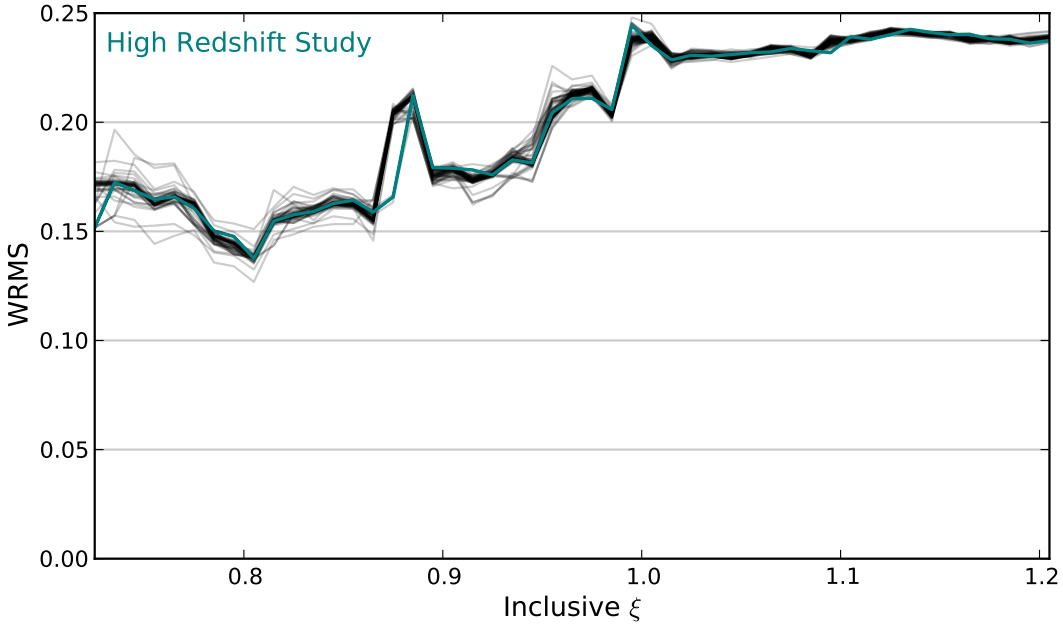

Figure 4.8 Magnitude dispersion in mock high redshift study. Using the twins ranking does improve the WRMS, but only to about 0.15 mag, indicating that to use the full power of the twins analysis future high redshift studies would benefit from higher quality spectrophotometric data.

Part II

Additional Spectrocopic Analyses

Chapter 5

Literature Analysis of $\mathcal{R}_{SJB}$

5.1 Introduction

In Part I, Chapters 1 through 4, we explored the very best standardization possible. We used full spectrophotometric timeseries to find pairs that have the best-matching flux values at all phases and wavelengths and demonstrated that those pairs have a very low magnitude dispersion. There is, however, a long standing tradition of proceeding in the other direction, namely looking for the most simple approach that corrects for the bulk of the dispersion in the supernova population. If a correction with a small amount of data can produce a low dispersion, it is encouraging for future projects, as spectrophotometric timeseries are certainly observationally costly, which is why the next avenue of study for the Twins analysis is to test the performance under the degradation of data quality.

There are other shortcuts that have shown promise. One such study was done by Bailey et al. [2009] (hereafter B09) also using data from the Nearby Supernova Factory, but instead of the full timeseries, using a single spectrophotometric observation for each supernova near maximum light. The study used spectral flux ratios to decrease the scatter around the Hubble line to ≈0.13 mag, a new standardization method that is competitive with the canonical methods of combining stretch and color corrections. This represents a further study of the B09 result to see if it carries over to other data sets. It has been claimed, in e.g. Blondin et al. [2011], that the B09 result is not maintained in other data sets. We test the correction on the literature supernovae of Matheson et al. [2008].

5.2 Method Review

The B09 analysis was done in blinded fashion. The data were split into training and validation subsets. The best-performing spectral flux ratios found in the training set and via Monte Carlo before the performance was examined on the validation set.

The flux ratio method correlates the uncorrected Hubble diagram residuals with ratios of fluxes in near-maximum light spectra. Note that this method requires only a single flux-calibrated spectrum per SN, as opposed to stretch and color which require a well-sampled light curve in many bands. In B09, many good (correlation coefficient > 0.90) flux ratios were found. A Hubble diagram was then fit with a distance modulus given by $\mu_B = (m_B - M') + \gamma\mathcal{R}$, where m_B is the uncorrected rest-frame B-band magnitude and M' (which includes both the mean SN Ia absolute magnitude and the $\mathcal{R}$ intercept) and γ are fit in the χ^2 minimization of the residuals. The best of these ratios, $\mathcal{R}_{642/443} \equiv \mathcal{R}_{SJB}$ with a fitted $\gamma = 3.5$, gives a Hubble diagram with a very low scatter of 0.128 mag (combined training and validation subsets).

5.3 The Literature Supernovae

In order to further test this method, we perform the analysis on a sample of literature SNe. We use the 20 SNe from Matheson et al. [2008] (hereafter M08) having observations within ±2.5 days of maximum light (the phase requirement of B09) and coverage over both wavelength regions of interest for this flux ratio (2000 km/s bins around 6415Åand 4427Å). See Table 5.1 for a list of these 20 SNe and their associated photometric information.

SN	cz_{helio}	cz_{CMB}	m_B	Phase	$\bar{\mathcal{R}}_{SJB}$	$E(B-V)$
SN1997dt*	2149	1828	15.41(0.05)^a	1	0.910	0.057
SN1998aq	1184	1354	12.31(0.02)^b	1,2	0.404(0.013)	0.014
SN1998bp	3127	3048	15.28(0.05)^b	-2.5,-1.5,-0.5,0.5,1.5	0.723(0.106)	0.076
SN1998bu	897	1196	12.12(0.02)^b	-2.5,-2,-0.5	0.695(0.013)	0.025
SN1998de	4990	4671	17.30(0.05)^b	-2.5,-1.5,0	0.992(0.239)	0.057
SN1998dh	2678	2307	13.96(0.02)^a	0	0.553(0.190)	0.068
SN1998ec	5966	6032	16.09(0.05)^a	-2.5,-1.5	0.667(0.024)	0.085
SN1998eg	7423	7056	16.12(0.02)^a	0	0.550(0.190)	0.123
SN1998es	3168	2868	13.83(0.04)^b	-2,-1,1,2	0.452(0.012)	0.032
SN1998v	5268	5148	15.08(0.04)^a	0.5,1.5,2.5	0.423(0.017)	0.196
SN1999aa	4330	4572	14.72(0.03)^b	-2,-1,1	0.356(0.023)	0.040
SN1999ac	2848	2943	14.09(0.04)^b	-2.5,-0.5	0.419(0.004)	0.046
SN1999cc	9392	9452	16.76(0.02)^b	-1,0.5,2	0.519(0.033)	0.023
SN1999cl	2281	2605	14.87(0.04)^b	-2.5,-1.5,-0.5,1.5	1.980	0.038
SN1999dq*	4295	4060	14.42(0.08)^b	-2.5,-1.5,1,2	0.470	0.110
SN1999ej	4114	3831	15.36(0.05)^a	-0.5,2.5	0.569(0.005)	0.071
SN1999gd	5535	5775	16.85(0.05)^a	2.5	0.946(0.190)	0.041
SN1999gp*	8018	7806	15.99(0.05)^b	-1.5,0.5	0.463	0.056
SN2000dk	5228	4931	15.34(0.05)^b	1.5	0.545(0.126)	0.070
SN2000fa	6378	6533	15.71(0.04)^a	1.5,2.5	0.433(0.093)	0.069

Table 5.1 Summary of SNe used in the $\mathcal{R}_{SJB}$ literature cross check. Starred SNe are not included in the analysis due to host galaxy contamination in the spectra. cz_{helio} and $E(B-V)$ are from Matheson et al. [2008], Table 1. Phases are listed in days with respect to maximum light; all spectra within the ± 2.5 day acceptance window are listed. m_B with superscript a are from Jha et al. [2006], Table 7, while those with superscript b are from Hicken et al. [2009a], Table 3.

For photometry for these 20 SNe, we use a combination of two sources: Hicken et al. [2009a] (hereafter H09) and Jha et al. [2006] (hereafter J06). H09 has photometry for about half the SNe, while J06 has photometry for almost all. We choose to use H09 photometry when possible because J06 gives $B_{B_{max}}$, derived from a parabolic fit of the light curve to templates (see J06 page 549 for more details), and we expect H09 to have a more accurate m_B measurement as it is a more refined approach to fitting the data. (In section 5.4 we consider photometry solely from J06.) Note that the $B_{B_{max}}$ in J06 have not been corrected for Galactic extinction, so we correct them using the $E(B-V)$ values provided in J06. Uncertainties on $B_{B_{max}}$ are set to 0.05 mag unless provided in J06 (Table 8).

Three of the 20 SNe satisfying our phase and wavelength requirements are not included in any subsequent fitting due to strong H_α emission visible in the spectra, indicative of host galaxy contamination. These SNe are included in Table 5.1, for reference. Another SN, SN1999cl, is known to be unusually reddened with time-varying NaID; it is a significant outlier and does not pass outlier rejection in the fits.

Some SNe have multiple observations in the ± 2.5 day acceptance window; the phase of each accepted observation is listed in Table 5.1. $\mathcal{R}_{SJB}$ is calculated for each spectrum after deredshifting (using z_{helio}) and correcting for Galactic extinction. In cases of more than one usable spectrum, the mean value of $\mathcal{R}_{SJB}$ is given in the Table 5.1 and the uncertainty ($\sigma_{\mathcal{R}}$) is given by the dispersion in the individual $\mathcal{R}_{SJB}$ measurements. If only one spectrum falls in the acceptance window, we use spectral slope uncertainties derived by M08 from comparison with $B-V$ photometry, as discussed below. Note, however, that when using the dispersion as the uncertainty we are a assuming random scatter of the measurements; i.e. if all the measurements are wrong in the same way (e.g. from calibration errors) this approach will underestimate the uncertainty. We choose to do this in order to be the most conservative in our this cross check, giving the literature data the best chance to show tension with the result of B09.

When we cannot use the dispersion in $\mathcal{R}$ for $\sigma_{\mathcal{R}}$, we extrapolate the uncertainty from M08's values of σ_{B-V}. Figure 5.1 is taken from M08; it plots the $B-V$ color determined from a SN's spectrum versus the $B-V$ color determined from a SN's photometry (or the extrapolation thereof if no photometry was coincident) and uses the scatter to determine σ_{B-V}. Observations taken up to 1999 were not uniformly observed at the parallactic angle; they have $\sigma_{B-V} = 0.095$. Beginning in 2000, observations were completed at the parallactic angle and the scatter drops to $\sigma_{B-V} = 0.063$ (for observations within 20 days of maximum light). To estimate $\sigma_{\mathcal{R}}$, we correct for the longer baseline of the $\mathcal{R}$ wavelength range: $\sigma_{\mathcal{R}} = \sigma_{B-V}(642-443)/(540-442)$, where 540(442) is the central wavelength of the $B(V)$ filter in nm and 642(443) is the red(blue) wavelength used in $\mathcal{R}_{SJB}$.

5.4 Dispersion Results

In order to test the correlation, we must account for the various sources of error on our measurements, which are broken down in Table 5.2. Uncertainties on m_B are as described in the previous section. We also include the effects of peculiar velocity on the Hubble residual as: $\sigma_{v_{pec}} = (5/ln(10)) * (\sigma_{cz}/cz) = 0.0022/cz$ for $\sigma_{cz} = 300km/s$, a reasonable value. Both values for the uncertainty in $\mathcal{R}$ are listed, $\sigma_{\mathcal{R}}$ for uncertainty from the dispersion in $\mathcal{R}$ and

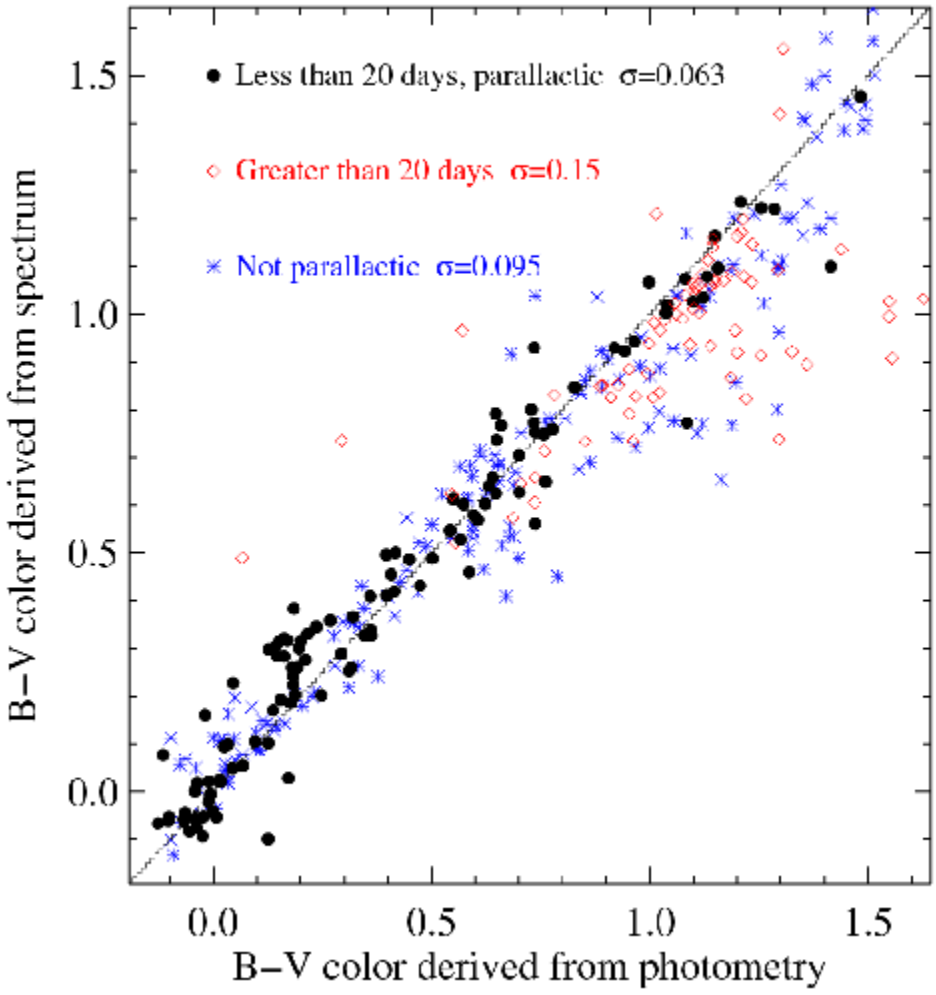

Figure 5.1 From Matheson et al. [2008]; $B-V$ color from photometry versus $B-V$ color from spectroscopy. Used to estimate $\sigma_{\mathcal{R}}$ when a dispersion of $\mathcal{R}$ measurements is not available.

SN	σ_{m_B}	$\sigma_{v_{pec}}$	$\sigma_{\mathcal{R}}$	$\sigma'_{\mathcal{R}}$	Residual
SN1998aq	0.02	0.487	0.013	0.190	-0.158
SN1998bp	0.05	0.217	0.106	0.190	-0.230
SN1998bu	0.02	0.552	0.013	0.190	0.798
SN1998de	0.05	0.141	0.239	0.190	-0.365
SN1998dh	0.02	0.286	...	0.190	-0.123
SN1998ec	0.05	0.109	0.024	0.190	0.245
SN1998eg	0.02	0.094	...	0.190	0.145
SN1998es	0.04	0.230	0.012	0.190	0.122
SN1998v	0.04	0.128	0.017	0.190	0.048
SN1999aa	0.03	0.144	0.023	0.190	-0.098
SN1999ac	0.04	0.224	0.004	0.190	-0.201
SN1999cc	0.02	0.070	0.033	0.190	0.021
SN1999ej	0.05	0.172	0.005	0.190	-0.359
SN1999gd	0.05	0.114	...	0.190	0.382
SN2000dk	0.05	0.134	...	0.126	0.123
SN2000fa	0.04	0.101	0.093	0.126	-0.032

Table 5.2 Summary of error budget of SNe used in the $\mathcal{R}_{SJB}$ literature cross check corresponding to the fit of panel *a* of Figure 5.4

.

$\sigma'_{\mathcal{R}}$ for uncertainty estimated from σ_{B-V}. We note that in most cases (all but SN1998de, a 91bg-like SN), $\sigma'_{\mathcal{R}}$ is larger than $\sigma_{\mathcal{R}}$, so as discussed in the previous section, we choose to use the later when possible. The final column in the table is the residual from the fit corresponding to panel *a* of Figure 5.4. The primary contributor to the overall error for most SNe is the peculiar velocity uncertainty; the SNe from B09 are further out in the Hubble flow and as such not as affected by this uncertainty.

Figure 5.2 plots the raw Hubble diagram residual, $m_B - 5 * log_{10}(cz)$ (where cz is cz_{CMB}), as a function of $\mathcal{R}_{SJB}$. Values of the raw residual are not displayed because we do not include the contributions from H_0 or M as these constants are absorbed in the offset of the fit $\mu_B = (m_B - M') + \gamma\mathcal{R}$. Panel *a* shows the individual $\mathcal{R}$ values, while panel *b* shows the average $\bar{\mathcal{R}}$. The correlation is clearly seen, with $\rho = 0.90$ for $\bar{\mathcal{R}}$. Figure 5.3 is taken from B09 and shows these literature SNe over-plotted on the training and validation sets of B09. Note that SN1999cl is plotted in this figure and it is a clear outlier. The environment of SN1999cl is known to be unusual, with time-varying NaID [Blondin et al., 2009] and "highly non-standard dust" [Krisciunas et al., 2006]. SN1999cl is also a large outlier when corrected with the standard stretch and color corrections.

Figure 5.2 also shows the two corrections that were fit - the red solid line for a correction using the B09 value of $\gamma = 3.5$, fitting for the intercept, and the orange dashed line for a correction fitting for both the intercept and the slope (γ). These fits are done using $\bar{\mathcal{R}}$ and with errors from Table 5.2. Residuals from these fits are plotted in Figure 5.4, the top panel for a fixed $\gamma = 3.5$ and the bottom for a fitted $\gamma = 3.0$. The scatter of these two fits is $\sigma_{fix} = 0.20$ and $\sigma_{fit} = 0.19$, respectively. In both cases the dispersion is higher than the value of $\sigma = 0.128$ found in B09, but the fits have $\chi^2_\nu = 0.7$ and $\chi^2_\nu = 0.8$, respectively, indicating that the dispersion is consistent with the measurement errors for these data and

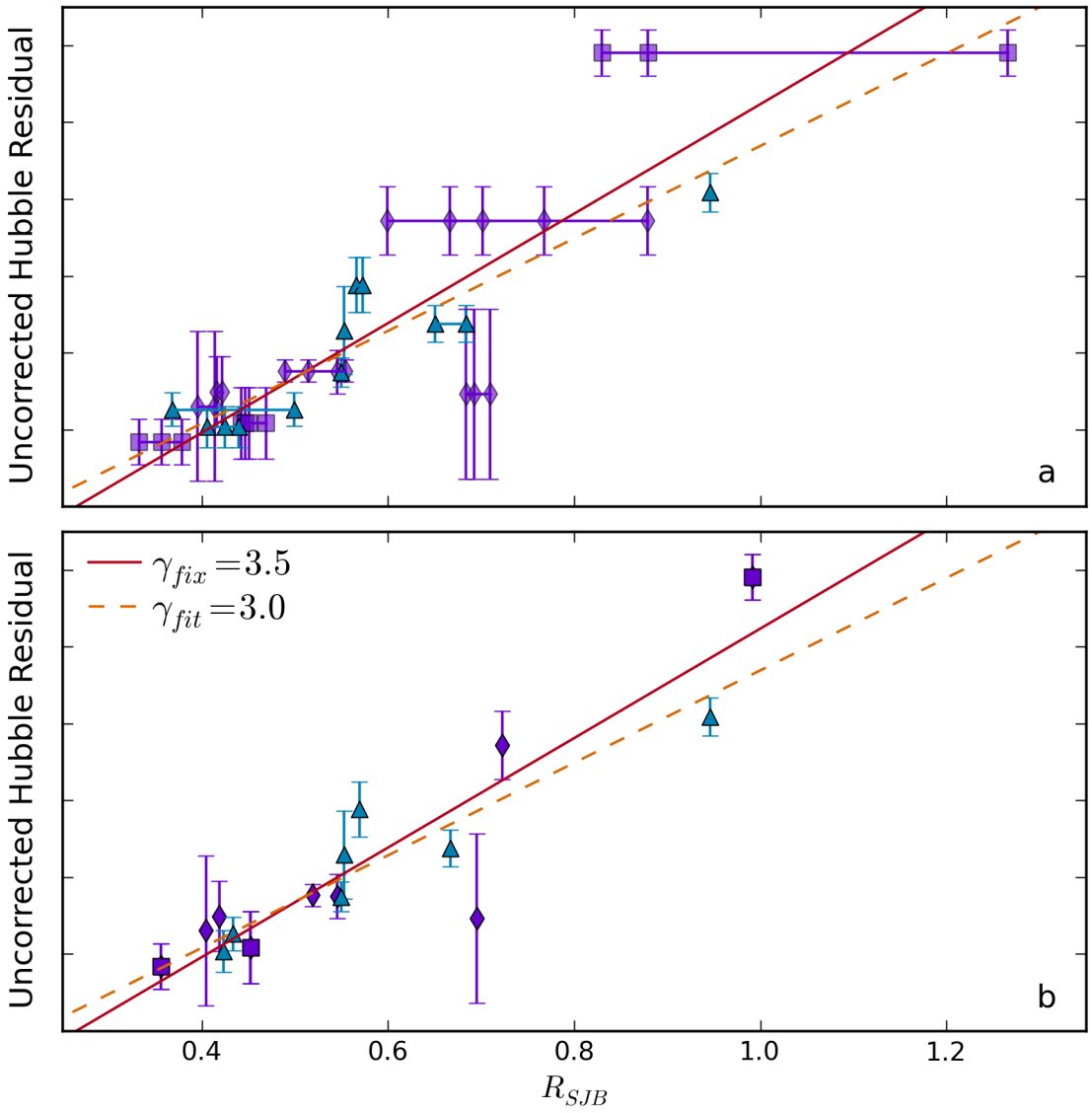

Figure 5.2 Uncorrected Hubble residuals as a function of $\mathcal{R}_{SJB}$. Panel *a* shows the individual $\mathcal{R}$ measurements for each SN connected with a thin line, while panel *b* shows $\bar{\mathcal{R}}$. In both panels the red solid line is the fit of the correlation using the B09 value of $\gamma = 3.5$; the dashed orange line is the fit allowing γ to float. SNe with photometry from H09 are plotted in purple as diamonds if they are normal SNe and as squares if they are 91bg- or 91t-like. SNe with photometry from J06 are plotted as cyan triangles.

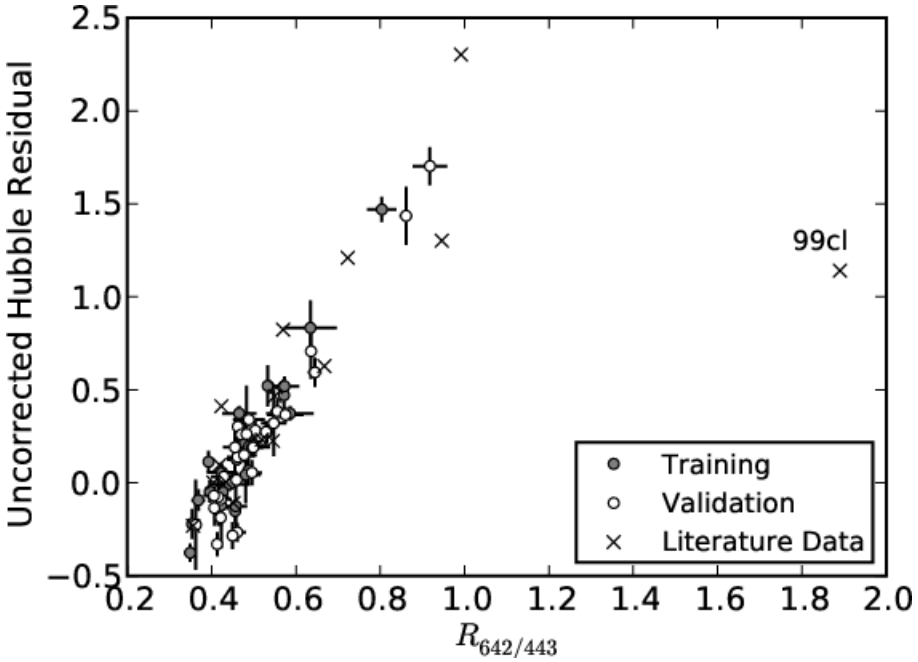

Figure 5.3 A figure from B09 showing their training (filled circles) and validation (open circles) SNe, as well as these literature SNe (crosses). SN1999cl is also plotted and labeled; it is clear that this SN does not pass outlier rejection cuts.

m_B from H09, J06			m_B from J06 only			m_B from R09-SALT		
γ	σ	χ^2_ν	γ	σ	χ^2_ν	γ	σ	χ^2_ν
3.5	0.20	0.77	3.5	0.19	0.80	3.5	0.17	0.41
3.0	0.19	0.73	3.1	0.18	0.80	3.3	0.16	0.42

Table 5.3 Summary of results for the slope γ, dispersion σ and χ^2_ν for the three different photometry sources: H09 and J06 combined; J06 alone, and R09-SALT fits.

.

the result does not contradict the low dispersion found in B09. We summarize the results in Table 5.3. Values for the dispersion do not change significantly when using $\gamma = 3.5$ or letting γ fit, though when fit the data prefer a lower value for γ.

As mentioned above, we do a consistency check of our result, using different sources of m_B to ensure that our choice to combine H09 and J06 for the primary result does not inject bias. We consider two alternatives - using m_B solely from J06 (possible for all SNe in the sample except SN1998aq) and using m_B from fits using a version of the SALT fitter [Guy et al., 2005]. For the latter, our m_B values come from private communication with D. Rubin, who used an altered version of the SALT fitter to fit the SNe (hereafter R09-SALT). Figure 5.5 shows the residuals from the fits for both of these alternatives and Table 5.3 summarizes the results. In all cases, the dispersion σ is higher than the B09 value, but the χ^2_ν are < 1, indicating consistency with the B09 result.

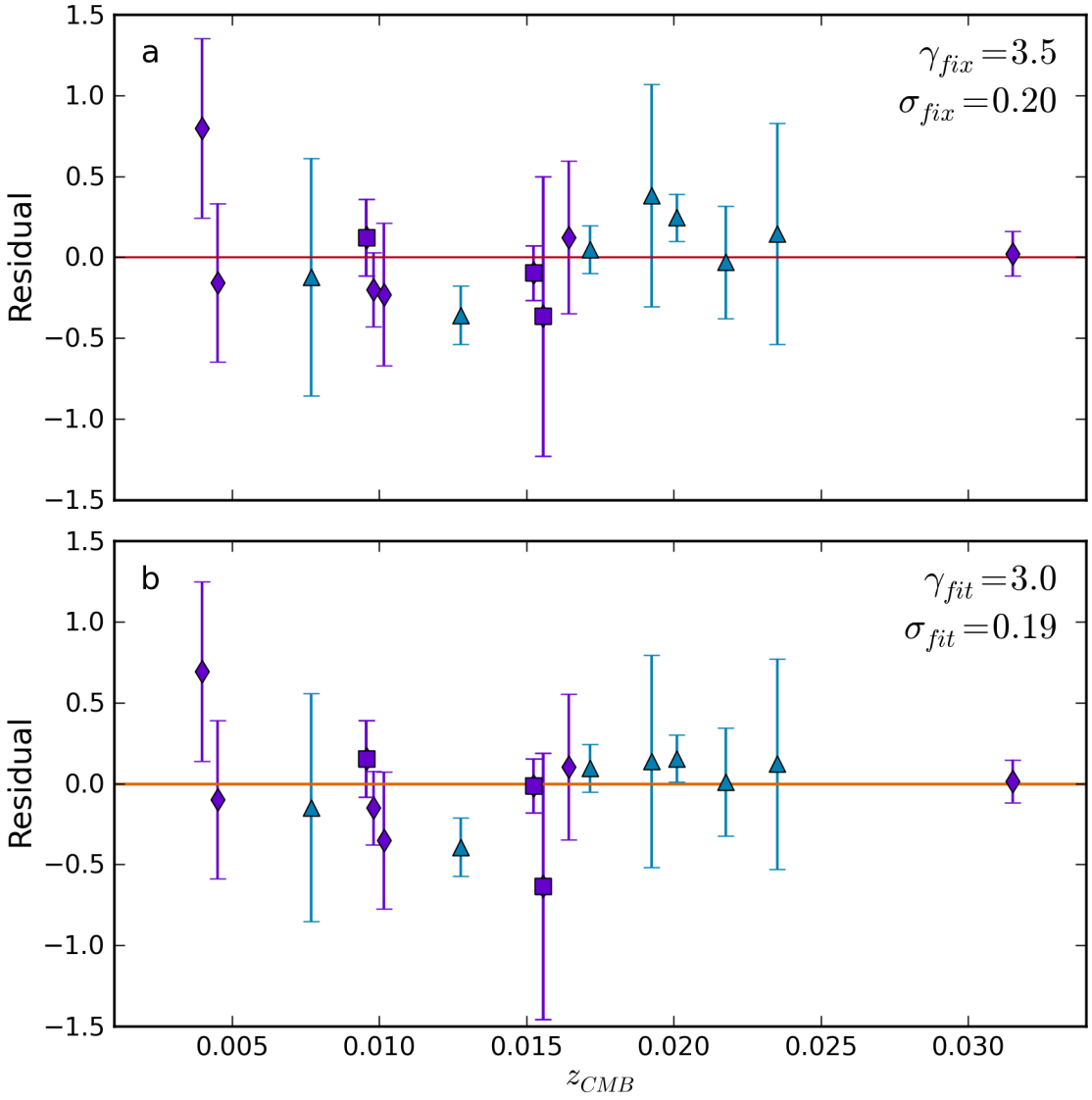

Figure 5.4 Residuals from fits of uncorrected Hubble residual to $\mathcal{R}_{SJB}$: $\delta HD = \gamma \mathcal{R}_{SJB} + M'$. Panel *a* shows residuals from the fit keeping γ fixed to the B09 value of 3.5 and fitting for the intercept M'. Panel *b* shows residuals from fitting for both γ and M'. In both panels, SNe with photometry from H09 are plotted in purple as diamonds if they are normal SNe and as squares if they are 91bg- or 91t-like. SNe with photometry from J06 are plotted as cyan triangles.

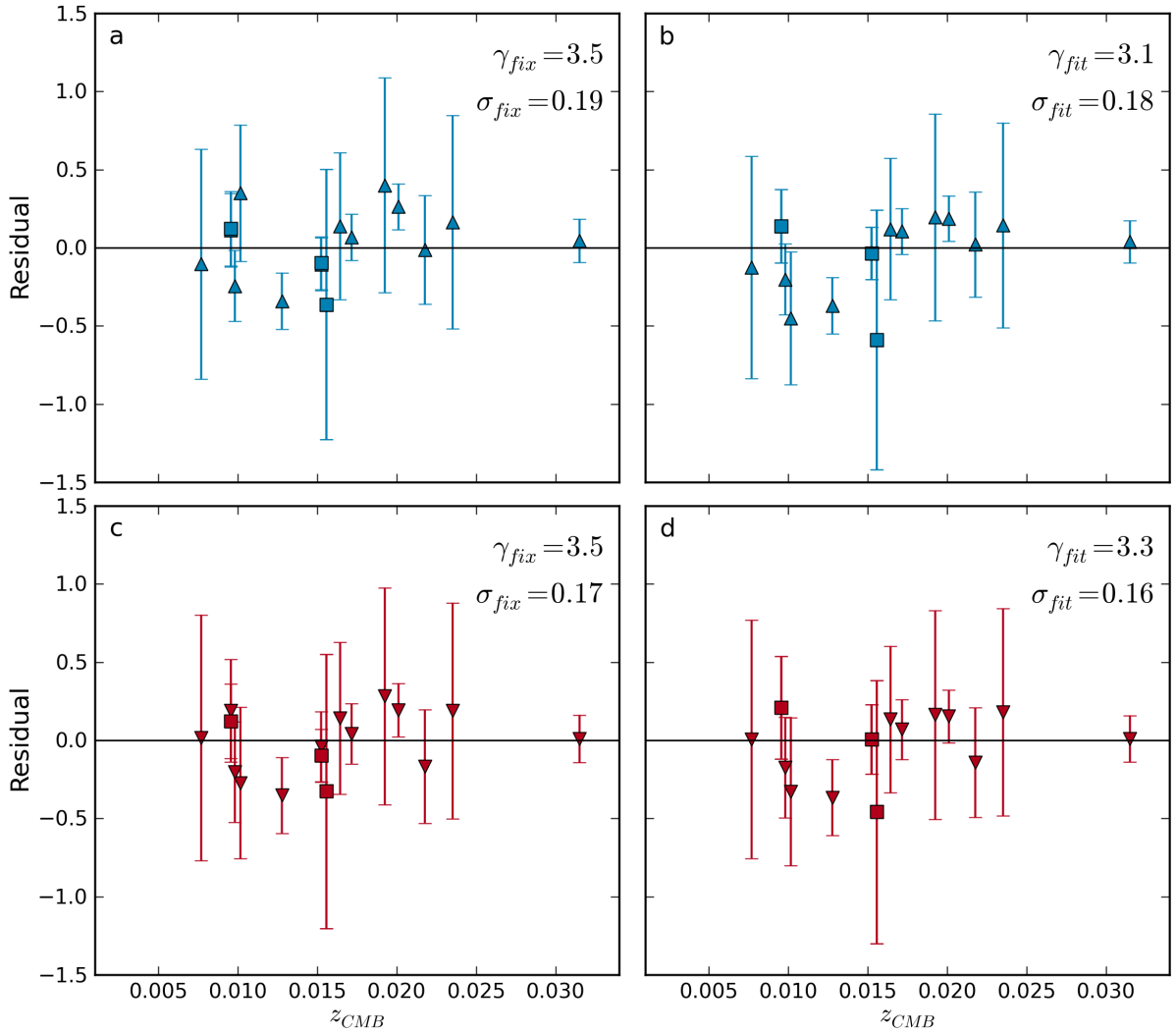

Figure 5.5 Residuals from Hubble diagram fits with m_B from J06 (panels a and b, cyan plots) and m_B from R09-SALT (panels c and d, red plots). Results fixing $\gamma - 3.5$ are shown in panels a and c and fitting γ in panels b and d. In all panels, 91bg- and 91t-like SNe are plotted as square symbols.

5.5 Summary

We tested the low dispersion result of B09 with a sample of SNe from the literature. We confirm the strong correlation of uncorrected Hubble diagram residuals with $\mathcal{R}_{642/443}$. The measurement errors on these literature SNe, though chosen as conservatively as is reasonable, are large and dominated by uncertainty arising from peculiar velocities, resulting in $\chi^2_\nu < 1$ for all fits. The dispersion found for these data (0.16 mag to 0.20 mag depending on the photometry source used) is substantially larger than the 0.128 mag result of B09, but is consistent with the measurement errors. As such we cannot rule out the B09 result as has been suggested in Blondin et al. [2011].

Chapter 6

Monochromatic Hubble Diagrams and Flux Ratios

6.1 Introduction

As an extension of the analysis discussed in Chapter 5, we explore the possibility of avoiding using the SALT model altogether. Recall that the method of Bailey et al. [2009] uses a spectral flux ratio to correct the Hubble Diagram residuals calculated by fitting the supernova photometric data with the SALT light curve fitter.

Using data from an early processing run of the Nearby Supernova Factory, we explore using monochromatic Hubble diagram (McHD) residuals corrected with flux ratios as a way to standardize Type Ia supernova luminosities. We construct Hubble diagrams from flux values at a single wavelengths and explore the wavelengths that offer the lowest dispersion. We then correct these residuals with the method of Bailey et al. [2009]. The advantage of this approach is that it requires only a spectrophotometric observation near maximum light, whereas the canonical standardization mechanisms require a well-sampled light curve (photometry at many phases and in many bands) not only to produce a Hubble diagram but also to correct luminosities via light curve stretch and color.

As done with other analyses from the Nearby Supernova Factory, we divide the sample into a "training" and "validation" set - the same split that was used in Bailey et al. [2009]. This leaves us with a training sample of 28 SNe with spectra near maximum light (within 2.5 days). We proceed in our analysis development with these training SNe until all tuning and tweaking is complete and then unblind with the validation SNe.

6.2 Monochromatic Hubble Diagrams

To construct the Monochromatic Hubble Diagrams (McHDs) the spectra were first dereddened (to correct for Milky Way dust), deredshifted, and rebinned to $c\Delta\lambda/\lambda \sim 2000$ km/s bins to sample the features in the physically relevant velocity space on scales still smaller than the features themselves. For each wavelength bin, we fit magnitudes as a function of distance as:

$$log_{10}(flux(\lambda)) = log_{10}(1/d_L^2) + intercept$$

where the luminosity distance is calculated using $\Omega_\Lambda = 0.70$ and $\Omega_m = 0.30$. (The result is not sensitive to the exact values used given the low redshift of the sample.) We mandate a slope of one as we are interested in the spread about the best fit line. The fitted intercept absorbs the reference flux value in the magnitude definition as well as other constants in the luminosity distance-flux relation. An example of this fit for a particular wavelength value (λ =642 nm) is shown in Figure 6.1.

We complete this procedure for all wavelength bins and determine the RMS about the best fit line; results are displayed in Figure 6.2. The error on the RMS is determined with a jackknife procedure, removing each SN in turn and calculating the standard deviation of the differences in RMS with and without each SN. The wavelength region around 640 nm has the lowest RMS and corresponds to the red shoulder of the primary SiII feature. Interestingly, one of the wavelengths in the Bailey et al. [2009] study is in this regime - namely 642 nm. The scatter in this region ($\sigma(\Delta\mu_\lambda) \sim 0.2$ mag) is substantially less than the uncorrected B-band scatter ($\sigma(\Delta\mu_B) \sim 0.4$ mag). However, standard stretch and color corrections are able to bring the scatter down to ~ 0.15 mag, so we cannot simply use McHDs.

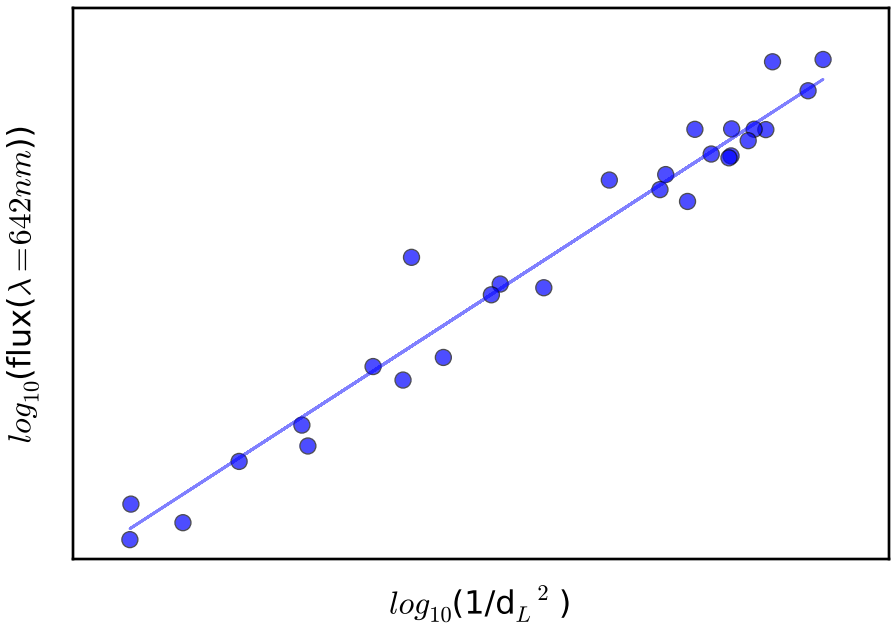

Figure 6.1 Relation between luminosity distance (calculated from the concordance cosmology) and the magnitudes of SNe in the training set (blue circles). The linear fit is mandated to have a slope of one.

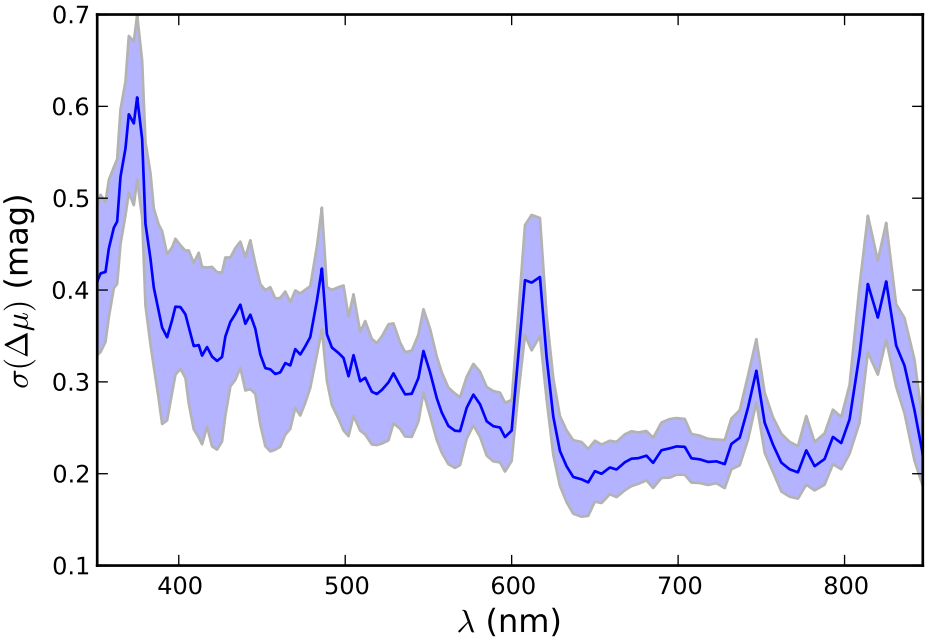

Figure 6.2 RMS about monochromatic Hubble diagrams for each wavelength; error on the RMS is shown as the light blue contour.

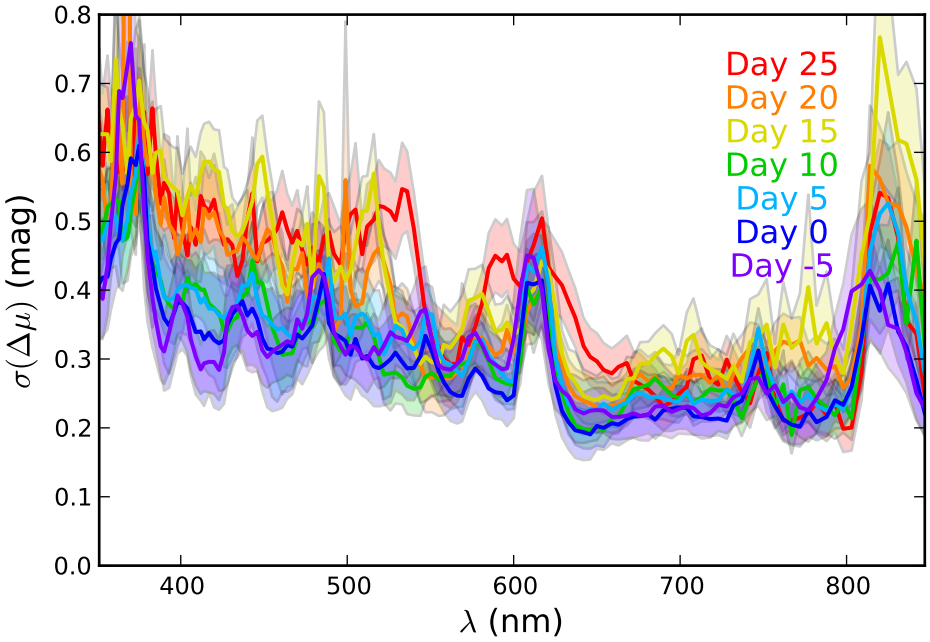

Figure 6.3 Scatter about monochromatic Hubble diagrams as a function of wavelength for different SN phases. Shaded contours about each line represent the error on the RMS. For each phase bin, SNe with phases within 2.5 days of the nominal phase are included.

Additionally it is possible to consider McHDs away from maximum light; it could be that SNe are naturally more standard at other phases in their evolution. McHD residual RMSs for bins in 5 days are shown in Figure 6.3. For almost all phases the red shoulder of the SiII feature is an area of low scatter, indicating that SNe share a high degree of similarity at these wavelengths across many phases. Although much could be done to continue exploring monochromatic Hubble diagrams, we choose a single one (642 nm at maximum light) and look for flux ratio corrections in the hopes of finding a competitive set of corrections.

6.3 Flux Ratio Corrections

As discussed in the previous section, we use the monochromatic Hubble diagram at $\lambda = 642$ nm at maximum light because this wavelength is in the region of low-scatter and it is one of the wavelengths identified in Bailey et al. [2009]. Whereas that analysis chose to look for correlations between Hubble residuals and flux ratios, here we search directly for flux ratios that give low residual scatter: $\sigma(\Delta\mu_{642})$; although this represents a practical difference it amounts to a similar search, as only flux ratios with good correlations have a hope of having a low $\sigma(\Delta\mu_{642})$. We explore flux ratios, $\mathcal{R}_{x/y} = f(\lambda = x)/f(\lambda = y)$, over the whole wavelength range. For each flux ratio, we fit $\Delta\mu_{642} = a\mathcal{R}_{x/y} + b$, a form analogous to the standard corrections of the form $\mu_B = (m_B - M) + \alpha(s - 1) + \beta c$, where s is the stretch, c is the color, and α and β are fitted coefficients. The color density plot in Figure 6.4 shows the resultant $\sigma(\Delta\mu_{642})$ for each flux ratio. The plot is almost symmetric, but will vary

Correction Parameter	Correction Slope		Residual Scatter	
	Train	Full	Train	Full
$\mathcal{R}_{642/443}$	-1.6	-1.5	0.110±0.015	0.141±0.014
$\mathcal{R}_{642/512}$	-2.3	-2.0	0.108±0.014	0.146±0.014

Table 6.1 Flux ratio $\mathcal{R}$ corrections to monochromatic Hubble diagrams and residual scatter.

somewhat as a fit of $\Delta\mu_{642} = a\mathcal{R}_{x/y} + b$ will not yield identical results as $\Delta\mu_{642} = a\mathcal{R}_{y/x} + b$.

It is immediately apparent that there are some flux ratios that yield a $\sigma(\Delta\mu_{642}) \sim 0.1$ mag, which would be a substantial improvement over current correction methods. Before we consider unblinding, we must choose which flux ratios to consider. Because we have the Bailey et al. [2009] results, we choose to use two of the flux ratios identified in that analysis, namely $\mathcal{R}_{642/443}$ and $\mathcal{R}_{642/512}$, the former as it is the primary ratio used and the latter as it has a low scatter in this analysis. Results from the training set are listed in Table 6.4.

In order to assess the statistical significance of these results before unblinding, we perform a Monte Carlo test. For each of 10,000 trials, monochromatic Hubble diagram residuals ($\Delta\mu_{642}$) are randomized, corrections are performed for all possible flux ratios, and the lowest $\sigma(\Delta\mu_{642})$ is stored. A histogram of the resulting $\sigma(\Delta\mu_{642})$ values is shown in Figure 6.5. The two vertical lines show the scatter for $\mathcal{R}_{642/443}$ and $\mathcal{R}_{642/512}$. The probability that random fluctuations can attain the low level of scatter found is 2.2% (1.6%) for $\sigma(\Delta\mu_{642})$ =0.110 mag (0.108 mag), corresponding to 2.3σ (2.5σ). Since low scatters are obtainable through randomization of the Hubble residuals, we will not be surprise if upon unblinding we see our good result above fail, as the low scatters could be statistical fluctuations.

6.4 Results Summary

We choose to unblind only the two flux ratios listed above and the results are listed in Table 6.4. The low dispersion result does not hold in the full sample. In order to test if the training and validation sets sample the same parent population, we perform a K-S test on the training and validation McHD residuals for all wavelengths (i.e. not just 642 nm). The sets are consistent with coming from the same larger sample. However, this does not test for systematic bias, so for each wavelength the RMS of the validation and training sets are compared and the "winner" is noted. The validation set has a higher RMS 86% of the time, which points to possible significant bias. It is possible that additional data (soon on hand with the SNfactory) will will not exhibit this bias between the training and validation sets and a return to this type of analysis will be warranted.

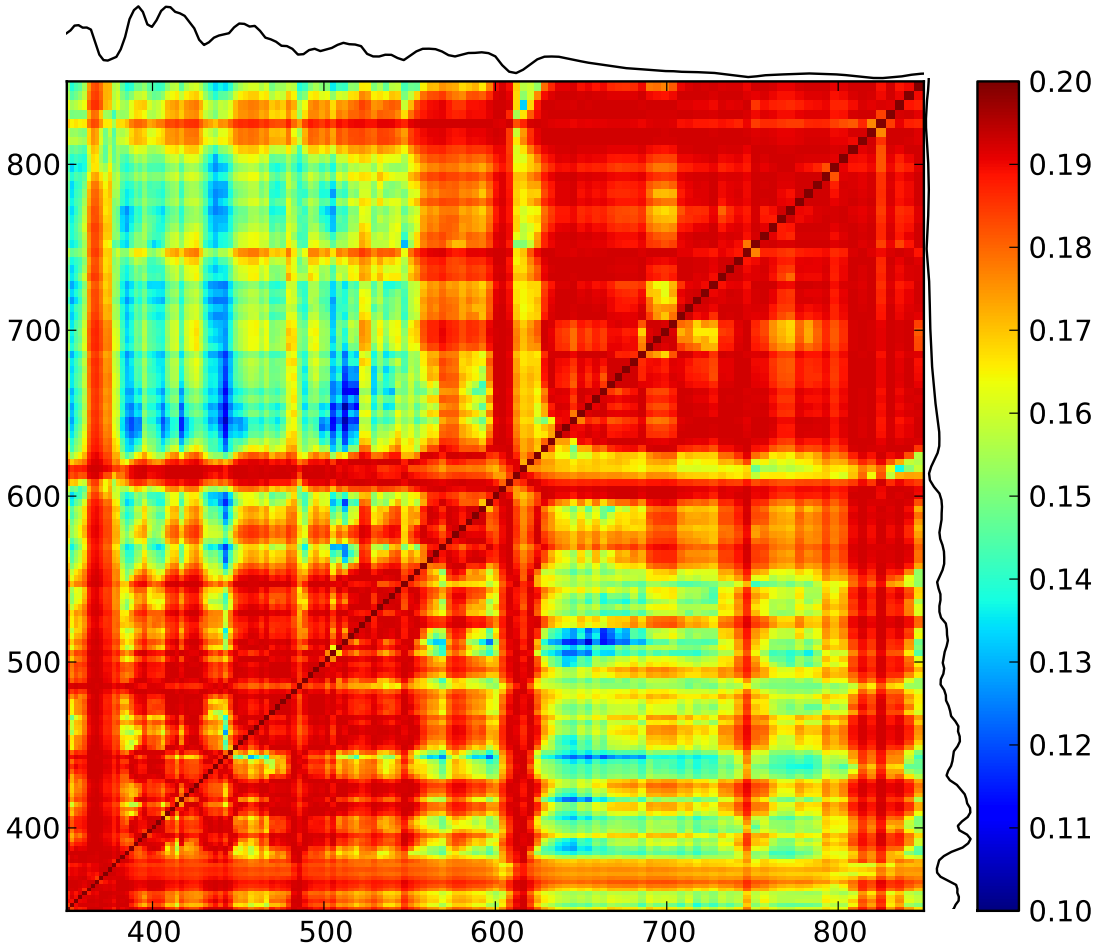

Figure 6.4 Color density map of $\sigma(\Delta\mu_{642})$ for all possible flux ratios. In most regions the scatter is around the pre-corrected value of 0.2 mag, indicating that the flux ratio correction does hot help. The blue patches show many instances where the scatter is reduced to almost 0.1 mag.

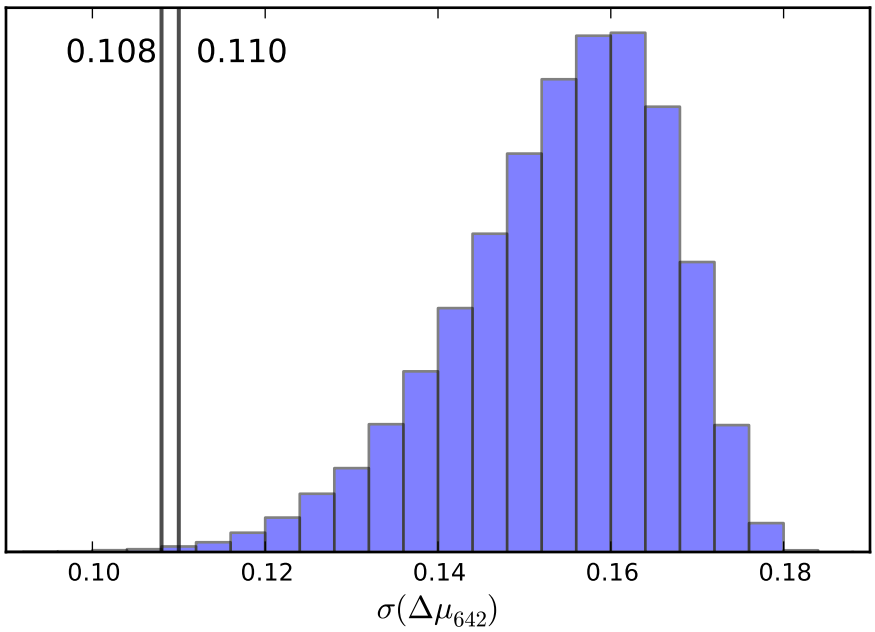

Figure 6.5 Results from the Monte Carlo permutation test. Vertical lines show the two $\sigma(\Delta\mu_{642})$ values corresponding to flux ratios $\mathcal{R}_{642/443}$ and $\mathcal{R}_{642/512}$. Note that there are some permutations that produce $\sigma(\Delta\mu_{642})$ values below the displayed values, indicating they may be the result of statistical fluctuations and may not hold after unblinding.

Chapter 7

Future Directions

This work has only begun to explore all that can be studied within the twin supernova paradigm. The low-dispersion result is highly encouraging and sets the bar for the goals of future Type Ia Supernova observations and analysis tools.

Before applying our method to high redshift, much study is still to be done to understand just what data quality and quantity are necessary to reproduce the low-dispersion result. Using the final pipeline production of the Nearby Supernova Factory data set will also allow us to test the twins result on a larger number of supernovae.

We can complete a thorough test of data quality; the analysis presented here used a highly selective subset of supernovae, those with no observable flaws. It remains to be answered just how selective we need to be to reproduce the low-dispersion result.

Tests on data quantity are also important, specifically studies of how coarse the resolution can be as well as further studies of whether a single at-max spectrum is sufficient to recover the low-dispersion result.

Although there is substantial work in executing these tests, specifically in training Gaussian Process models on new data, the foundation is laid here for how to utilize this method for high-redshift data and further decrease the uncertainty on cosmological parameters.

Clearly the approach presented here for identifying twin supernovae is not the only approach, nor is it necessarily the optimal approach. It was chosen for its transparency but there are many other statistical techniques one might want to move toward. Principle component analyses (PCA), for instance, could potentially reduce the dimensionality while still achieving a low dispersion. Of particular use may be the tools developed in Bailey [2012] for performing PCA analyses on noisey datasets.

There is also the need to develop practical analysis tools to fit cosmological parameters from the datasets. The standard technique today is to use light curve fitters, such as SALT2 [Guy et al., 2007a], which only have a few continuous parameters. From this twins analysis it is clear that there are many subgroupings within the Type Ia supernova population, and they may not lend themselves to continuous parameters. New light curve fitting tools will need to be developed to fully take advantage of all the information supernovae data have to offer.

Bibliography

E. Agol, H. Aihara, C. Allende Prieto, D. An, et al. The Eighth Data Release of the Sloan Digital Sky Survey: First Data from SDSS-III. submitted, January 2011.

G. Aldering, P. Antilogus, S. Bailey, C. Baltay, A. Bauer, N. Blanc, S. Bongard, Y. Copin, E. Gangler, S. Gilles, R. Kessler, D. Kocevski, B. C. Lee, S. Loken, P. Nugent, R. Pain, E. Pécontal, R. Pereira, S. Perlmutter, D. Rabinowitz, G. Rigaudier, R. Scalzo, G. Smadja, R. C. Thomas, L. Wang, and B. A. Weaver. Nearby Supernova Factory Observations of SN 2005gj: Another Type Ia Supernova in a Massive Circumstellar Envelope. *ApJ*, 650: 510–527, October 2006. doi: 10.1086/507020.

R. Amanullah, C. Lidman, D. Rubin, G. Aldering, P. Astier, K. Barbary, M. S. Burns, A. Conley, K. S. Dawson, S. E. Deustua, M. Doi, S. Fabbro, L. Faccioli, H. K. Fakhouri, G. Folatelli, A. S. Fruchter, H. Furusawa, G. Garavini, G. Goldhaber, A. Goobar, D. E. Groom, I. Hook, D. A. Howell, N. Kashikawa, A. G. Kim, R. A. Knop, M. Kowalski, E. Linder, J. Meyers, T. Morokuma, S. Nobili, J. Nordin, P. E. Nugent, L. Östman, R. Pain, N. Panagia, S. Perlmutter, J. Raux, P. Ruiz-Lapuente, A. L. Spadafora, M. Strovink, N. Suzuki, L. Wang, W. M. Wood-Vasey, N. Yasuda, and T. Supernova Cosmology Project. Spectra and Hubble Space Telescope Light Curves of Six Type Ia Supernovae at 0.511 ¡ z ¡ 1.12 and the Union2 Compilation. *ApJ*, 716:712–738, June 2010. doi: 10.1088/0004-637X/716/1/712.

P. Astier, J. Guy, N. Regnault, R. Pain, E. Aubourg, D. Balam, S. Basa, R. G. Carlberg, S. Fabbro, D. Fouchez, I. M. Hook, D. A. Howell, H. Lafoux, J. D. Neill, N. Palanque-Delabrouille, K. Perrett, C. J. Pritchet, J. Rich, M. Sullivan, R. Taillet, G. Aldering, P. Antilogus, V. Arsenijevic, C. Balland, S. Baumont, J. Bronder, H. Courtois, R. S. Ellis, M. Filiol, A. C. Gonçalves, A. Goobar, D. Guide, D. Hardin, V. Lusset, C. Lidman, R. McMahon, M. Mouchet, A. Mourao, S. Perlmutter, P. Ripoche, C. Tao, and N. Walton. The Supernova Legacy Survey: measurement of Ω_M, Ω_λ, and w from the first year data set. *A&A*, 447:31, February 2006. doi: 10.1051/0004-6361:20054185.

R. Bacon, G. Adam, A. Baranne, G. Courtes, D. Dubet, J. P. Dubois, E. Emsellem, P. Ferruit, Y. Georgelin, G. Monnet, E. Pecontal, A. Rousset, and F. Say. 3D spectrography at high spatial resolution. I. Concept and realization of the integral field spectrograph TIGER. *A&AS*, 113:347, October 1995.

R. Bacon, E. Emsellem, Y. Copin, and G. Monnet. Supermassive Black Hole Searches with 3-D Spectroscopy. In W. van Breugel and J. Bland-Hawthorn, editors, *Imaging the Universe*

in Three Dimensions, volume 195 of *Astronomical Society of the Pacific Conference Series*, page 173, 2000.

R. Bacon, Y. Copin, G. Monnet, B. W. Miller, J. R. Allington-Smith, M. Bureau, C. M. Carollo, R. L. Davies, E. Emsellem, H. Kuntschner, R. F. Peletier, E. K. Verolme, and P. T. de Zeeuw. The SAURON project - I. The panoramic integral-field spectrograph. *MNRAS*, 326:23–35, September 2001. doi: 10.1046/j.1365-8711.2001.04612.x.

S. Bailey. Principal Component Analysis with Noisy and/or Missing Data. *PASP*, 124: 1015–1023, September 2012. doi: 10.1086/668105.

S. Bailey, G. Aldering, P. Antilogus, C. Aragon, C. Baltay, S. Bongard, C. Buton, M. Childress, N. Chotard, Y. Copin, E. Gangler, S. Loken, P. Nugent, R. Pain, E. Pecontal, R. Pereira, S. Perlmutter, D. Rabinowitz, G. Rigaudier, K. Runge, R. Scalzo, G. Smadja, H. Swift, C. Tao, R. C. Thomas, C. Wu, and The Nearby Supernova Factory. Using spectral flux ratios to standardize SN Ia luminosities. *A&A*, 500:L17–L20, June 2009. doi: 10.1051/0004-6361/200911973.

C. Balland, S. Baumont, S. Basa, M. Mouchet, D. A. Howell, P. Astier, R. G. Carlberg, A. Conley, D. Fouchez, J. Guy, D. Hardin, I. M. Hook, R. Pain, K. Perrett, C. J. Pritchet, N. Regnault, J. Rich, M. Sullivan, P. Antilogus, V. Arsenijevic, J. Le Du, S. Fabbro, C. Lidman, A. Mourão, N. Palanque-Delabrouille, E. Pécontal, and V. Ruhlmann-Kleider. The ESO/VLT 3rd year Type Ia supernova data set from the supernova legacy survey. *A&A*, 507:85, November 2009. doi: 10.1051/0004-6361/200912246.

K. Barbary, K. S. Dawson, K. Tokita, G. Aldering, R. Amanullah, N. V. Connolly, M. Doi, L. Faccioli, V. Fadeyev, A. S. Fruchter, G. Goldhaber, A. Goobar, A. Gude, X. Huang, Y. Ihara, K. Konishi, M. Kowalski, C. Lidman, J. Meyers, T. Morokuma, P. Nugent, S. Perlmutter, D. Rubin, D. Schlegel, A. L. Spadafora, N. Suzuki, H. K. Swift, N. Takanashi, R. C. Thomas, and N. Yasuda. Discovery of an Unusual Optical Transient with the Hubble Space Telescope. *ApJ*, 690:1358, January 2009. doi: 10.1088/0004-637X/690/2/1358.

R. L. Barone-Nugent, C. Lidman, J. S. B. Wyithe, J. Mould, D. A. Howell, I. M. Hook, M. Sullivan, P. E. Nugent, I. Arcavi, S. B. Cenko, J. Cooke, A. Gal-Yam, E. Y. Hsiao, M. M. Kasliwal, K. Maguire, E. Ofek, D. Poznanski, and D. Xu. Near-infrared observations of Type Ia supernovae: the best known standard candle for cosmology. *MNRAS*, 425: 1007–1012, September 2012. doi: 10.1111/j.1365-2966.2012.21412.x.

S. Baumont, C. Balland, P. Astier, J. Guy, D. Hardin, D. A. Howell, C. Lidman, M. Mouchet, R. Pain, and N. Regnault. PHotometry Assisted Spectral Extraction (PHASE) and identification of SNLS supernovae. *A&A*, 491:567–585, November 2008. doi: 10.1051/0004-6361: 200810210.

S. Blondin, J. L. Prieto, F. Patat, P. Challis, M. Hicken, R. P. Kirshner, T. Matheson, and M. Modjaz. A Second Case of Variable Na I D Lines in a Highly Reddened Type Ia Supernova. *ApJ*, 693:207–215, March 2009. doi: 10.1088/0004-637X/693/1/207.

S. Blondin, K. S. Mandel, and R. P. Kirshner. Do spectra improve distance measurements of Type Ia supernovae? *A&A*, 526:A81, February 2011. doi: 10.1051/0004-6361/201015792.

D. Branch, D. J. Jeffery, J. Parrent, E. Baron, M. A. Troxel, V. Stanishev, M. Keithley, J. Harrison, and C. Bruner. Comparative Direct Analysis of Type Ia Supernova Spectra. IV. Postmaximum. *PASP*, 120:135–149, February 2008. doi: 10.1086/527572.

T. J. Bronder, I. M. Hook, P. Astier, D. Balam, C. Balland, S. Basa, R. G. Carlberg, A. Conley, D. Fouchez, J. Guy, D. A. Howell, J. D. Neill, R. Pain, K. Perrett, C. J. Pritchet, N. Regnault, M. Sullivan, S. Baumont, S. Fabbro, M. Filliol, S. Perlmutter, and P. Ripoche. SNLS spectroscopy: testing for evolution in type Ia supernovae. *A&A*, 477: 717–734, January 2008. doi: 10.1051/0004-6361:20077655.

J. A. Cardelli, G. C. Clayton, and J. S. Mathis. The relationship between infrared, optical, and ultraviolet extinction. *ApJ*, 345:245, October 1989.

N. Chotard, E. Gangler, G. Aldering, P. Antilogus, C. Aragon, S. Bailey, C. Baltay, S. Bongard, C. Buton, A. Canto, M. Childress, Y. Copin, H. K. Fakhouri, E. Y. Hsiao, M. Kerschhaggl, M. Kowalski, S. Loken, P. Nugent, K. Paech, R. Pain, E. Pecontal, R. Pereira, S. Perlmutter, D. Rabinowitz, K. Runge, R. Scalzo, G. Smadja, C. Tao, R. C. Thomas, B. A. Weaver, C. Wu, and Nearby Supernova Factory. The reddening law of type Ia supernovae: separating intrinsic variability from dust using equivalent widths. *A&A*, 529: L4, May 2011. doi: 10.1051/0004-6361/201116723.

A. Conley, J. Guy, M. Sullivan, N. Regnault, P. Astier, C. Balland, S. Basa, R. G. Carlberg, D. Fouchez, D. Hardin, I. M. Hook, D. A. Howell, R. Pain, N. Palanque-Delabrouille, K. M. Perrett, C. J. Pritchet, J. Rich, V. Ruhlmann-Kleider, D. Balam, S. Baumont, R. S. Ellis, S. Fabbro, H. K. Fakhouri, N. Fourmanoit, S. González-Gaitán, M. L. Graham, M. J. Hudson, E. Hsiao, T. Kronborg, C. Lidman, A. M. Mourao, J. D. Neill, S. Perlmutter, P. Ripoche, N. Suzuki, and E. S. Walker. Supernova Constraints and Systematic Uncertainties from the First Three Years of the Supernova Legacy Survey. *ApJS*, 192:1, January 2011. doi: 10.1088/0067-0049/192/1/1.

M. Davis, S. M. Faber, J. Newman, A. C. Phillips, R. S. Ellis, C. C. Steidel, C. Conselice, A. L. Coil, D. P. Finkbeiner, D. C. Koo, P. Guhathakurta, B. Weiner, R. Schiavon, C. Willmer, N. Kaiser, G. A. Luppino, G. Wirth, A. Connolly, P. Eisenhardt, M. Cooper, and B. Gerke. Science Objectives and Early Results of the DEEP2 Redshift Survey. In *Discoveries and Research Prospects from 6- to 10-Meter-Class Telescopes II. Edited by Guhathakurta, Puragra. Proceedings of the SPIE, Volume 4834*, pages 161–172, February 2003.

S. M. Faber, A. C. Phillips, R. I. Kibrick, B. Alcott, S. L. Allen, J. Burrous, T. Cantrall, D. Clarke, A. L. Coil, D. J. Cowley, M. Davis, W. T. S. Deich, K. Dietsch, D. K. Gilmore, C. A. Harper, D. F. Hilyard, J. P. Lewis, M. McVeigh, J. Newman, J. Osborne, R. Schiavon, R. J. Stover, D. Tucker, V. Wallace, M. Wei, G. Wirth, and C. A. Wright. The DEIMOS spectrograph for the Keck II Telescope: integration and testing. 4841:1657–1669, March 2003. doi: 10.1117/12.460346.

R. J. Foley, D. A. Perley, D. Pooley, J. X. Prochaska, J. S. Bloom, W. Li, B. Cobb, H.-W. Chen, G. Aldering, C. Bailyn, C. H. Blake, E. E. Falco, P. J. Green, M. P. Kowalski, S. Perlmutter, K. Roth, and K. Volk. GRB 050408: A Bright Gamma-Ray Burst Probing an Atypical Galactic Environment. *ApJ*, 645:450–463, July 2006. doi: 10.1086/504313.

A. Gal-Yam, D. C. Leonard, D. B. Fox, S. B. Cenko, A. M. Soderberg, D.-S. Moon, D. J. Sand, W. Li, A. V. Filippenko, G. Aldering, and Y. Copin. On the Progenitor of SN 2005gl and the Nature of Type IIn Supernovae. *ApJ*, 656:372–381, February 2007. doi: 10.1086/510523.

P. M. Garnavich, S. Jha, P. Challis, A. Clocchiatti, A. Diercks, A. V. Filippenko, R. L. Gilliland, C. J. Hogan, R. P. Kirshner, B. Leibundgut, M. M. Phillips, D. Reiss, A. G. Riess, B. P. Schmidt, R. A. Schommer, R. C. Smith, J. Spyromilio, C. Stubbs, N. B. Suntzeff, J. Tonry, and S. M. Carroll. Supernova Limits on the Cosmic Equation of State. *ApJ*, 509:74, December 1998.

J. Guy, P. Astier, S. Nobili, N. Regnault, and R. Pain. SALT: a spectral adaptive light curve template for type Ia supernovae. *A&A*, 443:781–791, December 2005. doi: 10.1051/0004-6361:20053025.

J. Guy, P. Astier, S. Baumont, D. Hardin, R. Pain, N. Regnault, S. Basa, R. G. Carlberg, A. Conley, S. Fabbro, D. Fouchez, I. M. Hook, D. A. Howell, K. Perrett, C. J. Pritchet, J. Rich, M. Sullivan, P. Antilogus, E. Aubourg, G. Bazin, J. Bronder, M. Filiol, N. Palanque-Delabrouille, P. Ripoche, and V. Ruhlmann-Kleider. SALT2: using distant supernovae to improve the use of type Ia supernovae as distance indicators. *A&A*, 466:11–21, April 2007a. doi: 10.1051/0004-6361:20066930.

J. Guy, P. Astier, S. Baumont, D. Hardin, R. Pain, N. Regnault, S. Basa, R. G. Carlberg, A. Conley, S. Fabbro, D. Fouchez, I. M. Hook, D. A. Howell, K. Perrett, C. J. Pritchet, J. Rich, M. Sullivan, P. Antilogus, E. Aubourg, G. Bazin, J. Bronder, M. Filiol, N. Palanque-Delabrouille, P. Ripoche, and V. Ruhlmann-Kleider. SALT2: using distant supernovae to improve the use of type Ia supernovae as distance indicators. *A&A*, 466:11–21, April 2007b. doi: 10.1051/0004-6361:20066930.

J. Guy, M. Sullivan, A. Conley, N. Regnault, P. Astier, C. Balland, S. Basa, R. G. Carlberg, D. Fouchez, D. Hardin, I. M. Hook, D. A. Howell, R. Pain, N. Palanque-Delabrouille, K. M. Perrett, C. J. Pritchet, J. Rich, V. Ruhlmann-Kleider, D. Balam, S. Baumont, R. S. Ellis, S. Fabbro, H. K. Fakhouri, N. Fourmanoit, S. González-Gaitán, M. L. Graham, E. Hsiao, T. Kronborg, C. Lidman, A. M. Mourao, S. Perlmutter, P. Ripoche, N. Suzuki, and E. S. Walker. The Supernova Legacy Survey 3-year sample: Type Ia supernovae photometric distances and cosmological constraints. *A&A*, 523:A7, November 2010. doi: 10.1051/0004-6361/201014468.

M. Hicken, P. Challis, S. Jha, R. P. Kirshner, T. Matheson, M. Modjaz, A. Rest, and W. M. Wood-Vasey. CfA3: 185 Type Ia Supernova Light Curves from the CfA. *ArXiv e-prints*, January 2009a.

M. Hicken, W. M. Wood-Vasey, S. Blondin, P. Challis, S. Jha, P. L. Kelly, A. Rest, and R. P. Kirshner. Improved Dark Energy Constraints from ˜100 New CfA Supernova Type Ia Light Curves. *ApJ*, 700:1097, August 2009b. doi: 10.1088/0004-637X/700/2/1097.

I. M. Hook, D. A. Howell, G. Aldering, R. Amanullah, M. S. Burns, A. Conley, S. E. Deustua, R. Ellis, S. Fabbro, V. Fadeyev, G. Folatelli, G. Garavini, R. Gibbons, G. Goldhaber, A. Goobar, D. E. Groom, A. G. Kim, R. A. Knop, M. Kowalski, C. Lidman, S. Nobili, P. E. Nugent, R. Pain, C. R. Pennypacker, S. Perlmutter, P. Ruiz-Lapuente, G. Sainton, B. E. Schaefer, E. Smith, A. L. Spadafora, V. Stanishev, R. C. Thomas, N. A. Walton, L. Wang, and W. M. Wood-Vasey. Spectra of High-Redshift Type Ia Supernovae and a Comparison with Their Low-Redshift Counterparts. *AJ*, 130:2788–2803, December 2005. doi: 10.1086/497635.

D. A. Howell, M. Sullivan, K. Perrett, T. J. Bronder, I. M. Hook, P. Astier, E. Aubourg, D. Balam, S. Basa, R. G. Carlberg, S. Fabbro, D. Fouchez, J. Guy, H. Lafoux, J. D. Neill, R. Pain, N. Palanque-Delabrouille, C. J. Pritchet, N. Regnault, J. Rich, R. Taillet, R. Knop, R. G. McMahon, S. Perlmutter, and N. A. Walton. Gemini Spectroscopy of Supernovae from the Supernova Legacy Survey: Improving High-Redshift Supernova Selection and Classification. *ApJ*, 634:1190–1201, December 2005. doi: 10.1086/497119.

E. Y. Hsiao, A. Conley, D. A. Howell, M. Sullivan, C. J. Pritchet, R. G. Carlberg, P. E. Nugent, and M. M. Phillips. K-Corrections and Spectral Templates of Type Ia Supernovae. *ApJ*, 663:1187–1200, July 2007. doi: 10.1086/518232.

S. Jha, R. P. Kirshner, P. Challis, P. M. Garnavich, T. Matheson, A. M. Soderberg, G. J. M. Graves, M. Hicken, J. F. Alves, H. G. Arce, Z. Balog, P. Barmby, E. J. Barton, P. Berlind, A. E. Bragg, C. Briceño, W. R. Brown, J. H. Buckley, N. Caldwell, M. L. Calkins, B. J. Carter, K. D. Concannon, R. H. Donnelly, K. A. Eriksen, D. G. Fabricant, E. E. Falco, F. Fiore, M. R. Garcia, M. Gómez, N. A. Grogin, T. Groner, P. J. Groot, K. E. Haisch, Jr., L. Hartmann, C. W. Hergenrother, M. J. Holman, J. P. Huchra, R. Jayawardhana, D. Jerius, S. J. Kannappan, D.-W. Kim, J. T. Kleyna, C. S. Kochanek, D. M. Koranyi, M. Krockenberger, C. J. Lada, K. L. Luhman, J. X. Luu, L. M. Macri, J. A. Mader, A. Mahdavi, M. Marengo, B. G. Marsden, B. A. McLeod, B. R. McNamara, S. T. Megeath, D. Moraru, A. E. Mossman, A. A. Muench, J. A. Muñoz, J. Muzerolle, O. Naranjo, K. Nelson-Patel, M. A. Pahre, B. M. Patten, J. Peters, W. Peters, J. C. Raymond, K. Rines, R. E. Schild, G. J. Sobczak, T. B. Spahr, J. R. Stauffer, R. P. Stefanik, A. H. Szentgyorgyi, E. V. Tollestrup, P. Väisänen, A. Vikhlinin, Z. Wang, S. P. Willner, S. J. Wolk, J. M. Zajac, P. Zhao, and K. Z. Stanek. UBVRI Light Curves of 44 Type Ia Supernovae. *AJ*, 131:527–554, January 2006. doi: 10.1086/497989.

R. Kessler, A. C. Becker, D. Cinabro, J. Vanderplas, J. A. Frieman, J. Marriner, T. M. Davis, B. Dilday, J. Holtzman, S. W. Jha, H. Lampeitl, M. Sako, M. Smith, C. Zheng, R. C. Nichol, B. Bassett, R. Bender, D. L. Depoy, M. Doi, E. Elson, A. V. Filippenko, R. J. Foley, P. M. Garnavich, U. Hopp, Y. Ihara, W. Ketzeback, W. Kollatschny, K. Konishi, J. L. Marshall, R. J. McMillan, G. Miknaitis, T. Morokuma, E. Mörtsell, K. Pan, J. L. Prieto, M. W. Richmond, A. G. Riess, R. Romani, D. P. Schneider, J. Sollerman, N. Takanashi,

K. Tokita, K. van der Heyden, J. C. Wheeler, N. Yasuda, and D. York. First-Year Sloan Digital Sky Survey-II Supernova Results: Hubble Diagram and Cosmological Parameters. *ApJS*, 185:32–84, November 2009. doi: 10.1088/0067-0049/185/1/32.

T. Kim, E. M. Hu, L. L. Cowie, and A. Songaila. The Redshift Evolution of the Ly alpha Forest. *AJ*, 114:1, July 1997.

K. Krisciunas, J. L. Prieto, P. M. Garnavich, J.-L. G. Riley, A. Rest, C. Stubbs, and R. McMillan. Photometry of the Type Ia Supernovae 1999cc, 1999cl, and 2000cf. *AJ*, 131:1639–1647, March 2006. doi: 10.1086/499523.

B. Lantz, G. Aldering, P. Antilogus, C. Bonnaud, L. Capoani, A. Castera, Y. Copin, D. Dubet, E. Gangler, F. Henault, J.-P. Lemonnier, R. Pain, A. Pecontal, E. Pecontal, and G. Smadja. SNIFS: a wideband integral field spectrograph with microlens arrays. In L. Mazuray, P. J. Rogers, and R. Wartmann, editors, *Society of Photo-Optical Instrumentation Engineers (SPIE) Conference Series*, volume 5249 of *Society of Photo-Optical Instrumentation Engineers (SPIE) Conference Series*, pages 146–155, February 2004. doi: 10.1117/12.512493.

T. Matheson, R. P. Kirshner, P. Challis, S. Jha, P. M. Garnavich, P. Berlind, M. L. Calkins, S. Blondin, Z. Balog, A. E. Bragg, N. Caldwell, K. Dendy Concannon, E. E. Falco, G. J. M. Graves, J. P. Huchra, J. Kuraszkiewicz, J. A. Mader, A. Mahdavi, M. Phelps, K. Rines, I. Song, and B. J. Wilkes. Optical Spectroscopy of Type ia Supernovae. *AJ*, 135:1598, April 2008. doi: 10.1088/0004-6256/135/4/1598.

J. B. Oke, J. G. Cohen, M. Carr, J. Cromer, A. Dingizian, F. H. Harris, S. Labrecque, R. Lucinio, W. Schaal, H. Epps, and J. Miller. The Keck Low-Resolution Imaging Spectrometer. *PASP*, 107:375–+, April 1995.

S. Perlmutter, G. Aldering, M. della Valle, S. Deustua, R. S. Ellis, S. Fabbro, A. Fruchter, G. Goldhaber, D. E. Groom, I. M. Hook, A. G. Kim, M. Y. Kim, R. A. Knop, C. Lidman, R. G. McMahon, P. Nugent, R. Pain, N. Panagia, C. R. Pennypacker, P. Ruiz-Lapuente, B. Schaefer, and N. Walton. Discovery of a supernova explosion at half the age of the universe. *Nature*, 391:51, January 1998.

S. Perlmutter, G. Aldering, G. Goldhaber, R. A. Knop, P. Nugent, P. G. Castro, S. Deustua, S. Fabbro, A. Goobar, D. E. Groom, I. M. Hook, A. G. Kim, M. Y. Kim, J. C. Lee, N. J. Nunes, R. Pain, C. R. Pennypacker, R. Quimby, C. Lidman, R. S. Ellis, M. Irwin, R. G. McMahon, P. Ruiz-Lapuente, N. Walton, B. Schaefer, B. J. Boyle, A. V. Filippenko, T. Matheson, A. S. Fruchter, N. Panagia, H. J. M. Newberg, W. J. Couch, and The Supernova Cosmology Project. Measurements of Omega and Lambda from 42 High-Redshift Supernovae. *ApJ*, 517:565, June 1999.

R. M. Quimby, G. Aldering, J. C. Wheeler, P. Höflich, C. W. Akerlof, and E. S. Rykoff. SN 2005ap: A Most Brilliant Explosion. *ApJL*, 668:L99–L102, October 2007. doi: 10.1086/522862.

C. E. Rasmussen and C. K. I. Williams. *Gaussian Processes for Machine Learning*. The MIT Press, 2006.

A. G. Riess, A. V. Filippenko, P. Challis, A. Clocchiatti, A. Diercks, P. M. Garnavich, R. L. Gilliland, C. J. Hogan, S. Jha, R. P. Kirshner, B. Leibundgut, M. M. Phillips, D. Reiss, B. P. Schmidt, R. A. Schommer, R. C. Smith, J. Spyromilio, C. Stubbs, N. B. Suntzeff, and J. Tonry. Observational Evidence from Supernovae for an Accelerating Universe and a Cosmological Constant. *AJ*, 116:1009–1038, September 1998.

R. A. Scalzo, G. Aldering, P. Antilogus, C. Aragon, S. Bailey, C. Baltay, S. Bongard, C. Buton, M. Childress, N. Chotard, Y. Copin, H. K. Fakhouri, A. Gal-Yam, E. Gangler, S. Hoyer, M. Kasliwal, S. Loken, P. Nugent, R. Pain, E. Pécontal, R. Pereira, S. Perlmutter, D. Rabinowitz, A. Rau, G. Rigaudier, K. Runge, G. Smadja, C. Tao, R. C. Thomas, B. Weaver, and C. Wu. Nearby Supernova Factory Observations of SN 2007if: First Total Mass Measurement of a Super-Chandrasekhar-Mass Progenitor. *ApJ*, 713:1073–1094, April 2010. doi: 10.1088/0004-637X/713/2/1073.

B. P. Schmidt, N. B. Suntzeff, M. M. Phillips, R. A. Schommer, A. Clocchiatti, R. P. Kirshner, P. Garnavich, P. Challis, B. Leibundgut, J. Spyromilio, A. G. Riess, A. V. Filippenko, M. Hamuy, R. C. Smith, C. Hogan, C. Stubbs, A. Diercks, D. Reiss, R. Gilliland, J. Tonry, J. Maza, A. Dressler, J. Walsh, and R. Ciardullo. The High-Z Supernova Search: Measuring Cosmic Deceleration and Global Curvature of the Universe Using Type IA Supernovae. *ApJ*, 507:46–63, November 1998. doi: 10.1086/306308.

C. C. Steidel, K. L. Adelberger, A. E. Shapley, M. Pettini, M. Dickinson, and M. Giavalisco. Lyman Break Galaxies at Redshift z ˜ 3: Survey Description and Full Data Set. *ApJ*, 592: 728–754, August 2003. doi: 10.1086/375772.

M. Sullivan, D. Le Borgne, C. J. Pritchet, A. Hodsman, J. D. Neill, D. A. Howell, R. G. Carlberg, P. Astier, E. Aubourg, D. Balam, S. Basa, A. Conley, S. Fabbro, D. Fouchez, J. Guy, I. Hook, R. Pain, N. Palanque-Delabrouille, K. Perrett, N. Regnault, J. Rich, R. Taillet, S. Baumont, J. Bronder, R. S. Ellis, M. Filiol, V. Lusset, S. Perlmutter, P. Ripoche, and C. Tao. Rates and Properties of Type Ia Supernovae as a Function of Mass and Star Formation in Their Host Galaxies. *ApJ*, 648:868–883, September 2006. doi: 10.1086/506137.

M. Sullivan, J. Guy, A. Conley, N. Regnault, P. Astier, C. Balland, S. Basa, R. G. Carlberg, D. Fouchez, D. Hardin, I. M. Hook, D. A. Howell, R. Pain, N. Palanque-Delabrouille, K. M. Perrett, C. J. Pritchet, J. Rich, V. Ruhlmann-Kleider, D. Balam, S. Baumont, R. S. Ellis, S. Fabbro, H. K. Fakhouri, N. Fourmanoit, S. Gonzalez-Gaitan, M. L. Graham, M. J. Hudson, E. Hsiao, T. Kronborg, C. Lidmam, A. M. Mourao, J. D. Neill, S. Perlmutter, P. Ripoche, N. Suzuki, and E. S. Walker. SNLS3: Constraints on Dark Energy Combining the Supernova Legacy Survey Three Year Data with Other Probes. *ArXiv e-prints*, April 2011.

N. Suzuki, D. Rubin, C. Lidman, G. Aldering, R. Amanullah, K. Barbary, L. F. Barrientos, J. Botyanszki, M. Brodwin, N. Connolly, K. S. Dawson, A. Dey, M. Doi, M. Donahue, S. Deustua, P. Eisenhardt, E. Ellingson, L. Faccioli, V. Fadeyev, H. K. Fakhouri, A. S.

Fruchter, D. G. Gilbank, M. D. Gladders, G. Goldhaber, A. H. Gonzalez, A. Goobar, A. Gude, T. Hattori, H. Hoekstra, E. Hsiao, X. Huang, Y. Ihara, M. J. Jee, D. Johnston, N. Kashikawa, B. Koester, K. Konishi, M. Kowalski, E. V. Linder, L. Lubin, J. Melbourne, J. Meyers, T. Morokuma, F. Munshi, C. Mullis, T. Oda, N. Panagia, S. Perlmutter, M. Postman, T. Pritchard, J. Rhodes, P. Ripoche, P. Rosati, D. J. Schlegel, A. Spadafora, S. A. Stanford, V. Stanishev, D. Stern, M. Strovink, N. Takanashi, K. Tokita, M. Wagner, L. Wang, N. Yasuda, and H. K. C. Yee. The Hubble Space Telescope Cluster Supernova Survey: V. Improving the Dark Energy Constraints Above z¿1 and Building an Early-Type-Hosted Supernova Sample. *ArXiv:1105.3470*, May 2011.

E. S. Walker, I. M. Hook, M. Sullivan, D. A. Howell, P. Astier, C. Balland, S. Basa, T. J. Bronder, R. Carlberg, A. Conley, D. Fouchez, J. Guy, D. Hardin, R. Pain, K. Perrett, C. Pritchet, N. Regnault, J. Rich, G. Aldering, H. K. Fakhouri, T. Kronborg, N. Palanque-Delabrouille, S. Perlmutter, V. Ruhlmann-Kleider, and T. Zhang. Supernova Legacy Survey: using spectral signatures to improve Type Ia supernovae as distance indicators. *MNRAS*, 410:1262–1282, January 2011. doi: 10.1111/j.1365-2966.2010.17519.x.

W. M. Wood-Vasey, G. Miknaitis, C. W. Stubbs, S. Jha, A. G. Riess, P. M. Garnavich, R. P. Kirshner, C. Aguilera, A. C. Becker, J. W. Blackman, S. Blondin, P. Challis, A. Clocchiatti, A. Conley, R. Covarrubias, T. M. Davis, A. V. Filippenko, R. J. Foley, A. Garg, M. Hicken, K. Krisciunas, B. Leibundgut, W. Li, T. Matheson, A. Miceli, G. Narayan, G. Pignata, J. L. Prieto, A. Rest, M. E. Salvo, B. P. Schmidt, R. C. Smith, J. Sollerman, J. Spyromilio, J. L. Tonry, N. B. Suntzeff, and A. Zenteno. Observational Constraints on the Nature of Dark Energy: First Cosmological Results from the ESSENCE Supernova Survey. *ApJ*, 666:694, September 2007. doi: 10.1086/518642.

Part III

Appendices

Appendix A

Gaussian Processes

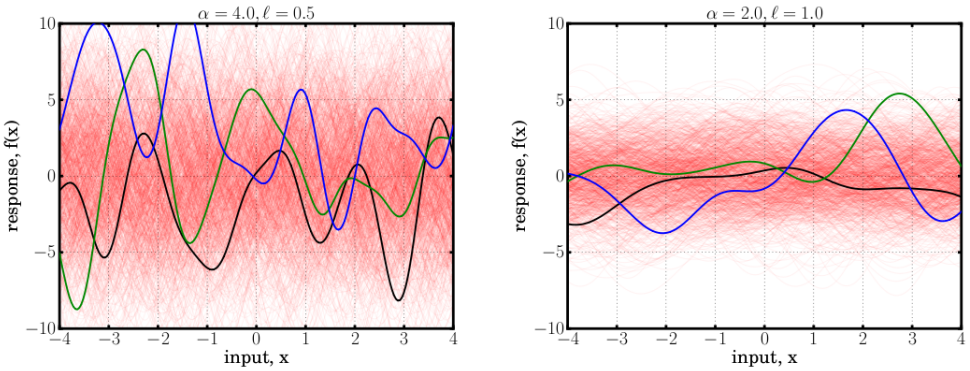

Figure A.1 Left panel: 1000 functions drawn at random from a GP prior, with zero mean, kernel of the form of Equation A.1 and hyperparameters $\alpha = 4.0$ and $l = 0.5$. Right panel: same as left panel but with hyperparameters $\alpha = 2.0$ and $l = 1.0$.

A.1 Gaussian Processes Introduction

Gaussian Processes (GPs) are a generalization of the Gaussian distribution. They allow a non-parametric reconstruction of a function from data and can be thought of as defining a distribution over functions. A GP is a collection of random variables ($f(x)$), any subset of which has a multivariate Gaussian distribution. They are completely described by a mean function $\mu(x)$ and covariance function $k(x, x')$: $f(x) \sim GP(\mu(x), k(x, x'))$ [Rasmussen and Williams, 2006]. The mean and covariance functions have hyperparameters that can be specified or can be learned by maximum-likelihood given some data.

As an example, consider a GP with mean function $\mu(x) = 0$ (i.e. a zero mean function) and kernel:

$$k(x, x') = \alpha^2 \exp(-\frac{|x - x'|^2}{2l^2}) + \sigma^2 \delta_{xx'}, \tag{A.1}$$

where the hyperparameters are: α (the amplitude), l (the length scale), and σ (the diagonal, i.i.d. noise). This is a commonly used covariance function (or kernel) called the "squared exponential." We can specify values for the hyperparameters and draw functions at random from the GP.

The left panel of Figure A.1 shows 1000 functions drawn at random from a GP prior with hyperparameters $\alpha = 4.0$ and $l = 0.5$; the right panel shows the same, but with different hyperparameters: $\alpha = 2.0$ and $l = 1.0$. (In both cases three of the random functions are plotted with thicker lines for clarity.) As can be seen from the figures, the amplitude hyperparameter α determines the typical spread in $f(x)$, and the length scale l determines the smoothness of the functions, i.e. how much change is needed in x to get a significant change in $f(x)$. The left panel has a larger α, resulting in a larger spread in $f(x)$ values for the 1000 realizations. The right panel has a larger l, resulting in smoother changes in $f(x)$.

If we have data, we can condition the GP prior on that data (called training data), as shown in Figure A.2. The left panel again shows 1000 functions, but now drawn from the GP conditioned on the training data (blue dots). The posterior mean is shown in black; it is constrained to go through the training data points and acts as an interpolation of the data. In the areas between the training data points, the spread in the realized functions (i.e. the

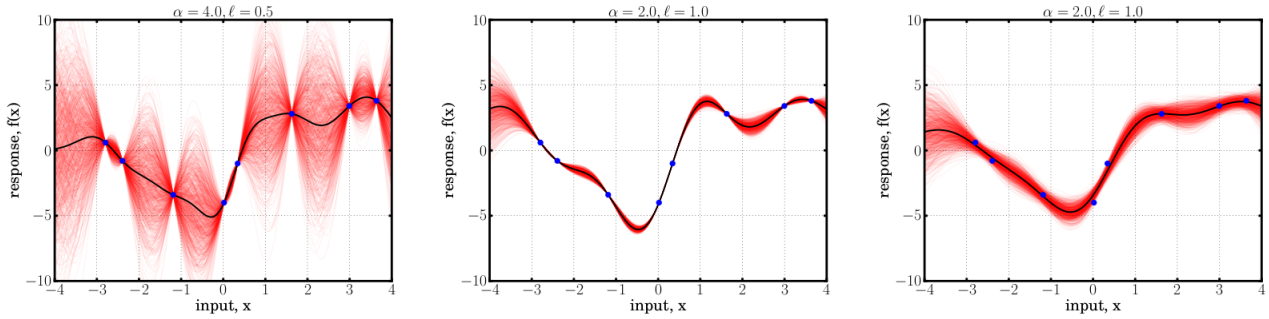

Figure A.2 Left panel: 1000 functions drawn from a GP prior conditioned on the training data (blue dots); posterior mean is shown in black. Middle panel: same as left panel but with different hyperparameter values. Right panel: similar to middle panel except including a term for i.i.d. noise in the kernel function.

error on the posterior mean) is a reflection of the hyperparameter values $\alpha = 4.0$ and $l = 0.5$. In the middle panel, the training data are the same, but the different hyperparameter values result in a different posterior mean and smaller spread in the realized functions. If we include the i.i.d. noise term in the kernel (Equation A.1; called the "nugget") and condition the GP prior on the same training data points, we get the right panel of Figure A.2. Here the posterior mean is no longer required to go through the data points and it acts as a smoothing of the data rather than a straight interpolation.

Formulaically (from Rasmussen and Williams [2006]), for a set of input points X_*, the values of the function are drawn from a Normal distribution

$$f_* \sim \mathcal{N}(\mu(X_*), K(X_*, X_*)), \tag{A.2}$$

where the covariance matrix K has elements filled with all input pairs of $k(x_{*,i}, x_{*,j})$. For y, a set of n measurements of f at inputs X, with measurement covariance V, a set of measurements and function values is drawn from a Normal distribution:

$$\begin{bmatrix} y \\ f_* \end{bmatrix} \sim \mathcal{N}\left(\begin{bmatrix} \mu(X) \\ \mu(X_*) \end{bmatrix}, \begin{bmatrix} K(X,X)+V & K(X,X_*) \\ K(X_*,X) & K(X_*,X_*) \end{bmatrix} \right) \tag{A.3}$$

The conditional distribution and function values is a Gaussian with expected mean

$$\bar{f}_* = \mu(X) + K(X_*, X)[K(X,X) + V]^{-1}(y - \mu(X)) \tag{A.4}$$

and covariance

$$\text{cov}(\bar{f}_*) = K(X_*, X_*) - K(X_*, X)[K(X,X) + V]^{-1}K(X, X_*). \tag{A.5}$$

In addition to conditioning the GP, the training data can be used to find the optimal hyperparameter values. This is done through maximizing the likelihood that the data arise from the given GP. The likelihood that y, a set of n measurements of f at inputs X with measurement covariance V is described by a Gaussian process is written as:

$$\ln\, p(y|X) = \frac{1}{2}(y - \mu(X))^T (K + V)^{-1}(y - \mu(X)) - \frac{1}{2}\ln\, |K + V| - \frac{n}{2}\ln\, 2\pi. \tag{A.6}$$

By finding the hyperparameter values that maximize this log likelihood, we obtain from the training data themselves what the best hyperparameter values are.

In summary, the basic outline is this: One has training data (a set of measurements y at inputs X with covariance V), chooses a mean function ($\mu(x)$) and kernel function ($k(x, x')$), optimizes the hyperparameters by maximizing the likelihood, chooses the locations (X_*) at which to predict the function, and calculates the predicted mean ($\bar{f}_*$) and covariance $\mathrm{cov}(\bar{f}_*)$. (In principle, one can also experiment with the choice of kernel and mean functions, as the likelihood gives a quantitative means of comparison.)

A.2 Gaussian Process Regression with SNfactory Data

For our analysis, the training data are the spectrophotometric flux values as a function of phase (with respect to light curve maximum) and wavelength. As a mean function we choose the spectral template of Hsiao et al. [2007] and allow one hyperparameter, θ_a, for an overall flux normalization constant. (Note that the mean function is what the GP prediction will default to in the absence of training data.) For our kernel, we use a squared exponential of the form:

$$k\left(\begin{bmatrix}\ln\lambda_i\\ t_i\end{bmatrix},\begin{bmatrix}\ln\lambda_j\\ t_j\end{bmatrix}\right)=\theta_s^2\exp\left(-\tfrac{1}{2}\begin{bmatrix}\ln\lambda_i-\ln\lambda_j\\ t_i-t_j\end{bmatrix}^T\begin{bmatrix}1/\theta_\lambda^2 & 0\\ 0 & 1/\theta_t^2\end{bmatrix}\begin{bmatrix}\ln\lambda_i-\ln\lambda_j\\ t_i-t_j\end{bmatrix}\right)+\theta_n^2\delta_{t_i,t_j} \tag{A.7}$$

We use the difference in $\ln\lambda$ as opposed to λ as velocity space is more physically relevant to supernova explosions; $\ln\lambda_r-\ln\lambda_b=\ln(1-v/c)$, so the wavelength length scale is thus a characteristic velocity, which is roughly wavelength independent for large features. θ_s is the amplitude hyperparameter and gives the scale of the GP prediction error when sufficiently far away from training data. θ_λ and θ_t are, respectively, the length scales in log wavelength and time. θ_n is the time nugget (which differs from i.i.d. noise in that it is non-zero when two data points are at the same phase) and accounts for wavelength-independent calibration errors and noise.

The hyperparameters for the mean and the kernel are learned simultaneously by maximum likelihood estimation for each individual time series. As we have ∼300 wavelength elements per spectrum and ∼10 spectra per supernova, a 3000x3000 covariance matrix must be decomposed each time the likelihood is calculated. This is computationally expensive, as the matrix must be decomposed at each optimization step as the hyperparameters are learned. (For our optimizer we use Minuit2.) Using the NERSC supercomputer Hopper, each learning run takes less than three minutes on a few hundred cores, using parallel distributed linear algebra routines (ScaLAPACK). We are then able to use these optimized hyperparameters to make predictions at any desired wavelengths and phases.

Of the 132 supernovae in the ACEv2 sample, 74 make it into the final sample for this analysis. (See Section 2.3 for details on sample selection.) Figure A.3 show histograms of the hyperparameter values for each of the five hyperparameters used in this analysis. The range of values for each of these hyperparameters is reasonable. We expect θ_a to be on order a few, as the mean template is normalized to one and the maximum supernova fluxes have been rescaled for this purpose to be on order a few. θ_s values ranging from 0.1 to

0.8 are also reasonable, as this hyperparameter is in essence the error in the GP sufficiently far away from data. For the time length scale θ_t, we have values ranging from $\sim$4 to $\sim$12. Although SNe vary on few day timescales (as is evidenced by examining their spectra), this hyperparameter value is affected by the data sampling as well as the overall smoothness of the data, as a shorter time length scale will allow for more variation in the GP predictions. The range of θ_λ corresponds to $\sim$2250 km s^{-1} to $\sim$7750 km s^{-1} (which in terms of Å is $\sim$25Å-85Å at the blue end and $\sim$65Å-215Å at the red end), a reasonable range given that SN features are $10^3 - 10^4$ km s^{-1}.

Figures A.4-A.7 show examples of GP predictions for four supernovae that represent different hyperparameter values. The first, Figure A.4, shows SNF20071015-000, which has the largest time length scale θ_t. The GP prediction in day intervals is shown in blue; in black are the data over-plotted on the day interval closest to the phase of the data. The other hyperparameters for this SN (displayed on the figure) are not particularly extreme. From the figure it is evident that this SN has a large degree of extrinsic reddening compared to the supernovae in the other figures. This reddening serves to make the SN more smooth in time than in would be otherwise, resulting in a larger θ_t; in fact all of the SNe in the sample with a large SALT2 color have $\theta_t > 9$ days.

Figure A.5 shows a particularly noisy SN: SNF20070528-003, which has the largest kernel amplitude hyperparameter θ_s. It is not surprising that a noisy SN would have a large θ_s, as θ_s gives the scale of the GP prediction error sufficiently far away from the data. Figure A.6 shows SNF20070831-015, which has a larger than average time nugget θ_n. Examining the data around +4 days, it is clear that the GP slightly over-predicts the value of the flux at all wavelengths. As θ_n encapsulates wavelength-independent calibration errors and noise, it is clear why this SN would have a higher than average θ_n.

The final example is SNF20080514-002, shown in Figure A.7; it is fairly representative of the hyperparameter space. It is one of our most well-measured SNe, as is clear from the density of data. The time length scale θ_t is on the smaller end of the distribution, which is not surprising based on how well sampled the data are. Also, θ_n is somewhat larger than the average because the data around +10 days is slightly under-predicted on the whole by the GP.

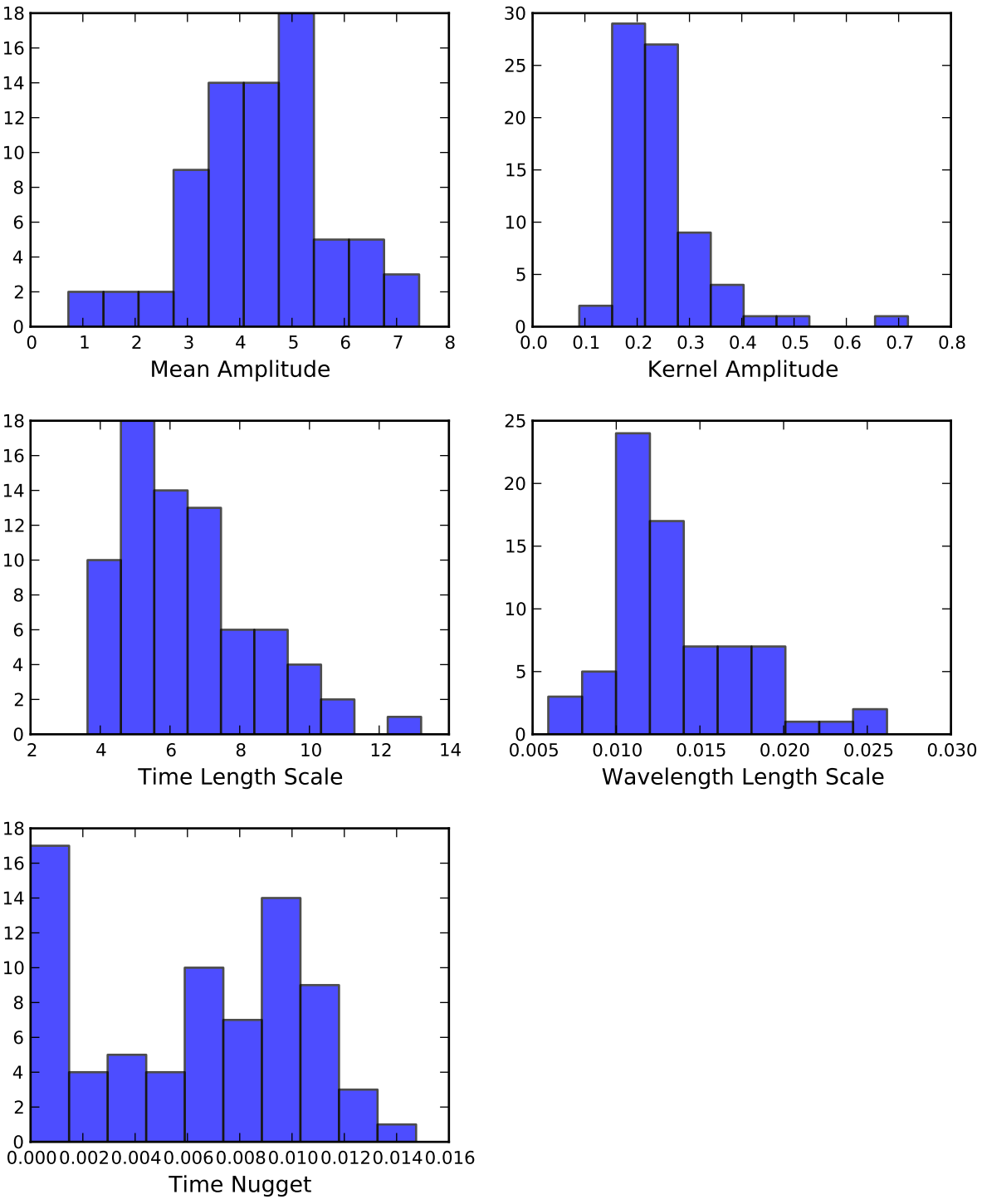

Figure A.3 Histograms of the various hyperparameters for the 74 SNe in the final sample. Top left to bottom left are: Mean Amplitude: θ_a, Kernel Amplitude: θ_s, Time Length Scale: θ_t, Wavelength Length Scale: θ_λ, and Time Nugget: θ_n

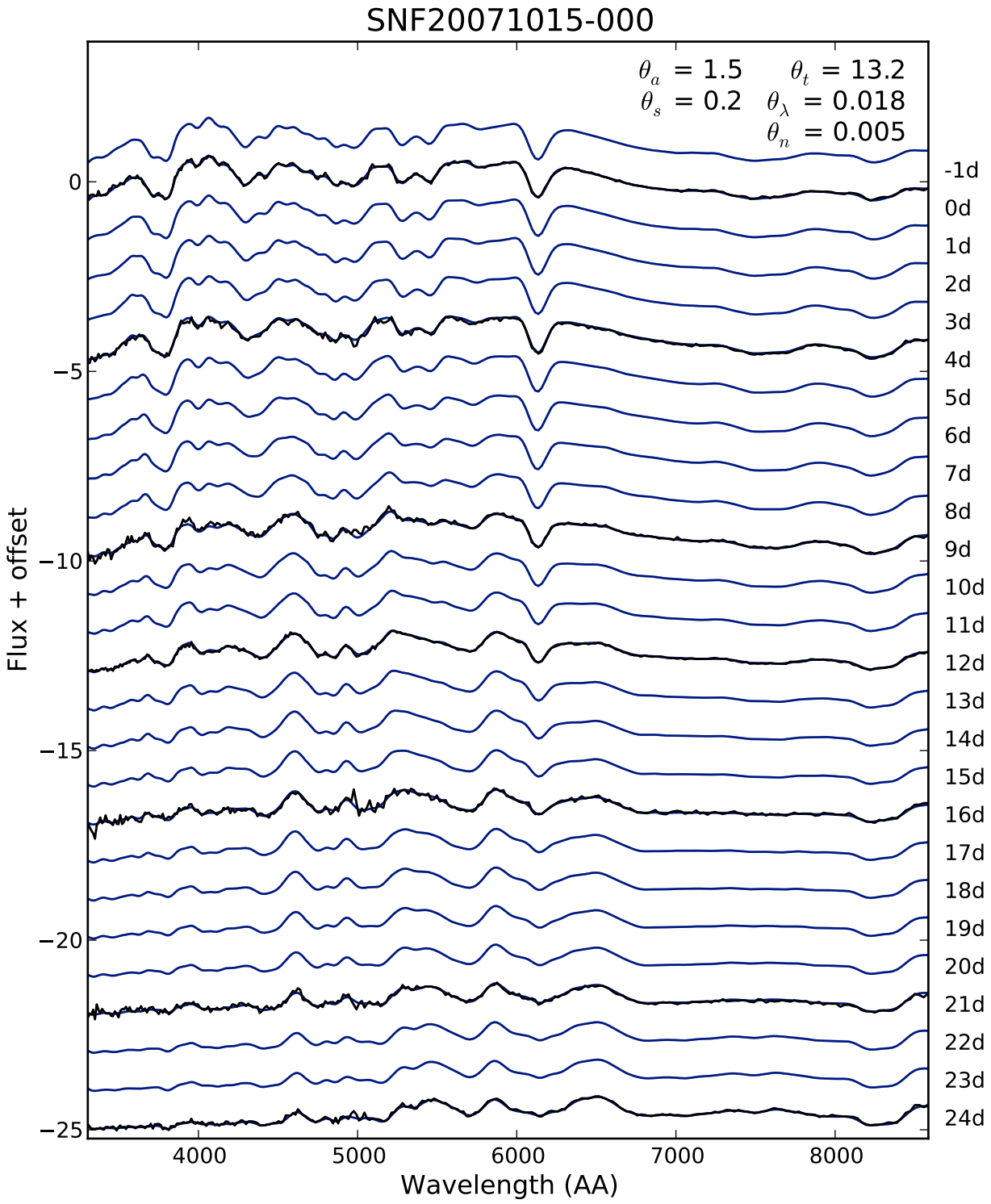

Figure A.4 Gaussian process predictions for SNF20071015-000 in day intervals (days with respect to maximum light, determined from the SALT2 fits to the data) is shown in blue; in black are the data over-plotted on the day interval closest to the phase of the data. Optimized hyperparameters are displayed in the upper right corner of the figure.

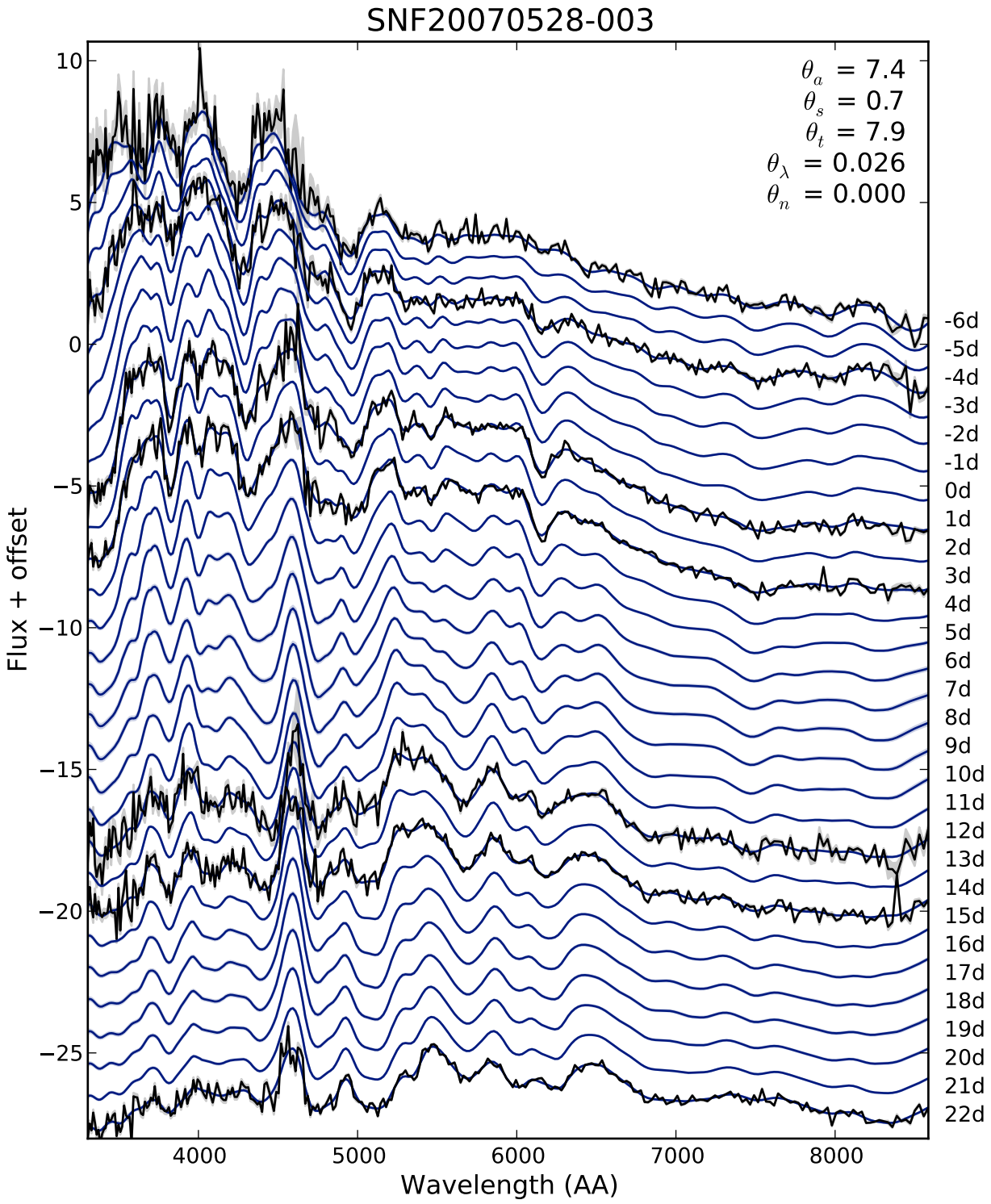

Figure A.5 Gaussian process predictions for SNF20070528-003 in day intervals (days with respect to maximum light, determined from the SALT2 fits to the data) is shown in blue; in black are the data over-plotted on the day interval closest to the phase of the data. Optimized hyperparameters are displayed in the upper right corner of the figure.

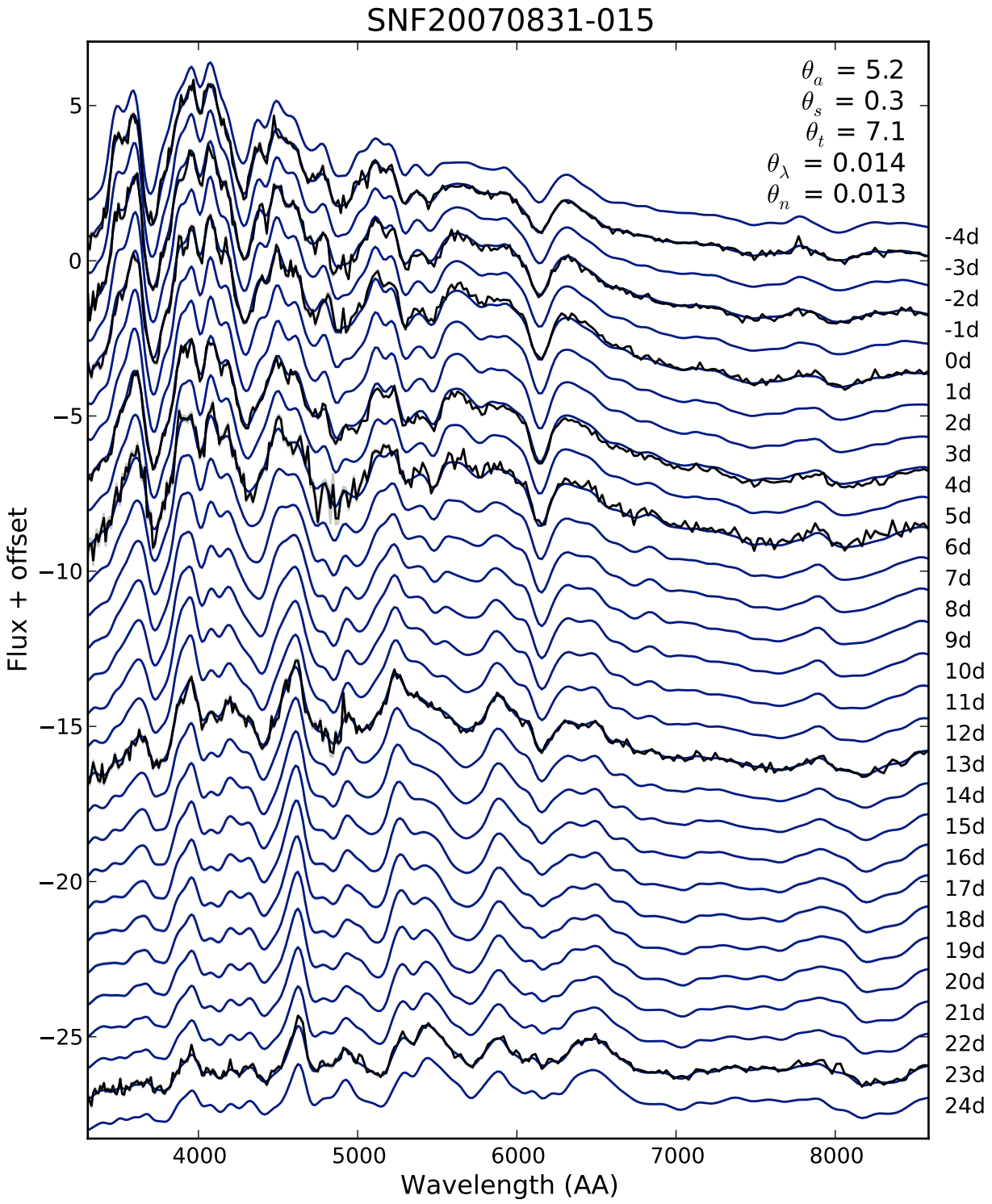

Figure A.6 Gaussian process predictions for SNF20070831-015 in day intervals (days with respect to maximum light, determined from the SALT2 fits to the data) is shown in blue; in black are the data over-plotted on the day interval closest to the phase of the data. Optimized hyperparameters are displayed in the upper right corner of the figure.

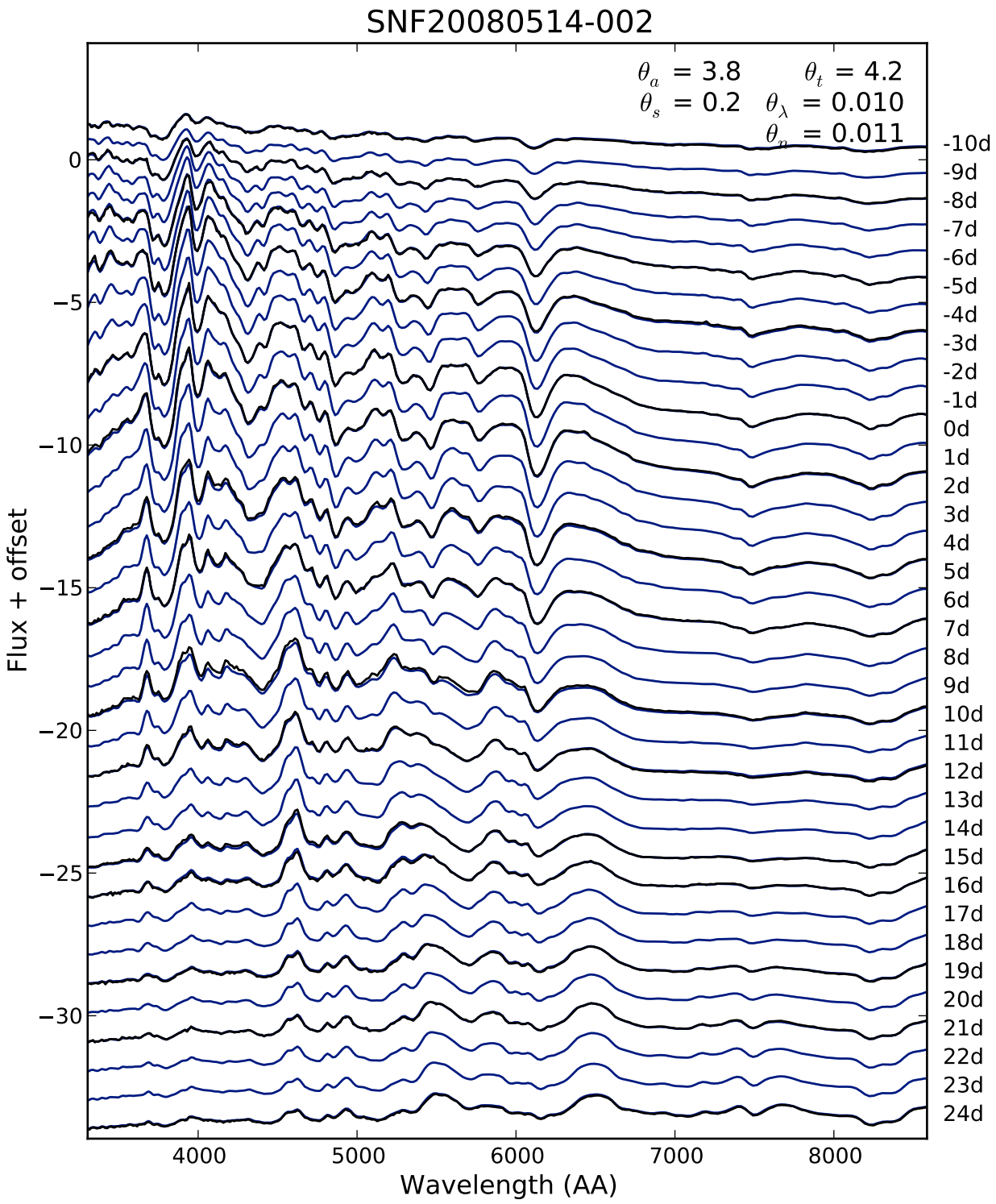

Figure A.7 Gaussian process predictions for SNF20080514-002 in day intervals (days with respect to maximum light, determined from the SALT2 fits to the data) is shown in blue; in black are the data over-plotted on the day interval closest to the phase of the data. Optimized hyperparameters are displayed in the upper right corner of the figure.

Appendix B

Spectroscopy from the Supernova Legacy Survey

B.1 Introduction

For our studies of whether data from a current high-redshift survey were to produce a low dispersion in the twins method of Chapter 4, we turn to the Supernova Legacy Survey (SNLS). The SNLS is one of many recent surveys [Wood-Vasey et al., 2007, Hicken et al., 2009b, Kessler et al., 2009, Suzuki et al., 2011] that constrain the dark energy equation-of-state parameter to an accuracy of 5%, excluding systematic errors. Over the five years the survey ran, SNLS obtained 500 well observed SNe Ia in the redshift interval z=0.2-1.1 [Astier et al., 2006, Guy et al., 2010]. We use the subset of SNLS candidates observed at the Keck telescope as a standard example of a high-redshift data set.

The SNLS uses imaging data from the Canada-France-Hawaii Telescope Legacy Survey (CFHTLS) for supernova discoveries and light curves using the "rolling search" technique in which the four deep CFHT legacy survey fields [Astier et al., 2006] (D1,D2,D3,D4) were imaged in four filters ($g'r'i'z'$) every four days during dark and gray time. Spectroscopic follow-up (for determining candidate redshift and supernova type) was done at the Very Large Telescope (VLT), the Gemini telescopes, and the Keck telescopes. For the spectroscopic follow-up of SNLS targets, the VLT and Gemini were used in service/queue mode, while Keck was used during pre-scheduled nights.

In this appendix we present the observations of all 113 candidates that were targeted with Keck using the LRIS and DEIMOS spectrographs at the Keck I and Keck II telescopes. There are a total of 59 SNe Ia and SNe Ia*, of which 36 are part of the SNLS 3-year cosmological results. The SNLS 3-year results (photometric follow-up and cosmological implications) are presented in Guy et al. [2010], Conley et al. [2011], and Sullivan et al. [2011]. Spectra taken at the VLT from the first three years of the SNLS survey are presented in Balland et al. [2009] and the remaining 4th and 5th year spectra are presented in Balland et al. (in prep). Spectra taken at Gemini are presented in Howell et al. [2005], Bronder et al. [2008], and Walker et al. [2011].

B.2 Observations

B.2.1 Search and Selection

The candidates in this sample were discovered during the five year SNLS project. The rolling search technique, employed with the CFHTLS and described in detail in Howell et al. [2005], continually imaged the fields of interest in several filters every few days, providing densely-sampled lightcurves for all transients. As there was insufficient spectroscopic time to follow all the transients, when possible the choice of which objects to prioritize for spectroscopic follow-up was made based on the goodness of fit of the candidate's (usually pre-max) photometry data to SN Ia lightcurves [Sullivan et al., 2006].

Once a candidate made it to spectroscopy status, generally if it was thought to be at high redshift ($z > 0.6$) and time was available it was sent to Gemini-N or Gemini-S, as the nod-and-shuffle mode at these telescopes is helpful for reducing sky line residuals. Lower redshift targets in the SNLS equatorial fields were sent preferentially to the VLT, as it has the shortest setup time. Both of these facilities (Gemini and VLT) were operated in queue

or service mode: requests for observations were sent to the telescope and observed based on priority ratings. The remainder of the spectroscopic candidates were sent to the Keck telescope observing list.

B.2.2 Spectroscopic follow-up

Of the four SNLS fields, denoted D1–4, D3 is a far northern field and thus not accessible by VLT or Gemini-S. For this reason we initially focused our Keck observations during the period March–June when D3 was visible. Observing runs with Keck usually consisted of individual nights spread out with a spacing of roughly one per month in order to improve the chance for targeting SNLS candidates near their maximum brightness. At the mean redshift of $z \sim 0.6$ of SNLS SNe Ia, this ostensibly allowed spectroscopy of fresh candiates within ± 10 days of maximum light. SNLS candidates known to have later epoch, or which were less secure, were also included if there was a shortfall of premium candidates. Thus, it was expected that the number of candidates confirmed as SNe Ia would be lower than what was achieved with the VLT and Gemini. When poor weather at CFHT or other factors led to a shortfall of suitable SNLS candidates, or when conditions at Keck were poor, observations of other transients were pursued, resulting in several high-impact discoveries [Foley et al., 2006, Aldering et al., 2006, Quimby et al., 2007, Gal-Yam et al., 2007, Barbary et al., 2009].

Candidates were observed from May 2003 to April 2008 with the LRIS and DEIMOS spectrographs. The Low Resolution Imaging Spectrometer (LRIS) [Oke et al., 1995], at Keck I, operates in the visible wavelength range. It employs a dichroic beamsplitter to separate the light into red and blue channels. At the time of our observations, the red camera used a 2048x2048 Tektronix CCD detector, with a pixel scale of $0.215''$/pixel. The blue camera uses a mosaic of two 2Kx4K Marconi CCDs, with pixel scale $0.135''$/pixel [Steidel et al., 2003]. The DEep Imaging Multi-Object Spectrograph (DEIMOS) [Faber et al., 2003], at Keck II, also operates in the visible wavelength range. DEIMOS offers a variety of gratings and has a large focal plane array consisting of a 2x4 mosaic of 2Kx4K MIT/Lincoln Laboratory CCDs. The pixel scale for DEIMOS is $0.1185''$/pixel.

The choice between DEIMOS and LRIS depended on several factors whose relative weighting changed as the program progressed. During the early days of the SNLS survey the DEEP2 program [Davis et al., 2003] was using its large allocation of nights in part to obtain deep multi-object spectroscopy of galaxies in the Extended Groth Strip, which has considerable overlap with the SNLS D3 field. This offered the possibility of obtaining spectra for SNLS targets in parallel with DEEP2 observations by adding existing SNLS candidates to masks for DEEP2 fields that were about to be observed. As the DEEP2 program had extended dark runs, this arrangement also provided better insurance against bad weather. As masks must be made in advance, this program required tight coordination between DEEP2, SNLS and Keck. Altogether, spectroscopy of 10 targets — approximately 20% of all D3 spectroscopy targets prior to June 2004 — were obtained from this cooperative arrangement.

Additionally, in spring 2004 we designed a long slit mask having a reflective Alumiclad coating for DEIMOS. This allowed acquisition of single targets using the slit-viewing camera. Thus, with DEIMOS it became possible to observe single targets in long-slit mode as well as multi-object spectroscopy (MOS) masks. In the end, the broader wavelength coverage

provided by the simultaneous blue and red channels, along with overall higher throughput and more sensitive long-slit acquisition system, led to a general preference for LRIS, which was employed on 14 of our 19 nights. However, as the program neared its end we returned to MOS masks on DEIMOS for two nights to obtain spectroscopy of the host galaxies of SNLS SNe from previous years in parallel with observations of active SNLS candidates.

For data taken with LRIS, the standard wavelength coverage for our observations is from 3500 Å to 9200 Å; for data taken with DEIMOS, the coverage is from 5300 Å to 9800 Å. Observations of each candidate typically consisted of 2-4 exposures of varying duration (between 1200 and 1800 s), depending on the brightness of the object. Observational details, including setup and conditions, for each candidate are given in Tables B.1 to B.3. For observations with DEIMOS, the grating used is listed in the table; for LRIS observations, the dichroic and grism are listed as well. During LRIS observations the red side grating tilt was adjusted to achieve continuous wavelength coverage; however, there were two nights (2005 March 16 and 2005 April 11) for which this was not done and there is a gap in wavelength coverage. 12 candidates are affected by this; nine are SNe Ia/Ia* and three are of unidentified type (CI=2), providing a 75% success rate — surprisingly, better than the mean for our sample.

The majority of our candidates were observed in long slit mode. Whenever possible, the slit angle was chosen to include the presumed host galaxy of the candidate, as the most accurate redshift determination comes from narrow galactic features. Since this position angle rarely coincided with the parallactic angle, the resulting spectra are not expected to be spectrophotometric. For long slit observations, flux calibration standard stars were observed at the parallactic angle over a range in airmass. In the case of LRIS, the slit width was chosen to match the projected seeing for the night. The DEIMOS long slit was available with a width of $0''.7$ only. The slits for MOS were $1''$.

In total we were awarded 25 nights from May 2003 to April 2008. Our first night in May 2003 was used for SNLS commissioning support and to observe DEEP2 masks, initiating our collaboration with the DEEP2 team. The following three awarded nights (May 2003, July 2003, March 2004) were joint with the DEEP2 team and we observed some SNLS targets in long slit mode, some SNLS targets on DEEP2 masks, and some DEEP2 masks without SNLS targets. Three nights were entirely lost due to weather (two in March 2006, and one in August 2007) and three additional nights (March 2004, February 2007, December 2007) suffered from poor weather and we were unable to observe many targets. All told, of our 25 nights, Tables B.1 to B.3 lists 19 nights with observed targets.

B.3 Data Reduction

B.3.1 DEIMOS Pipeline

For reducing DEIMOS data, we use the UCB DEEP2 pipeline[1]: an IDL-based package (based on the SDSS spectral code of D. Schlegel), which produces cosmic-ray cleaned, sky-subtracted 2-D and 1-D extracted spectra. The pipeline properly accounts for tilted sky lines resulting from tilted slits, yielding sky subtraction residuals near the Poisson level.

[1] `http://astro.berkeley.edu/~cooper/deep/spec2d/`

The first stage in the reduction is the processing of flat and arc files, chip by chip to produce the necessary calibration files. Multiple flats, taken before and after science observations, are processed to determine the location of the slitlets on the CCD array, reject cosmic rays, and to measure the throughput of the slitlet. Arc files are used to determine the 2-D wavelength solution for each slitlet, with a mean RMS scatter of 0.25Å.

The science frames are also reduced chip by chip to extract science data, using the calibration files to flatfield and rectify each slitlet. The b-spline used for the construction of the sky model is a description of the mean sky as a function of wavelength and includes cosmic ray rejection. To complete sky-subtraction, the b-spline sky model appropriate for each exposure is subtracted from the individual extracted science slitlets. To combine the separate science exposures, an inverse variance weighted average is computed, pixel by pixel. Cosmic ray rejection is applied at this stage based on the variability of a given pixel.

1-D spectra and error spectra are obtained for each object (the supernova candidate as well as occasionally the candidate host) on each of the slitlets using an unweighted rectangular aperture (i.e. a boxcar) for extraction. To complete the reduction process, the 1-D spectra are flux calibrated and corrected for telluric features using observations of CALSPEC standard stars; an atmospheric extinction correction is also applied, derived from the effective airmass of the observation.

B.3.2 LRIS Pipeline

For reducing LRIS data, we use the Low-Redux pipeline[2]: a package for reducing longslit data from several different optical spectrometers including LRIS. Flat fielding in this pipeline is split in two for improved sky subtraction: pixel flats represent the intrinsic pixel-to-pixel variations in CCD response, illumination flats represent the larger scale variations due to non-uniformities in the slit width and vignetting. After this split flat-fielding proceeds as with the DEIMOS pipeline. Arc exposures taken for wavelength calibration are processed to yield a wavelength solution with mean RMS scatter of 0.27Å and 0.62Åfor the red and blue channels respectively.

The science frames are then reduced, red and blue channels separately, using the flat fields and wavelength solution. The sky is modeled by a b-spline function along the spatial direction, excluding the science object pixels from the fit. Individual science exposures are sky-subtracted using this b-spline model.

Final extraction is completed for the red and blue channels independently, producing 1-D spectra and error spectra for all objects. Extraction is completed with the boxcar method, where the box size is matched to the seeing. At this stage the red and blue sides of the spectra are flux calibrated, telluric corrected, and extinction corrected before being coadded and cosmic ray cleaned to produce final spectra.

B.4 Candidate Classification

For determining redshifts, when possible we obtain the redshift from narrow features in the underlying or accompanying host spectrum. At high redshifts host contamination is

[2] `http://www.ucolick.org/~xavier/LowRedux/`

generally unavoidable due to the small angular size of the galaxy. To identify the host lines, we use four galaxy principle component templates from a collection of SDSS spectra [Agol et al., 2011], each template with different emission and absorption lines. The templates are fitted to the spectrum, together with a third order polynomial which accounts for any slowly varying mis-calibration, to produce a χ^2 per degree of freedom distribution as a function of redshift. The synthetic fluxes corresponding to the minima of the fit are compared to the data spectrum by eye to ensure that the emission and absorption lines of the synthetic flux correspond to legitimate emission and absorption in the data (and not to stray cosmic rays or sky subtraction residuals). [OII] $\lambda\lambda$ 3726, 3729, [OIII] $\lambda\lambda$ 4959, 5007, CaH, CaK, and Hβ are the most commonly detected features, as well as occasionally Hα and [NII] λ 6584. When the redshift is determined from narrow host galaxy features we assign an error of 0.001 unless otherwise noted.

When no host lines are detected we must rely on the supernova fitting algorithm for the redshift; this method is less accurate, yielding a redshift error of 0.01. For supernova fitting, we use Superfit [Howell et al., 2005], which is a χ^2 fitter designed to separate supernova from host galaxy light and to obtain the supernova type through comparison to a library of supernova observations over a range of epochs and types. Unless the redshift is supplied from lines in the host galaxy spectrum, it is varied in the fit, along with the host contamination and the reddening (using the reddening law of Cardelli et al. [1989] with $R_v = 3.1$). The supernova library consists of 184 SN Ia, 75 SN Ib/c, and 47 SN II. The fit result, consisting of best matching SN templates, host galaxy templates, redshift (if not set by the host lines), and reddening, must be inspected visually for final classification. The epoch of the supernova is determined from the mean of the epochs of the five best fit templates.

For final classification we adopt the Confidence Index (CI) fully described in Howell et al. [2005]. SNe of CI=5 are certain SNe Ia: the distinctive SiII or SII are present; at redshifts observed in this sample, the SiII 6150Å and SII 5400Å lines are shifted toward redder wavelengths where sky line residuals can obscure supernova flux, so often SiII 4000Å(in combination with the flux decrease blueward toward the CaII H&K feature) is used as the key indicator. CI=4 are highly probably SNe Ia: the spectrum matches SN Ia template spectra and does not match other SN type template spectra, but lacks the definitive lines; for the redshifts probed in this sample, the UV features, particularly CaII H&K, and the MgII triplet are the most commonly identified lines. SNe of CI=3 are probable SNe Ia: the spectrum, although well-matched to a SN Ia template lacks definitive line identification and could also match other SN templates (generally SN Ib or Ic); this classification is noted as SN Ia* in other schemes. CI=2 is applied when the type cannot be determined, usually due to low S/N or severe host contamination. Candidates that are probably not SNe Ia are given a CI=1: the candidate spectrum is not consistent with SN Ia templates but the type cannot be confirmed unambiguously. CI=0 is for candidates that are definitely not SNe Ia: the spectrum matches that of another type (SN Ib/c, SN II, or AGN) or is inconsistent with being a SN Ia.

B.5 Classification Results

The SNLS 3-year sample has been published in Guy et al. [2010]. Here we present spectra observed at Keck that will become part of the 5-year SNLS sample. For those of our spectra in the 3-year sample, for which we have photometric data, we have included light curve epoch information for comparison with the spectral fit epoch information. None of the objects in this sample are confirmed to be peculiar SNe Ia; however, as it is difficult to identify peculiar SNe unless the signal-to-noise ratio is high, we cannot rule out that some of these objects may be peculiar.

Tables B.4 and B.5 list the classification of each object and when possible, redshift, best fit supernova template, and spectroscopically-derived epoch relative to maximum light (τ_{spec}). SNe Ia discovered from 2003 to 2006 are included in the SNLS 3-year sample and for these objects we have finalized photometry and light curve fits from which we can derive τ_{LC}, the epoch of the spectrum relative to B-band maximum light; when available this is listed in the Table. Figures B.1-B.10 show observed data in gray for all classified objects (i.e. CI$\neq$2). If the redshift has been determined from narrow emission or absorption from the host galaxy, those lines are marked, otherwise the redshift has been determined from fits to supernova templates.

We also show supernova template fits to the candidates that are classified SNe Ia/Ia* and non-SNe Ia. In these figures, unless otherwise noted, a host galaxy template has been subtracted from the object flux. The amount and type of host galaxy template to subtract is determined by Superfit as a part of the joint supernova and galaxy template fitting proceedure. The template-host subtracted flux has been rebinned to 20 Å for visualization purposes, though narrow galaxy emission lines have not been removed prior to rebinning. Figures B.1-B.5 show the template host-subtracted spectra, and the best-fit template object for secure SNe Ia (candidates with CI=4 and CI=5). SNe Ia* (candidates with CI=3) are shown in Figures B.6-B.8 and non-SNe Ia candidates (CI=0-CI=1) are shown in Figures B.9-B.11. As mentioned in Section B.2.2, some candidates lack continuous wavelength coverage.

B.6 Discussion

Redshifts were determined for 99 of the 113 candidates, a success rate of 88%. Of the 14 candidates for which no redshift could be determined, the presumed host of the object was either very faint or not apparent. Figure B.12 is a histogram of the number of candidates of each different classification level as a function of redshift. SNe of CI=4 and CI=5 are grouped together as "SN Ia" and objects of CI=0 and CI=1 are grouped together as "Non-Ia." "No ID" refers to objects of CI=2 and "SN Ia*" are less secure SNe Ia of CI=3. At higher redshifts, the fraction of the less certain SN Ia* type over the secure SN Ia type increases, as would be expected from the decreased S/N available at higher redshift. Most non-SN Ia objects are at lower redshift, as core collapse SNe are generally intrinsically fainter phenomena; note that the single non-SN Ia object in the highest redshift bin is 07D3ar, an AGN. The mean redshift of the combined SN Ia and SN Ia* sample is $\bar{z}_{Keck} = 0.61$, which is comparable to the redshift distributions presented in Walker et al. [2011] for observations

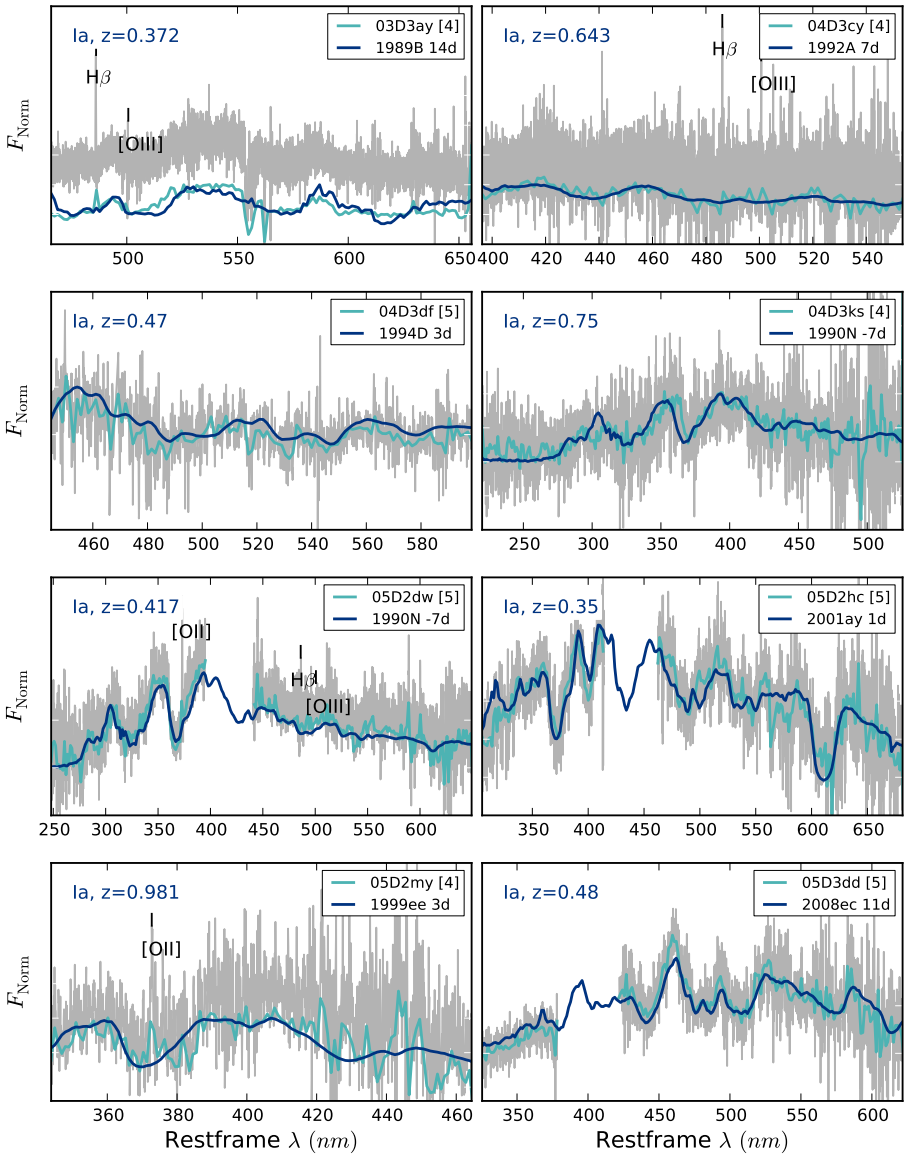

Figure B.1 Candidates with CI=4 or CI=5 (secure SN Ia). Observed data is shown in gray with host galaxy emission or absorption lines marked. Supernovva+host minus template galaxy is shown in light blue, best fit supernova template shown in dark blue. The spectra have been deredshifted into the restframe and the fluxes are normalized to unity. Confidence Index CI is shown in the legend adjacent to the supernova name.

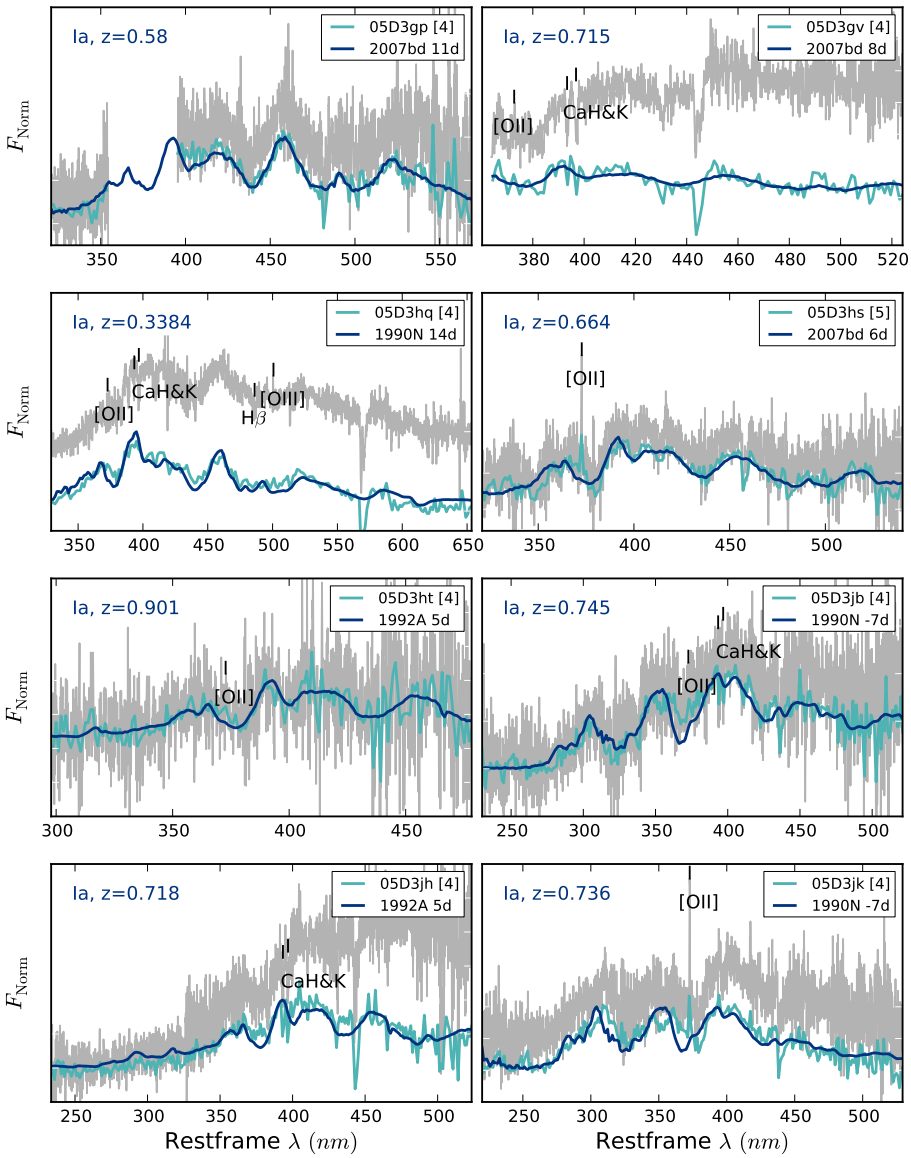

Figure B.2 Continued from Figure B.1.

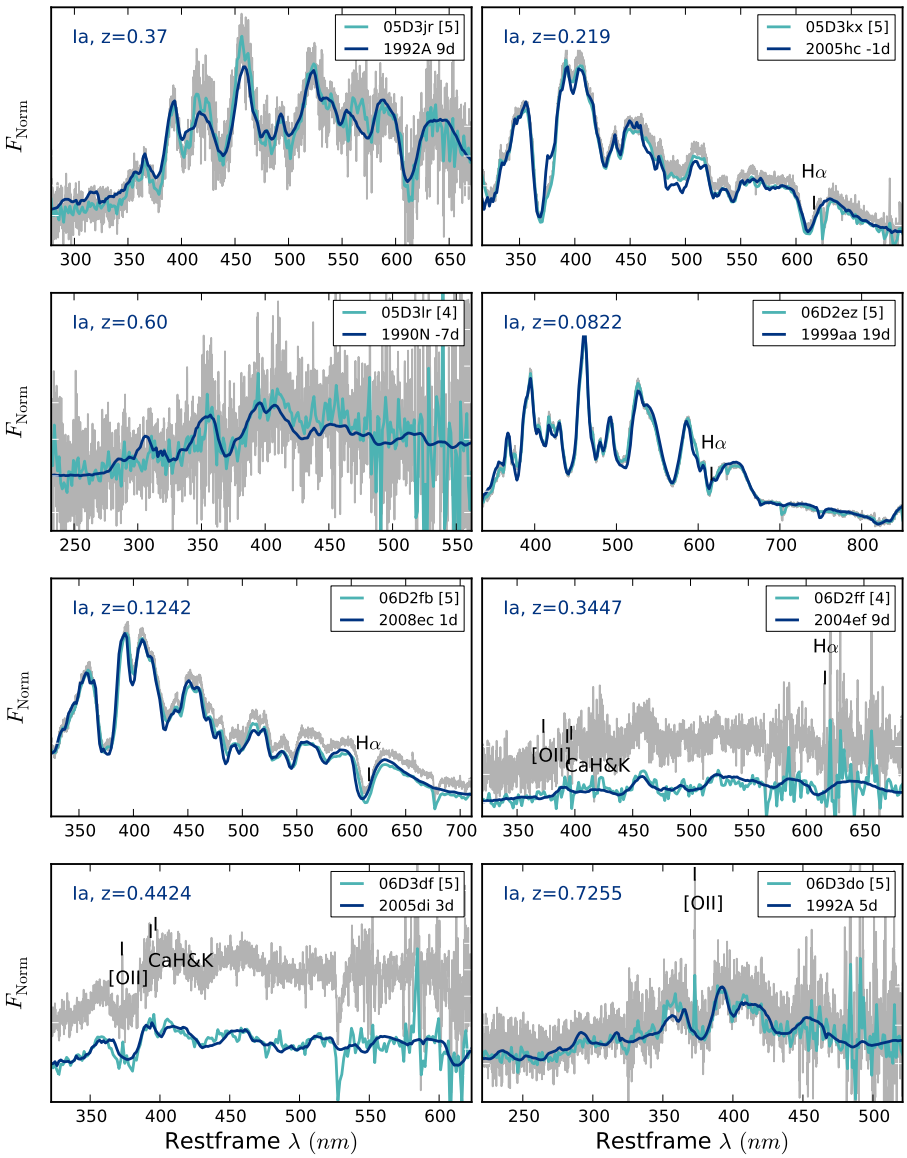

Figure B.3 Continued from Figure B.1.

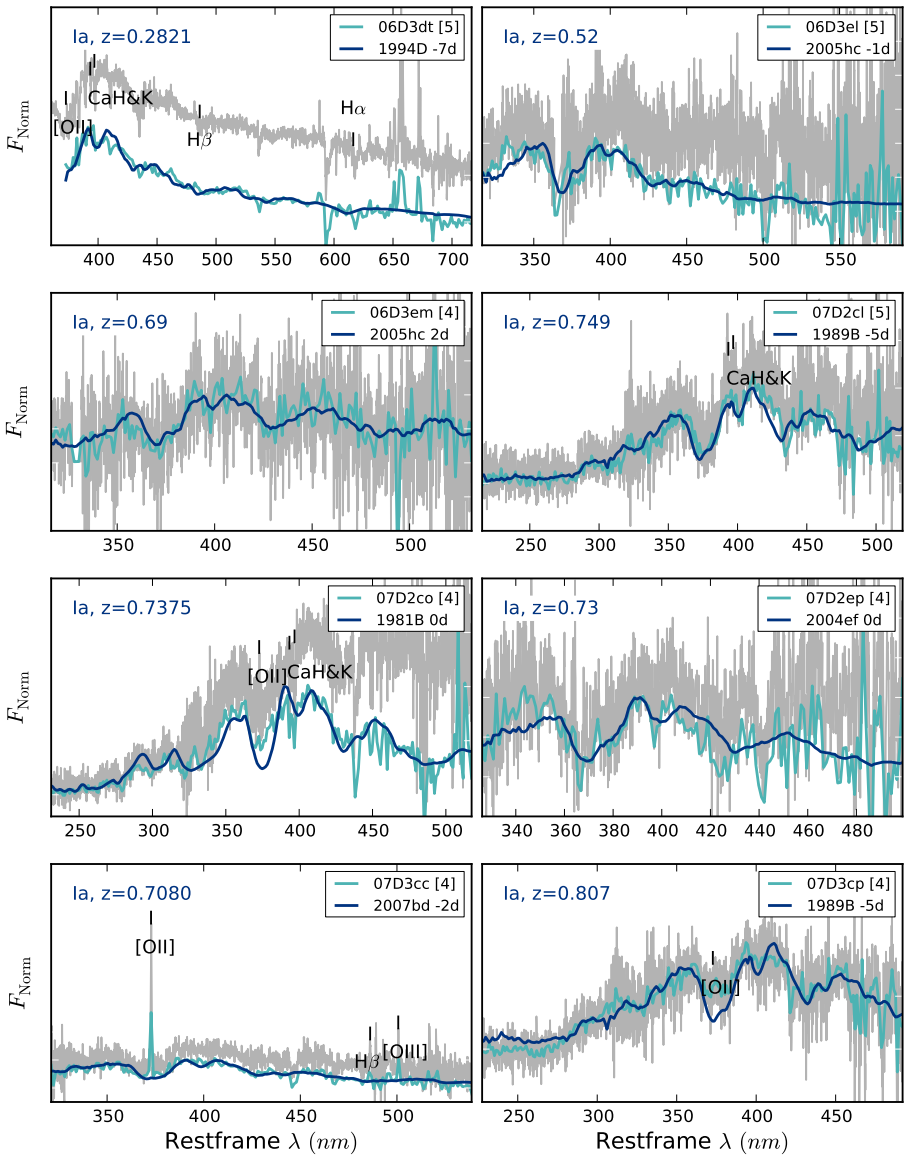

Figure B.4 Continued from Figure B.1.

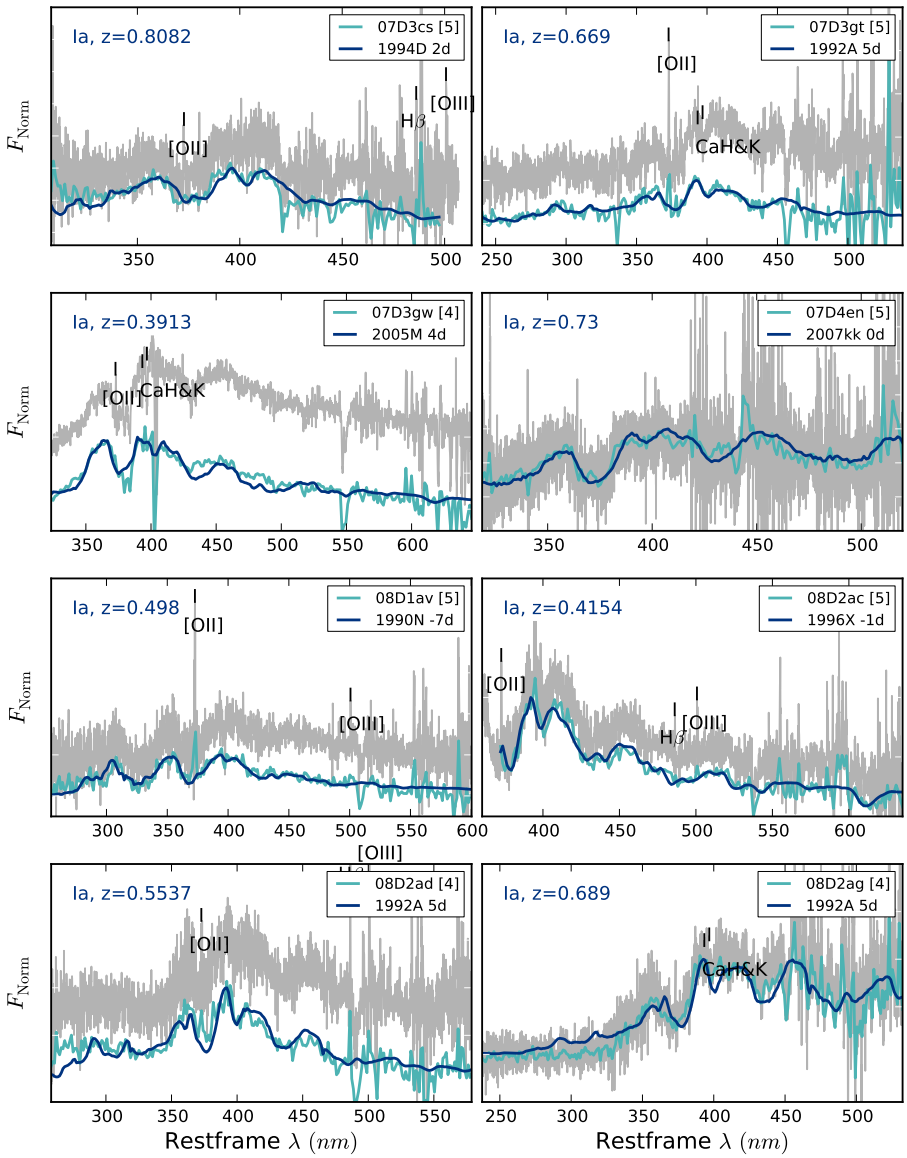

Figure B.5 Continued from Figure B.1.

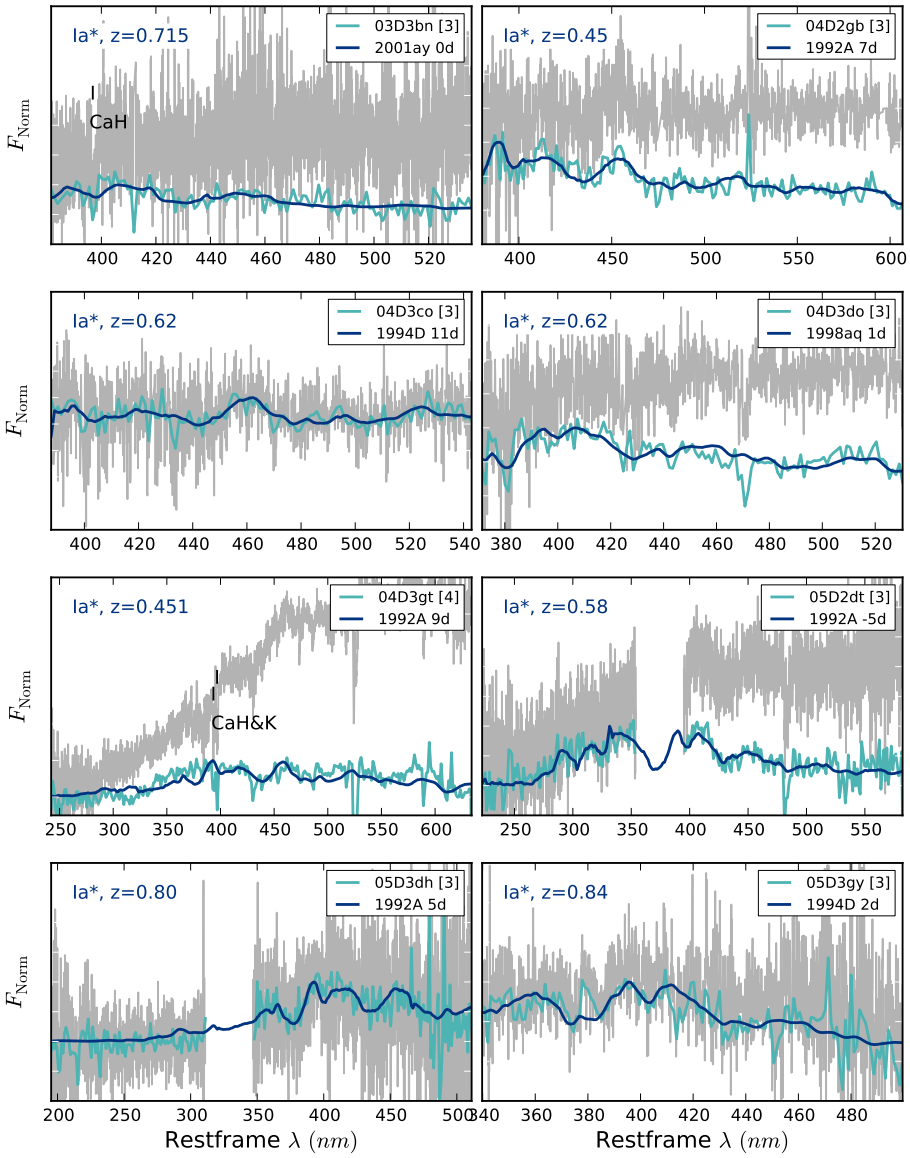

Figure B.6 Candidates with CI=3 (likely SNe Ia). Observed data is shown in gray with host galaxy emission or absorption lines marked. Supernova+host minus template galaxy is shown in light blue, best fit supernova template shown in dark blue. The spectra have been deredshifted into the restframe and the fluxes are normalized to unity. Confidence Index CI is shown in the legend adjacent to the supernova name.

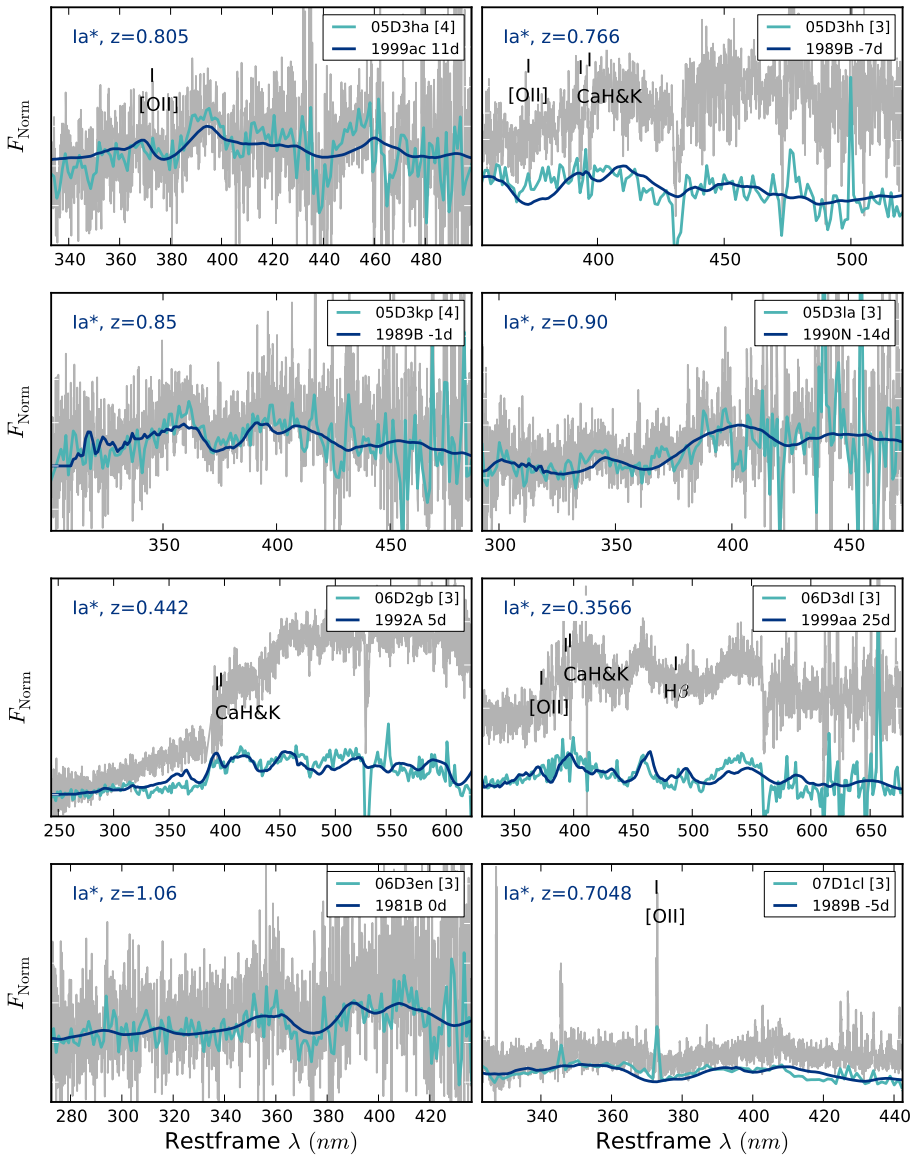

Figure B.7 Continued from Figure B.6.

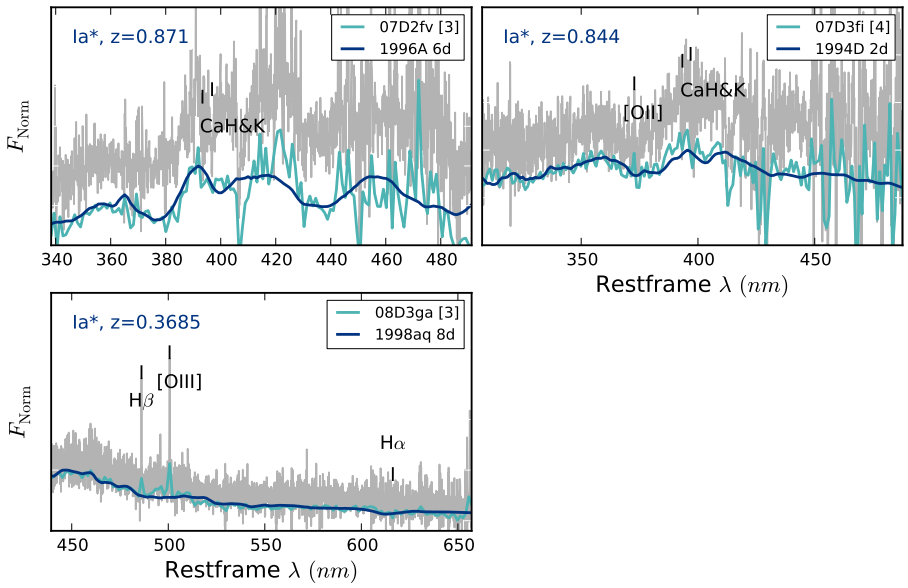

Figure B.8 Continued from Figure B.6.

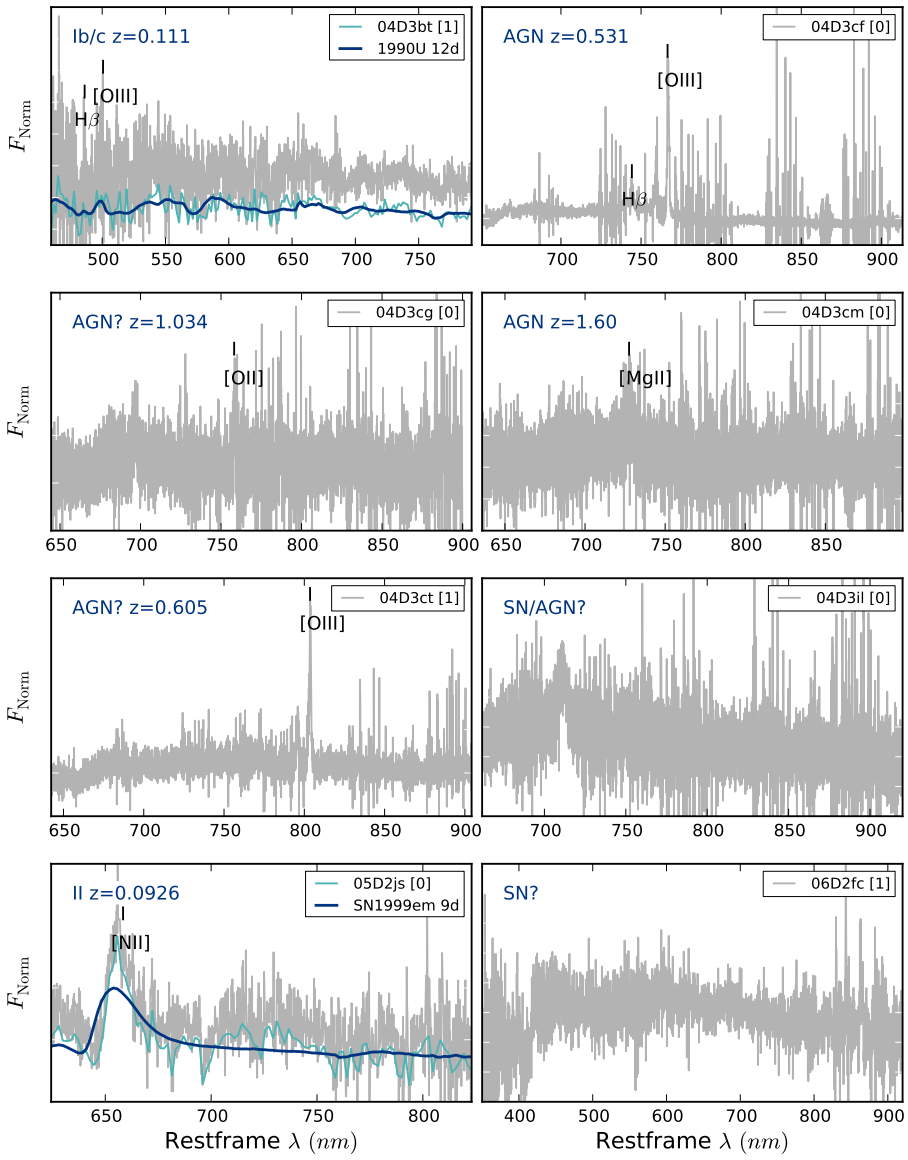

Figure B.9 Candidates with CI=0 or CI=1 (non-SN Ia). Observed data is shown in gray with host galaxy emission or absorption lines marked. Supernova+host minus template galaxy is shown in light blue, best fit supernova template (if available) shown in dark blue. If a template is fit to the data, the spectra have been deredshifted into the restframe. In all cases the fluxes are normalized to unity. Confidence Index CI is shown in the legend adjacent to the supernova name; upper left corner of each panel shows the type: Ib/c, II, AGN.

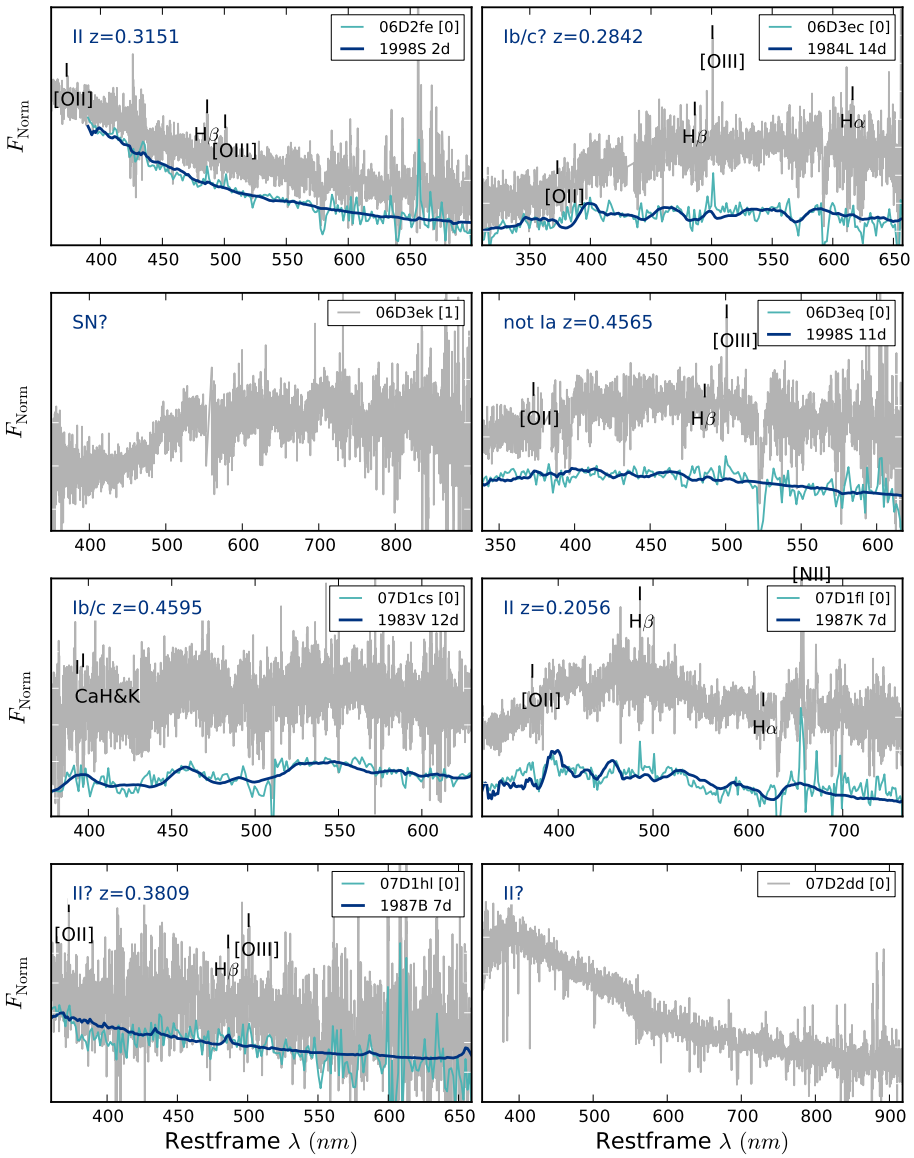

Figure B.10 Continued from Figure B.9.

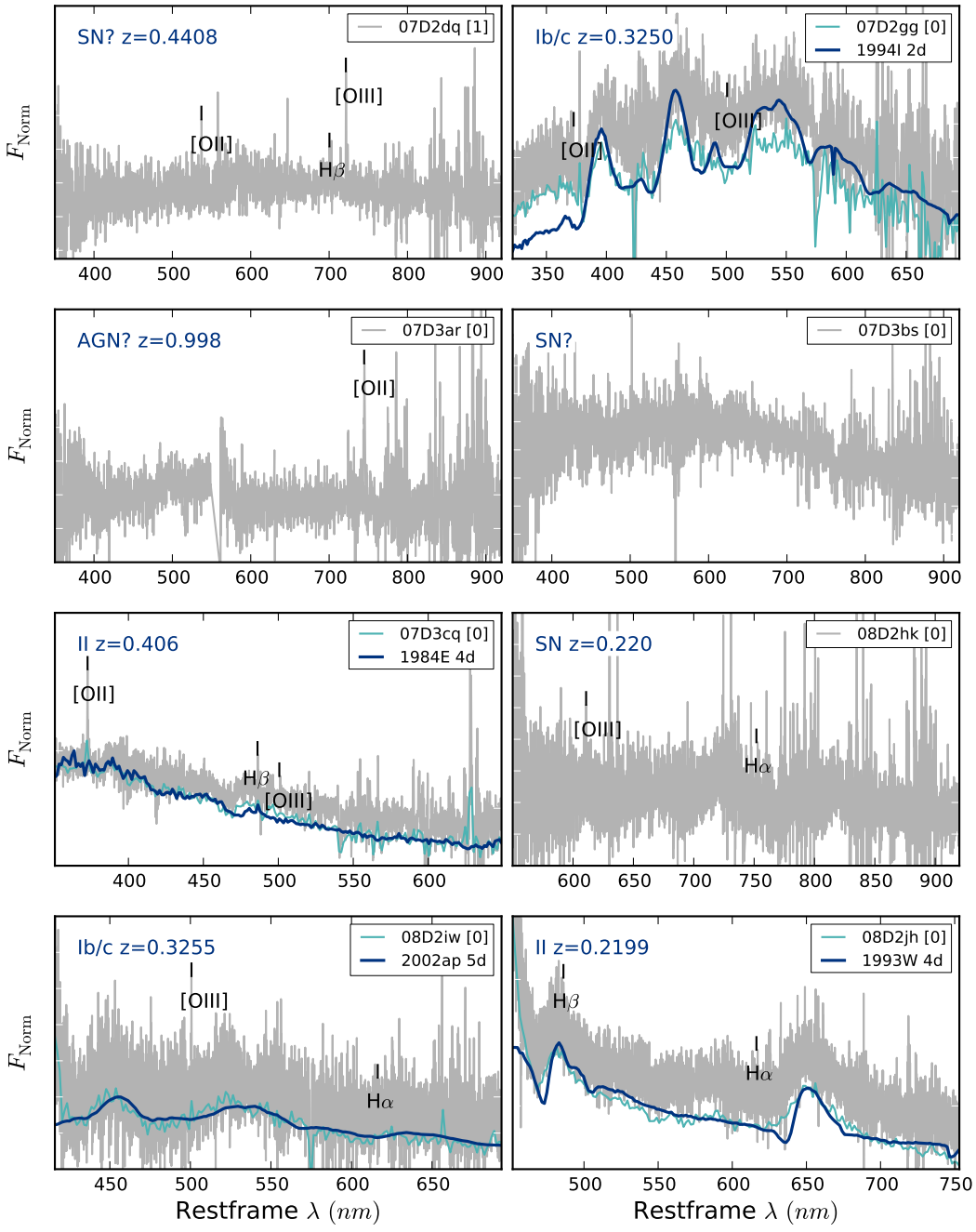

Figure B.11 Continued from Figure B.9.

done at Gemini ($\bar{z}_{Gem} = 0.63$) and in Balland et al. [2009] for observations done at the VLT ($\bar{z}_{VLT} = 0.63$).

For those SNe Ia/Ia* in the SNLS 3-year sample (36 objects), we can compare the epoch determined from fits to the spectra (τ_{Spec} in Tables B.4) and B.5 to the epoch determined from fits to the light curves (τ_{LC} in Tables B.4 and B.5). Figure B.13 shows this comparison; it is apparent that the epoch estimation from fits to the spectra are poor at early (before -10 days) and late (after ∼+12 days) times. The RMS of the whole sample is 3.9 days, higher than the values found in Howell et al. [2005] and Hook et al. [2005] (2.5 and 3.3 days, respectively). However, if we look only at the epochs probed by those two analyses (-10 days to +10 days and -7.5 days to +15 days), the RMS of our sample is 3.0 days (in both cases), consistent with previous results. This inability to determine the epoch of early time spectra was also seen in Howell et al. [2005] and is due to the limited number of early time spectra. The difficulty at later time stems from the increased similarity of spectra at later times coupled with the library of spectra having more templates around ∼+7 days than ∼+15 days.

Thus in order to do an accurate comparison of the epoch coverage of this sample with other spectroscopic samples such as Howell et al. [2005], we must correct the spectroscopically determined epochs for the systematic underestimation at early and late times. The dashed line in Figure B.13 is a fit to τ_{spec} as a function of τ_{LC}. The shallow slope arises from the paucity of early and late time spectra coupled with the increased number of templates between -5d and +10d. By inverting this relation we can convert a spectroscopically determined epoch to an estimate of the light curve determined epoch. Figure B.14 shows the epoch of each spectrum's observation; for objects in the SNLS 3-year sample, τ_{LC} is used, while for objects without final photometry, τ_{spec} is corrected using this relation. Neglecting the two outlying objects at epochs greater than ∼30 days, the bulk of the sample is between -15 and +20 days, a larger range than the -10 to +10 days found in Howell et al. [2005]. This range is similar to what was found in Balland et al. [2009], but here the distribution is flatter, with more objects at early and late times, which is consistent with the expectation that when observations are done in classical observer mode, a wider range of targets are selected for follow-up.

The repercussions of classical mode observing are also evident in the fraction of candidates that were able to be classified as SN Ia/Ia* or non-SN Ia. In Howell et al. [2005] such a classification was determined for ∼80% of the observed candidates, whereas in this sample only ∼73 % are classified as SN Ia/Ia* or non-SN Ia. The percentages of spectroscopically determined SN Ia/Ia* for all SNLS candidates observed at the Gemini telescopes [Howell et al., 2005, Bronder et al., 2008, Walker et al., 2011] vs this sample are 71% vs 52 %. This is largely because a broader range of transients (generally fainter and more contaminated by host galaxy) were observed with Keck, than were sent to the VLT and Gemini.

In this appendix we have presented spectroscopic observations of 113 candidates from the SNLS survey. We present spectra of the 83 objects, 59 of which are classified as SNe Ia/Ia* in the redshift range $z = 0.082$ to $z = 1.06$; the other 24 objects are classified as non-SNe Ia. The epochs of these SNe Ia spectra range from ∼-15 days to +20 days relative to B-band maximum light. We see fair agreement between the epoch determined from fitting the spectra with a library of template spectra and the epoch determined from fits to the light curves. Spectra presented here span the complete 5-year range of observations with the

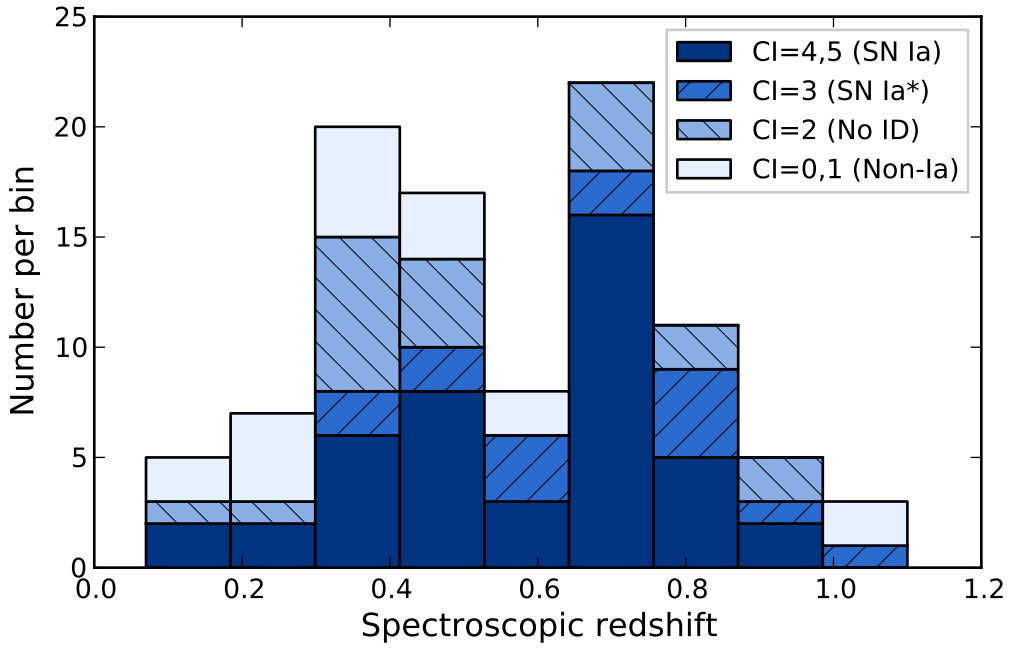

Figure B.12 Histogram of the redshifts of the 99 candidates for which we could measure a redshift.

SNLS.

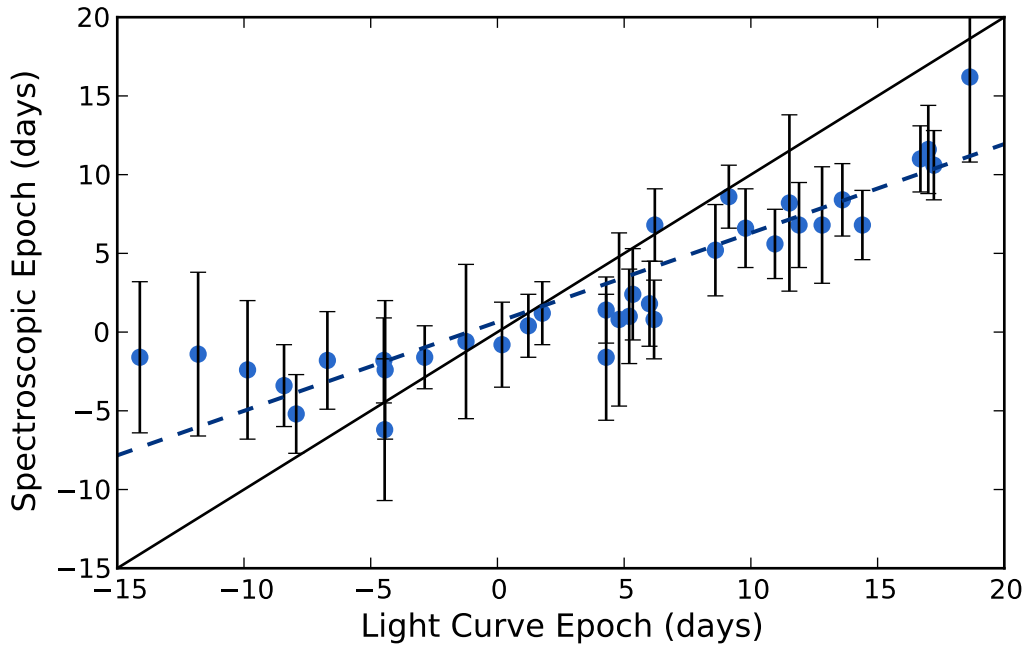

Figure B.13 Rest-frame epoch of spectroscopic observations relative to B-band maximum light from fits to the light curve and fits to the spectra. The light curve epoch is determined from the time of B-band maximum provided in Conley et al. [2011]. The solid line is not a fit to the data, but shows where the SNe would lie if the spectroscopic epoch were equal to the light curve epoch. The dashed blue line is a fit to the data, used for correcting the epochs of SNe Ia lacking light curve determined epochs.

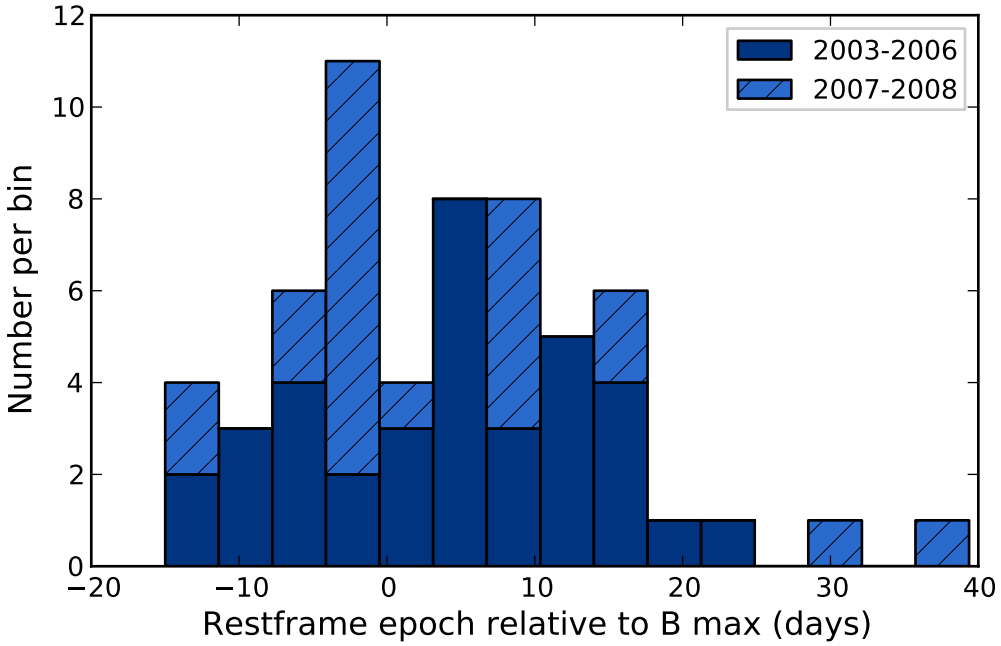

Figure B.14 Histogram of the rest-frame epoch relative to B-band maximum light for SNe Ia/Ia*. Objects discovered between 2003 and 2006 are in the SNLS 3-year sample and have finalied photometry; for these we use the light curve determined epoch. Objects discovered in 2007 and 2008 will have finalized photometry in the full SNLS 5-year sample, so we use the spectroscopically determined epoch corrected by the dashed line fit to the data in Figure B.13.

Table B.1 Summary of SNLS Candidate Observations at Keck: Part I

UT Date	**Telescope**		**Mean Seeing**		**Instrument**	
SN[a]	R.A.	Dec.	Exp (s)	Dichroic	Grating	Grism
2003 May 31	**KECK II**		**0.8″**		**DEIMOS**	
03D3bn	14:20:09.214	+53:02:34.40	710	···	830	···
2003 Jul 2	**KECK II**		**0.8″**		**DEIMOS**	
03D3bz	14:19:16.470	+52:37:49.40	2400	···	830	···
03D3cy	14:17:57.740	+52:57:37.33	4716	···	830	···
03D3dd	14:22:39.940	+52:47:49.51	3700	···	830	···
03D3dr	14:21:54.230	+52:58:50.01	1200	···	830	···
03D3ds	14:21:27.790	+53:06:10.75	7549	···	830	···
2004 Apr 22	**KECK II**		**1.0″**		**DEIMOS**	
04D2gb	10:02:22.712	+01:53:39.16	2400	···	830	···
04D2ii	10:00:29.469	+02:32:18.32	3600	···	830	···
04D3bt	14:16:59.861	+53:07:51.44	719	···	830	···
04D3ch	14:22:27.117	+52:40:03.23	3600	···	830	···
04D3co	14:17:50.024	+52:57:49.05	3600	···	830	···
04D3db	14:21:05.233	+52:53:53.09	2400	···	830	···
04D3df	14:18:10.020	+52:16:40.13	2400	···	830	···
04D3do	14:17:46.107	+52:16:03.55	2400	···	830	···
2004 May 23	**KECK I**		**0.8″**		**LRIS**	
04D3gt	14:22:32.594	+52:38:49.52	2400	560	400/8500	600/4000
04D3ht	14:16:17.101	+52:19:28.40	2400	560	400/8500	600/4000
04D3is	14:16:51.944	+52:48:45.44	3600	560	400/8500	600/4000
04D3jb	14:19:44.651	+52:37:08.00	1600	560	400/8500	600/4000
04D3ki	14:19:34.599	+52:17:32.59	3600	560	400/8500	600/4000
04D3kk	14:21:17.061	+53:04:05.85	2400	560	400/8500	600/4000
04D3kr	14:16:35.937	+52:28:44.20	1200	560	400/8500	600/4000
04D3ks	14:22:33.517	+52:11:06.75	3600	560	400/8500	600/4000
2003 Jun - 2004 May	**KECK II**		**-**[b]		**DEIMOS**	
03D3ay	14:17:58.430	+52:28:57.49	3900	···	12000	···
04D3at	14:16:41.267	+52:22:35.61	4625	···	12000	···
04D3bx	14:16:31.086	+52:20:26.01	5760	···	12000	···
04D3cf	14:16:43.271	+52:14:35.90	11400	···	12000	···
04D3cg	14:16:50.938	+52:15:28.79	3600	···	12000	···
04D3cm	14:16:53.721	+52:21:09.49	3600	···	12000	···
04D3ct	14:16:41.961	+52:31:43.14	8384	···	12000	···
04D3cy	14:18:12.435	+52:39:30.59	7200	···	12000	···
04D3il	14:17:05.757	+52:32:30.84	3600	···	12000	···
04D3qa	14:19:29.787	+52:52:06.61	3600	···	12000	···
2005 Mar 16	**KECK I**		**1.0″**		**LRIS**	
05D2dt	10:01:23.907	+01:51:28.13	4800	560	400/8500	600/4000
05D2du	10:01:28.316	+02:02:26.02	2400	560	400/8500	600/4000
05D2dw	09:58:32.058	+02:01:56.36	3600	560	400/8500	600/4000
05D3ba	14:18:26.790	+52:41:50.56	4200	560	400/8500	600/4000
05D3dh	14:20:50.382	+52:39:45.92	3000	560	400/8500	600/4000

[a]The SNLS naming convention is as follows: *06D3df*: the first two digits are the year of discovery, the second two are the field name, and the final two are *aa* for the first candidate of the year continuing toward *ab* and then on to *ba* for the 27th candidate.

[b]These events were observed on masks by the DEEP2 program and as such were taken on a variety of nights with a variety of seeings.

Table B.2 Summary of SNLS Candidate Observations at Keck: Part II

UT Date	**Telescope**		**Mean Seeing**	**Instrument**		
SN[a]	R.A.	Dec.	Exp (s)	Dichroic	Grating	Grism
2005 Apr 11	**KECK I**		**0.9″**		**LRIS**	
05D2hc	10:00:04.574	+01:53:09.94	2400	560	400/8500	600/4000
05D2if	10:01:58.377	+02:21:11.66	4800	560	400/8500	600/4000
05D3dd	14:22:30.410	+52:36:24.76	2400	560	400/8500	600/4000
05D3gp	14:22:42.338	+52:43:28.71	3600	560	400/8500	600/4000
05D3gv	14:20:59.279	+53:10:43.81	3600	560	400/8500	600/4000
05D3gy	14:16:27.868	+52:13:45.05	6000	560	400/8500	600/4000
05D3hh	14:19:10.168	+52:57:33.42	3600	560	400/8500	600/4000
2005 May 12	**KECK I**		**0.9″**		**LRIS**	
05D3ha	14:20:50.448	+52:50:02.31	3600	560	400/8500	600/4000
05D3hq	14:17:43.058	+52:11:22.67	1800	560	400/8500	600/4000
05D3hs	14:21:13.577	+52:54:13.44	3000	560	400/8500	600/4000
05D3ht	14:17:54.721	+53:10:03.14	4800	560	400/8500	600/4000
05D3jb	14:22:10.024	+52:52:41.28	3600	560	400/8500	600/4000
05D3jh	14:17:25.359	+52:37:07.77	2400	560	400/8500	600/4000
05D3jk	14:16:47.429	+52:35:33.32	2400	560	400/8500	600/4000
05D3jr	14:19:28.768	+52:51:53.34	2400	560	400/8500	600/4000
05D3km	14:22:38.298	+53:04:01.14	2000	560	400/8500	600/4000
2005 Jun 9	**KECK I**		**0.6″**		**LRIS**	
05D3kp	14:20:02.952	+52:16:15.28	3000	560	400/8500	600/4000
05D3kx	14:21:50.020	+53:08:13.49	1800	560	400/8500	600/4000
05D3la	14:21:25.377	+52:21:29.00	5000	560	400/8500	600/4000
05D3lq	14:21:18.449	+52:32:08.29	2000	560	400/8500	600/4000
05D3lr	14:22:12.158	+53:11:03.14	3600	560	400/8500	600/4000
2005 Dec 2	**KECK I**		**1.0″**		**LRIS**	
05D2lz	10:00:59.763	+02:18:30.99	3600	680	400/8500	300/5000
05D2mx	09:59:00.886	+02:27:18.05	5400	680	400/8500	300/5000
2005 Dec 3	**KECK I**		**1.1″**		**LRIS**	
05D2js	10:01:56.959	+01:56:09.93	2400	680	400/8500	300/5000
05D2my	09:58:31.457	+02:29:28.21	4800	680	400/8500	300/5000
2006 Apr 29	**KECK I**		**0.9″**		**LRIS**	
06D2ed	10:01:19.974	+02:39:18.61	2400	560	400/8500	600/4000
06D2ez	10:01:38.653	+01:56:38.85	1000	560	400/8500	600/4000
06D2fb	09:59:32.135	+01:49:40.70	900	560	400/8500	600/4000
06D2fc	09:58:48.262	+02:08:49.63	2700	560	400/8500	600/4000
06D2fe	09:58:36.873	+02:35:36.54	1800	560	400/8500	600/4000
06D2ff	10:00:16.358	+02:14:34.96	1800	560	400/8500	600/4000
06D3df	14:22:17.221	+52:57:27.51	2100	560	400/8500	600/4000
06D3dl	14:22:12.543	+52:38:27.35	1800	560	400/8500	600/4000
06D3do	14:16:59.400	+52:52:57.10	2400	560	400/8500	600/4000
06D3dt	14:17:21.639	+52:27:10.45	1200	560	400/8500	600/4000
2006 May 29	**KECK I**		**0.7″**		**LRIS**	
06D2gb	10:00:47.406	+01:59:07.51	1800	560	400/8500	600/4000
06D3ec	14:20:22.628	+52:21:02.23	3600	560	400/8500	600/4000
06D3ek	14:21:24.960	+52:53:50.39	3000	560	400/8500	600/4000
06D3el	14:17:01.062	+52:13:56.84	1000	560	400/8500	600/4000
06D3em	14:19:23.437	+53:01:22.61	3000	560	400/8500	600/4000
06D3en	14:21:13.304	+52:27:22.09	3600	560	400/8500	600/4000
06D3eq	14:19:02.599	+53:05:17.87	3600	560	400/8500	600/4000

[a]The SNLS naming convention is as follows: *06D3df*: the first two digits are the year of discovery, the second two are the field name, and the final two are *aa* for the first candidate of the year continuing toward *ab* and then on to *ba* for the 27th candidate.

[b]These events were observed on masks by the DEEP2 program and as such were taken on a variety of nights with a variety of seeings.

Table B.3 Summary of SNLS Candidate Observations at Keck: Part III

UT Date	**Telescope**		**Mean Seeing**	**Instrument**		
SN[a]	R.A.	Dec.	Exp (s)	Dichroic	Grating	Grism
2007 Feb 20	**KECK I**		**2.0″**		**LRIS**	
07D3cc	14:20:54.104	+52:28:49.23	6000	560	400/8500	600/4000
2007 Mar 20	**KECK I**		**0.8″**		**LRIS**	
07D2cc	10:01:22.807	+02:21:40.45	3600	560	400/8500	600/4000
07D2cl	10:01:07.419	+02:19:33.34	3600	560	400/8500	600/4000
07D2co	09:58:37.737	+01:51:33.74	3600	560	400/8500	600/4000
07D2dd	10:01:33.815	+01:49:31.24	2700	560	400/8500	600/4000
07D3cp	14:16:35.901	+53:05:02.27	4500	560	400/8500	600/4000
07D3cq	14:16:31.303	+52:47:52.51	3300	560	400/8500	600/4000
07D3cs	14:21:18.225	+52:40:30.52	3000	560	400/8500	600/4000
2007 Apr 17	**KECK I**		**1.2″**		**LRIS**	
07D2dq	10:01:17.574	+02:09:41.23	3600	560	400/8500	600/4000
07D2eb	09:59:26.160	+02:31:08.72	6000	560	400/8500	600/4000
07D2ep	09:59:16.661	+02:32:13.06	6000	560	400/8500	600/4000
07D3bs	14:21:50.466	+53:10:28.58	2700	560	400/8500	600/4000
07D3er	14:22:34.339	+52:11:21.66	3600	560	400/8500	600/4000
07D3fi	14:21:24.800	+53:10:40.10	7800	560	400/8500	600/4000
2007 May 16	**KECK I**		**0.7″**		**LRIS**	
07D2fv	10:01:37.833	+01:48:46.14	5400	560	400/8500	600/4000
07D2gg	09:58:49.154	+02:02:36.25	2400	560	400/8500	600/4000
07D3ar	14:17:49.219	+52:28:11.72	5400	560	400/8500	600/4000
07D3gt	14:19:02.078	+52:39:47.90	5400	560	400/8500	600/4000
07D3gw	14:21:50.902	+53:05:58.66	1800	560	400/8500	600/4000
2007 Oct 13	**KECK II**		**0.6″**		**DEIMOS**	
07D1cl	02:26:50.437	-04:41:47.36	3600	···	600	···
07D1cs	02:25:56.682	-04:22:51.55	3000	···	600	···
07D4en	22:14:47.508	-17:35:28.49	7200	···	600	···
2007 Dec 14	**KECK I**		**1.3″**		**LRIS**	
07D1fl	02:27:33.141	-04:42:49.45	900	560	400/8500	600/4000
07D1hl	02:24:36.566	-04:39:02.64	2300	560	400/8500	600/4000
2008 Jan 8	**KECK I**		**0.8″**		**LRIS**	
08D1af	02:24:13.330	-04:32:40.18	1200	560	400/8500	600/4000
08D1av	02:24:33.194	-04:57:24.04	4100	560	400/8500	600/4000
08D2ac	09:59:31.402	+02:20:25.28	1500	560	400/8500	600/4000
08D2ad	10:00:59.187	+01:45:27.81	2700	560	400/8500	600/4000
08D2ag	09:58:35.122	+01:49:25.06	7200	560	400/8500	600/4000
08D2az	09:59:14.796	+02:37:36.77	1500	560	400/8500	600/4000
2008 Apr 7	**KECK II**		**0.8″**		**DEIMOS**	
08D2hk	10:01:27.543	+02:37:15.23	3000	···	600	···
08D2iw	10:00:26.994	+01:53:57.42	5400	···	600	···
08D2jh	09:59:31.661	+02:14:51.93	3600	···	600	···
08D3ga	14:16:13.266	+52:43:48.39	5400	···	600	···

[a]The SNLS naming convention is as follows: *06D3df*: the first two digits are the year of discovery, the second two are the field name, and the final two are *aa* for the first candidate of the year continuing toward *ab* and then on to *ba* for the 27th candidate.

[b]These events were observed on masks by the DEEP2 program and as such were taken on a variety of nights with a variety of seeings.

Table B.4 Summary of SNLS candidate redshift measurements and classifications: Part I

SN	Type	CI[a]	Template	z	z from	τ_{Spec}[b]	τ_{LC}[c]
03D3ay	SN Ia	4	1989B +14	0.372 ± 0.001	Hβ, [OIII]	+19.0 ± 4.3	24.9
03D3bn	SN Ia*	3	2001ay 0d	0.715 ± 0.001	H	+0.3 ± 3.6	···
03D3bz	SN?	2	···	···	···	···	···
03D3cy	SN?	2	···	0.402 ± 0.001	Hβ, Hα, [NII]	···	···
03D3dd	SN/AGN?	2	···	0.510 ± 0.001	H&K, Na I D	···	···
03D3dr	SN?	2	···	0.737 ± 0.001	[OII], Hβ, [OIII]	···	···
03D3ds	SN?	2	···	0.709 ± 0.001	[OII], H&K	···	···
04D2gb	SN Ia*	3	1992A +7d	0.45 ± 0.01	SN	+6.6 ± 2.5	9.8
04D2ii	SN?	2	···	···	···	···	···
04D3at	SN?	2	···	0.333 ± 0.001	[OIII], Hα, [SI], [SII]	···	···
04D3bt	SN Ib/c	1	1990U +12d	0.111 ± 0.001	Hβ, [OIII]	+10.0 ± 3.7	···
04D3bx	SN?	2	···	0.3888 ± 0.0003	[OIII], Hα	···	···
04D3cf	AGN	0	···	0.531 ± 0.001	Hβ, [OIII]	···	···
04D3cg	AGN	0	···	1.034 ± 0.001	[OII]	···	···
04D3ch	SN	2	···	···	···	···	···
04D3cm	AGN	0	···	1.60 ± 0.01	[MgII]?	···	···
04D3co	SN Ia*	3	1994D +11d	0.62 ± 0.01	SN	+11.0 ± 2.1	16.7
04D3ct	AGN?	1	···	0.605 ± 0.001	[OIII]	···	···
04D3cy	SN Ia	4	1992A +7d	0.643 ± 0.001	Hβ, [OIII]	+6.8 ± 2.7	11.9
04D3db	SN	2	···	0.351 ± 0.001	[OIII]	···	···
04D3df	SN Ia	5	1994D +3d	0.47 ± 0.01	SN	-0.6 ± 4.9	-1.2
04D3do	SN Ia*	3	1998aq +1d	0.61 ± 0.01	SN	+2.4 ± 2.9	5.3
04D3gt	SN Ia	4	1992A +9d	0.451 ± 0.001	H&K	+8.2 ± 5.6	11.5
04D3ht	SN	2	···	0.504 ± 0.001	H&K	···	···
04D3il	SN/AGN?	0	···	···	···	···	···
04D3is	SN	2	···	···	···	···	···
04D3jb	SN?	2	···	···	···	···	···
04D3ki	SN	2	···	···	···	···	···
04D3kk	SN	2	···	···	···	···	···
04D3kr	SN?	2	···	0.337 ± 0.001	[OII], Hβ, [OIII]	···	···
04D3ks	SN Ia	4	1990N -7d	0.75 ± 0.01	SN	-1.6 ± 4.8	-14.1
04D3qa	SN?	2	···	0.370 ± 0.001	Hα, Na I D	···	···
05D2dt	SN Ia*	3	1992A -5d	0.58 ± 0.01	SN	-2.4 ± 4.4	-4.4
05D2du	SN?	2	···	0.227 ± 0.001	Hα	···	···
05D2dw	SN Ia	5	1990N -7d	0.417 ± 0.001	[OII], Hβ, [OIII]	-5.2 ± 2.5	-7.9
05D2hc	SN Ia	5	2001ay +1d	0.35 ± 0.01	SN	-0.8 ± 2.7	0.2
05D2if	SN	2	···	···	···	···	···
05D2js	SN II	0	1999em +9d	0.0926 ± 0.0003	[NII]	+8.4 ± 4.1	···
05D2lz	SN	2	···	0.763 ± 0.001	[OII]	···	···
05D2mx	SN	2	···	0.893 ± 0.001	[OII]	···	···
05D2my	SN Ia	4	1999ee +3d	0.981 ± 0.001	[OII]	+1.8 ± 2.7	6.0
05D3ba	SN	2	···	0.4228 ± 0.0003	[OII], [OIII]	···	···
05D3dd	SN Ia	5	2008ec +11d	0.48 ± 0.01	SN	+11.6 ± 2.8	17.0
05D3dh	SN Ia*	3	1992A +5d	0.80 ± 0.02	SN	+0.8 ± 5.5	4.8
05D3gp	SN Ia	4	2007bd +11d	0.58 ± 0.01	SN	+10.6 ± 2.2	17.2
05D3gv	SN Ia	4	2007bd +8d	0.715 ± 0.001	H&K, [OII]	+6.8 ± 2.3	6.2
05D3gy	SN Ia*	3	1994D +2d	0.84 ± 0.01	SN	-0.2 ± 3.3	···
05D3ha	SN Ia	4	1999ac +11d	0.805 ± 0.001	[OII]	+16.2 ± 5.4	18.6
05D3hh	SN Ia*	3	1989B -7d	0.766 ± 0.001	H&K, [OII]	-1.8 ± 3.1	-6.7
05D3hq	SN Ia	4	1990N +14d	0.3384 ± 0.0003	[OII], H&K, [OIII], Hβ	+10.4 ± 2.1	···
05D3hs	SN Ia	5	2007bd +6d	0.664 ± 0.001	[OII]	+8.4 ± 2.3	13.6
05D3ht	SN Ia	4	1992A +5d	0.901 ± 0.001	[OII]	+6.8 ± 2.2	14.4
05D3jb	SN Ia	4	1990N -7d	0.745 ± 0.001	[OII], H&K	-1.4 ± 5.2	-11.8

[a]SN Ia confidence index outlined in Section B.4: [5] Certain SN Ia, [4] Highly probably SN Ia, [3] Probable SN Ia, [2] Unidentifiable, [1] Probable non-SN Ia, [0] Certain non-SN Ia.

[b]Epoch as determined from spectroscopic fit.

[c]Epoch as determined from light curve; this value only given for data with photometry published in Conley et al. [2011]

Table B.5 Summary of SNLS candidate redshift measurements and classifications: Part II

SN	Type	CI[a]	Template	z	z from	τ_{Spec}[b]	τ_{LC}[c]
05D3jh	SN Ia	4	1992A +5d	0.718 ± 0.001	H&K	+5.6 ± 2.2	10.9
05D3jk	SN Ia	4	1990N -7d	0.736 ± 0.001	[OII]	-1.8 ± 2.7	-4.5
05D3jr	SN Ia	5	1992A +9d	0.37 ± 0.01	SN	+8.6 ± 2.0	9.1
05D3km	SN?	2	···	···	···	···	···
05D3kp	SN Ia	4	1989B -1d	0.85 ± 0.01	SN	+1.2 ± 2.0	1.8
05D3kx	SN Ia	5	2005hc -1d	0.219 ± 0.001	Hα	-1.6 ± 2.0	-2.9
05D3la	SN Ia*	3	1990N -14d	0.90 ± 0.01	SN	-6.2 ± 4.5	-4.4
05D3lq	SN	2	···	0.4204 ± 0.0003	[OII], H&K, [OIII], Hβ	···	···
05D3lr	SN Ia	4	1990N -7d	0.60 ± 0.01	SN	-2.4 ± 4.4	-9.9
06D2ed	SN?	2	···	0.891 ± 0.001	[OII]	···	···
06D2ez	SN Ia	5	1999aa +19d	0.0822 ± 0.0003	Hα	+17.4 ± 2.0	···
06D2fb	SN Ia	5	2008ec +1d	0.1242 ± 0.0003	Hα, [NII]	+0.4 ± 2.0	1.2
06D2fc	SN?	1	···	···	···	···	···
06D2fe	SN II	0	1998S +2d	0.3151 ± 0.0003	[OII], Hβ, [OIII]	+1.5 ± 2.2	···
06D2ff	SN Ia	4	2004ef +9d	0.3447 ± 0.0003	[OII], H&K, Hα	+10.2 ± 2.7	···
06D2gb	SN Ia*	3	1992A +5d	0.442 ± 0.001	H&K	+6.8 ± 3.7	12.8
06D3df	SN Ia	5	2005di +3d	0.4424 ± 0.0003	[OII], H&K	+1.0 ± 3.0	5.2
06D3dl	SN Ia*	3	1999aa +25d	0.3566 ± 0.0003	[OII], H&K, Hβ	+21.2 ± 4.4	···
06D3do	SN Ia	5	1992A +5d	0.7255 ± 0.0003	[OII]	+5.2 ± 2.9	8.6
06D3dt	SN Ia	5	1994D -7d	0.2821 ± 0.0003	[OII], H&K, Hβ, Hα	+0.8 ± 2.5	6.2
06D3ec	SN Ib/c?	0	1984L +14d	0.2842 ± 0.0003	[OII], Hβ, [OIII], Hα	+14.7 ± 2.5	···
06D3ek	SN	1	···	···	···	···	···
06D3el	SN Ia	5	2005hc -1d	0.52 ± 0.01	SN	-3.4 ± 2.6	-8.4
06D3em	SN Ia	4	2005hc +2d	0.69 ± 0.02	SN	+1.4 ± 2.1	4.3
06D3en	SN Ia*	3	1981B 0d	1.06 ± 0.02	SN	-1.6 ± 4.0	4.3
06D3eq	SN not Ia	0	1998S +11d	0.4565 ± 0.0003	[OII], Hβ, [OIII]	+7.0 ± 4.8	···
07D1cl	SN Ia*	3	1989B -5d	0.7048 ± 0.0003	[OII]	-1.6 ± 3.9	···
07D1cs	SN Ib/c	0	1983V +12d	0.4595 ± 0.0003	H&K	+3.4 ± 5.4	···
07D1fl	SN II	0	1987K +7d	0.2056 ± 0.0003	[OII], Hβ, Hα, [NII]	+7.2 ± 4.3	···
07D1hl	SN II?	0	1987B +7d	0.3809 ± 0.0003	[OII], Hβ, [OIII]	+6.6 ± 5.0	···
07D2cc	SN	2	···	0.740 ± 0.001	[OII], H&K, [OIII]	···	···
07D2cl	SN Ia	5	1989B -5d	0.749 ± 0.001	H&K	-0.2 ± 3.2	···
07D2co	SN Ia	4	1981B 0d	0.7375 ± 0.0003	[OII], H&K	-0.4 ± 2.2	···
07D2dd	SN II?	0	···	···	···	···	···
07D2dq	SN?	1	···	0.4408 ± 0.0003	[OII], Hβ, [OIII]	···	···
07D2eb	SN?	2	···	0.7967 ± 0.0003	H&K	···	···
07D2ep	SN Ia	4	2004ef 0d	0.73 ± 0.01	SN	-1.8 ± 3.4	···
07D2fv	SN Ia*	3	1996A +6d	0.871 ± 0.001	H&K	+5.6 ± 1.5	···
07D2gg	SN Ib/c	0	1994I +2d	0.3250 ± 0.0003	[OII], [OIII]	+1.0 ± 4.2	···
07D3ar	AGN	0	···	0.998 ± 0.001	[OII]	···	···
07D3bs	SN	0	···	···	···	···	···
07D3cc	SN Ia	4	2007bd -2d	0.7080 ± 0.0003	[OII], Hβ, [OIII]	-2.6 ± 3.0	···
07D3cp	SN Ia	4	1989B -5d	0.807 ± 0.001	[OII]	-1.0 ± 4.4	···
07D3cq	SN II	0	1984E +4d	0.406 ± 0.001	[OII], Hβ, [OIII]	+3.2 ± 4.8	···
07D3cs	SN Ia	5	1994D +2d	0.8082 ± 0.0003	[OII], Hβ, [OIII]	-1.4 ± 3.8	···
07D3er	SN?	2	···	0.7560 ± 0.0003	[OII], H&K	···	···
07D3fi	SN Ia	4	1994D +2d	0.844 ± 0.001	[OII], H&K	-1.2 ± 2.1	···
07D3gt	SN Ia	5	1992A +5d	0.669 ± 0.001	[OII], H&K	+5.4 ± 3.1	···
07D3gw	SN Ia	4	2005M +4d	0.3913 ± 0.0003	H&K, [OII]	+6.2 ± 2.8	···
07D4en	SN Ia	5	2007kk 0d	0.73 ± 0.01	SN	+1.0 ± 2.8	···
08D1af	SN	2	···	0.143 ± 0.001	H&K, [OII], Hα, [NII]	···	···
08D1av	SN Ia	5	1990N -7d	0.498 ± 0.001	[OII], [OIII]	-7.2 ± 5.2	···
08D2ac	SN Ia	5	1996X -1d	0.4154 ± 0.0003	[OII], [OIII], Hβ	-1.4 ± 2.3	···
08D2ad	SN Ia	4	1992A +5d	0.5537 ± 0.0003	[OII], [OIII], Hβ	+4.8 ± 2.5	···
08D2ag	SN Ia	4	1992A +5d	0.689 ± 0.001	H&K	+6.2 ± 2.0	···
08D2az	SN?	2	···	0.4074 ± 0.0003	H&K	···	···
08D2hk	SN	0	···	0.220 ± 0.001	[OIII], Hα	···	···
08D2iw	SN Ib/c	0	2002ap +5d	0.3255 ± 0.0003	[OIII], Hα	+5.2 ± 2.8	···
08D2jh	SN II	0	1993W +4d	0.2199 ± 0.0003	Hα, Hβ	+6.4 ± 2.6	···
08D3ga	SN Ia*	3	1998aq -8d	0.3685 ± 0.0003	[OIII], Hα, Hβ	-8.2 ± 3.9	···

[a,b,c]As in Table B.4